Retinal Organoid Differentiation, Characterization, and Adaptation as a Model for
Retinitis Pigmentosa

Dissertation
zur Erlangung des Doktorgrades
der Biomedizinischen Wissenschaften
(Dr. rer. physiol.)

der
Fakultät für Medizin
der Universität Regensburg

vorgelegt von
Dr. med. Patricia Berber
aus
Herrenberg

im Jahr

2022

Retinal Organoid Differentiation, Characterization, and Adaptation as a Model for
Retinitis Pigmentosa

Dissertation
zur Erlangung des Doktorgrades
der Biomedizinischen Wissenschaften
(Dr. rer. physiol.)

der
Fakultät für Medizin
der Universität Regensburg

vorgelegt von
Dr. med. Patricia Berber
aus
Herrenberg

im Jahr
2022

Dekan: Prof. Dr. Dirk Hellwig

Betreuer: Prof. Dr. Bernhard Weber

Tag der mündlichen Prüfung: 18.10.2022

A part of this work has been published in a peer-reviewed journal in an open access format:

Contribution: Conceptualization, methodology, study design, data acquisition, analysis, interpretation, and visualization, writing of an initial draft of the manuscript.

Table of Contents

0. Dedication

I dedicate my Ph.D. to the teachers who guided my academic and personal development, especially Mr. John Conlin (AP Calculus, Monta Vista High School).

1. Zusammenfassung

Retinale Organoide (RO) stellen ein 3-dimensionales Zellkulturmodell dar, welches in ihrer zellulären Zusammensetzung und Histoarchitektur dem nativen retinalen Gewebe nahekommt. ROs werden aus humanen induzierten pluripotenten Stammzellen (iPSC) differenziert und ermöglichen somit *in vitro* Untersuchungen an menschlichem Gewebe, zusammengesetzt aus einer Vielzahl von organotypischen Zelltypen. In dieser Studie wurden ROs im Rahmen von zwei Fragestellungen untersucht: Identifizierung der optimalen Bedingungen zur Ausdifferenzierung der ROs und die Eignung der ROs als Modellsystem für eine erbliche Netzhautdystrophie mit hauptsächlicher Beteiligung der Photorezeptoren.

Die erste Fragestellung adressierte vier abgrenzbare Projekte (i-iv). (i) Drei, von unabhängigen Arbeitsgruppen publizierte, Ausdifferenzierungsprotokolle wurden verglichen und das Protokoll mit der höchsten RO Quantität und Qualität wurde identifiziert. (ii) Vorangegangene Arbeiten haben gezeigt, dass mobile Kulturbedingungen die Ausdifferenzierung und Reifung von ROs verbessern. Aus diesem Grund wurden ROs, welche unter konstanter Bewegung kultiviert wurden, mit stationären ROs verglichen. Analysen mittels Immunzytochemie und RNA-Sequenzierung haben gezeigt, dass die Kulturbedingungen keine signifikanten Unterschiede hervorgerufen haben. (iii) Optimierung der Erntemethode, um die Anzahl der erhaltenen RO Fotorezeptoraußensegmente zu erhöhen, wodurch die Anzahl verdoppelt werden konnte. (iv) Charakterisierung der ROs eines Kultivierungszeitraumes zwischen 6 Monaten und 2 Jahren anhand von mRNAexpression, Proteinexpression und Histoarchitektur. Insgesamt zeigte sich, dass eine längere Kultivierungszeit der ROs mit einer niedrigeren Expression der Fotorezeptormarker einherging. Dennoch konnten auch in den 2-jährigen ROs einzelne, morphologisch gut entwickelte Fotorezeptoren nachgewiesen werden. Interessanterweise wurde mit steigender Kultivierungszeit eine höhere Expression von Müllerzellmarkern festgestellt.

Im Rahmen der zweiten Fragestellung wurden zwei unabhängige genetische Ursachen der Retinitis Pigmentosa Typ 1 untersucht. Zuerst wurden ROs mit autosomal dominanten Mutationen im *Retinitis Pigmentosa 1 Axonemal Microtubule Assoziertes* Gen (adRP1), welche im Patienten zu Seheinschränkungen im Erwachsenenalter führen, generiert. Nach 4, 5 und 12 Monaten der Kultivierung war

die Fotorezeptorentwicklung in adRP1 ROs, im Vergleich zu gesunden Kontrollen, nicht beeinträchtigt. Dahingegen zeigten 18 Monate alte ROs eine signifikant niedrigere Expression von 7 Markergenen, die für den bei der adRP1 betroffenen Fotorezeptortyp, die Stäbchen, spezifisch sind. Aus diesen Ergebnissen lässt sich ableiten, dass lange Kulturzeiten die Eignung von ROs als Modellsystem für erbliche Netzhautdystrophien, mit Beginn der Symptomatik im Erwachsenenalter, verbessern. Zudem wurde das CRISPR/Cas9 System verwendet, um selektiv das *RP1* Gen in iPSC stummzuschalten. Ausdifferenzierte ROs werden fortlaufend mit einem vielseitigen Methodenrepertoire untersucht. Zusammenfassend betont dieses Projekt die Vielseitigkeit von ROs als retinales Modellsystem.

2. Summary

Retinal organoids (ROs) are a 3-dimensional cell culture model system, which mimic the cellular composition and histoarchitecture of native retinal tissue. ROs are differentiated from human induced pluripotent stem cells (iPSC), thereby allowing *in vitro* investigations into 3D human tissue, comprised of a range of organotypic cell types. In this study, ROs were investigated in the context of two distinct queries: RO differentiation and development was improved, and their suitability as a model system for inherited retinal diseases with photoreceptor degeneration, was evaluated.

The first query addresses four distinct projects (i-iv). (i) Three previously published RO differentiation protocols were compared, and the method which produced the highest quantity and best quality of ROs was identified. (ii) Previous reports have suggested that nonstationary culture improves RO differentiation, so the influence of an orbital shaker on RO development was evaluated. Immunocytochemistry and RNA sequencing revealed that nonstationary culture did not significantly impact RO development or maturation. (iii) A technique was developed, which improved RO photoreceptor outer segment retention during processing. (iv) A challenge which was resolved in this study, is the lack of insight into RO development past 11 months. The mRNA expression, protein expression, and histoarchitecture of up to 2-year-old ROs was analyzed, which revealed the preservation of retinal histoarchitecture. In general, photoreceptor marker expression decreased over time, but photoreceptors with pristine morphological development were still present in 2-year-old ROs. Interestingly, Mueller cell marker expression increased over time.

In the second part of this study, two genetically distinct causes for retinitis pigmentosa were investigated. First, ROs were differentiated from patient iPSC with autosomal dominant mutations in the *Retinitis Pigmentosa 1 Axonemal Microtubule Associated* gene (adRP1), which causes adult-onset RP with degeneration of rod photoreceptors. Investigations into 4-, 5-, and 12-month-old adRP1 ROs showed normal photoreceptor development. In contrast, rod photoreceptor marker expression was significantly reduced in 1.5-year-old adRP1 ROs, indicating that long-term culture of ROs may be suitable to model adult-onset RP. Finally, CRISPR/Cas9-mediated gene editing was used to produce *RP1* knockout and isogenic control iPSC, which were then differentiated to ROs. The characterization of *RP1* knockout ROs is currently underway. In summary, this project highlights the versatility of ROs as a retinal model.

3.   Introduction

3.1. The Human Retina

In his revolutionary book "On the Origin of Species by Means of Natural Selection", Charles Darwin referred to the eye as an "organ of extreme perfection and complication"(1). Unfortunately, the eye is not always perfect (~8.5 % of people worldwide are disabled by visual impairment or blindness (2,3)), although its complexity cannot be stressed enough. In a healthy eye, light is registered and transduced to an electric signal by the retina (Figure 1A). The retina is part of the central nervous system and contains eight main cell types: ganglion cells, amacrine cells, bipolar cells, horizontal cells, Mueller cells, rod and cone photoreceptor cells, and retinal pigment epithelial cells (RPE; Figure 1B). All cell types, except for the RPE, belong to the neural retina, which has an intricate histoarchitecture. It is structured into five distinct layers, three of which contain the cell bodies: the ganglion cell layer (GCL), inner nuclear layer (INL), and outer nuclear layer (ONL). The GCL and ONL contain one predominant cell type (ganglion cells and photoreceptor cells, respectively), while the INL houses the remaining retinal cells (horizontal, bipolar, amacrine, and Mueller cells). Two layers separate the nuclear layers: the inner and outer plexiform layers (IPL and OPL, respectively). The plexiform layers contain the cellular processes and synaptic contacts of the neural retinal cells. A monolayer of RPE neighbors the photoreceptors in the ONL.
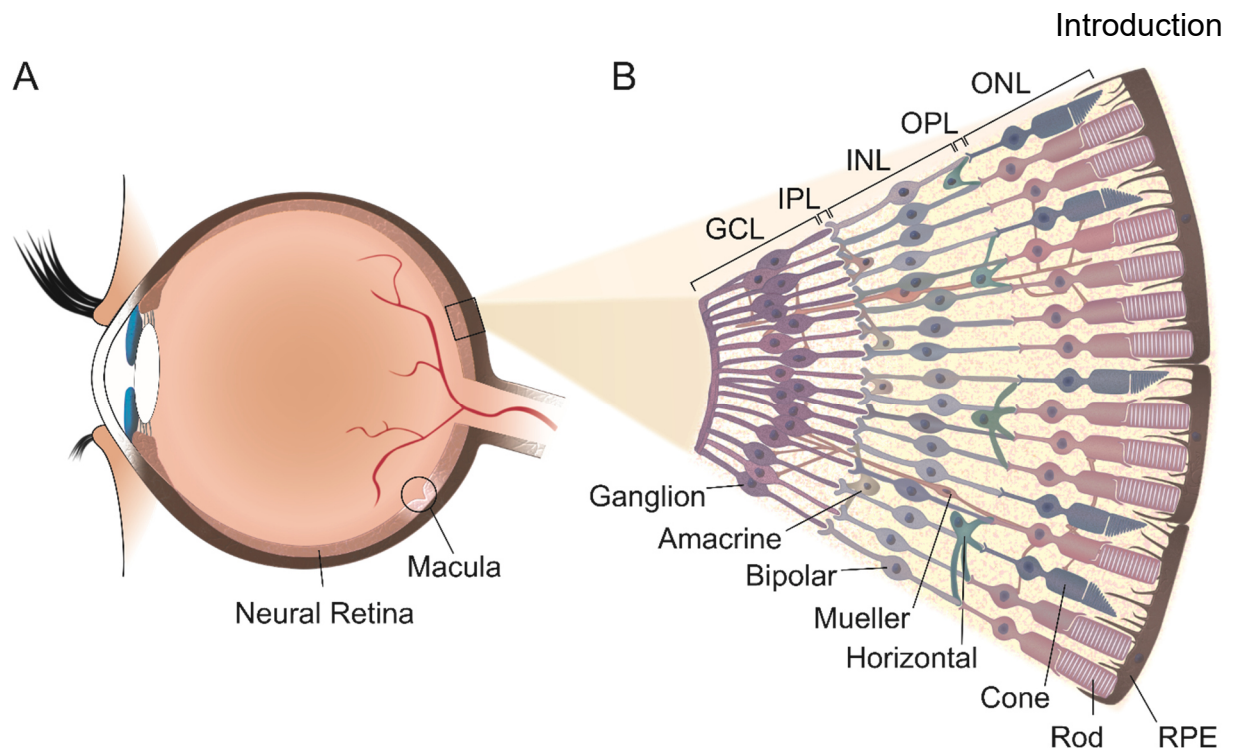
Figure 1: The human retina. A schematic overview of (**A**) the human eye and (**B**) the eight main retinal cell types and the retinal histoarchitecture are shown. The innermost cell layer is the GCL and is comprised of ganglion cells. The adjacent cell layer is the INL and is comprised of horizontal, bipolar, and amacrine cells. The cell bodies of the Mueller cells are also located in the INL, while the Mueller cells stretch the entire length of the neural retina. The outermost layer of the neural retina is the ONL and is comprised of rod and cone photoreceptors. The OPL and IPL separate the nuclear layers. Adjacent to the neural retina, a monolayer of RPE cells envelop and maintain the photoceptor outer segments. This is an original image (section 8.4).

The photoreceptors are highly specialized cells in the retina and are indispensable for initiating vision. Photoreceptors can be divided into a cell body, a permanent inner segment (IS), and a renewable outer segment (OS; Figure 2). The cell body contains the nucleus and the synapses, which join the photoreceptors to the bipolar and horizontal cells. The IS contains a great number of specialized mitochondria, which are necessary to accommodate the photoreceptor's energetic demand (4). The OS contains membranous disks, which is where phototransduction takes place, thanks to a family of proteins called opsins.
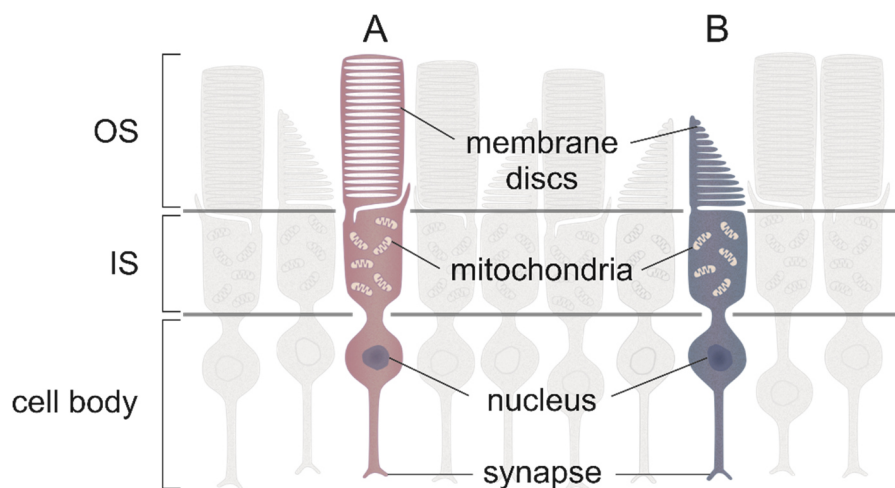
Figure 2: Rod and cone photoreceptors. A schematic overview of a (**A**) rod and (**B**) cone photoreceptor is shown. The planes of the cell body, IS, and OS, are indicated, and are divided horizontally. The OS membrane discs, mitochondria, nucleus, and synapses are indicated. The adjacent photoreceptors of the ONL are shown in light grey. This is an original image (section 8.4).

Humans express several types of opsins, and the photoreceptors are classified according to which opsin they express. The first opsin was discovered at the end of the nineteenth century and named rhodopsin (RHO; (5,6)). RHO is expressed by rod photoreceptors, which are capable of vision at low light levels, but cannot distinguish different colors (Figure 2A; (5)). In the 1950s, three subtypes of cone opsins were discovered: short-, medium-, and long-wavelength-specific opsin (OPN1SW, OPN1MW, and OPN1LW, respectively; (7,8), reviewed in (9)). Cone photoreceptors are imperative for high acuity vision and can perceive color, thanks to their unique absorption maximums for blue, green, or red light (Figure 2B; (8)). The final opsin expressed in the human retina is melanopsin, and was discovered only 22 years ago (10). It is expressed by intrinsically photosensitive ganglion cells (ipGCs), and in contrast to the other mammalian opsins, it is not involved in image formation (10). Instead, ipGCs mediate levels of illumination and are involved in the regulation of the circadian rhythm (reviewed in (11)). The ipGCs have a lower sensitivity and spatiotemporal resolution than photoreceptors (reviewed in (12)).

The photoreceptors are supported by the overlying monolayer of pigmented and polarized RPE cells, which shuttle energy sources and waste products for the photoreceptors (reviewed in (13)). The RPE also have finger-like processes, which reach in-between the photoreceptor OS. Via these protrusions, the RPE phagocytize shed photoreceptor OS. Perhaps most importantly, the RPE contain the biochemical

machinery required to recycle the photopigments needed for phototransduction (14,15).

3.2. Retinogenesis

As is to be expected for such a complex organ, the embryological eye development consists of a series of intricately orchestrated biological and physical events. Eye development begins shortly after gastrulation, when the neural tube develops five secondary vesicles including the diencephalon (reviewed in (16)). Beginning on day 22 of embryological development, the neuroepithelium of the diencephalon evaginates to form a protrusion known as the optic vesicle (Figure 3A). This process is coordinated by the expression of several eye field transcription factors such as Pax6, Rax, and Lhx2 (reviewed in (17)). The optic vesicle grows and extends towards the surface ectoderm, all the while remaining attached to the diencephalon base via the optic stalk. After reaching the surface ectoderm, the growth direction of the optic vesicle reverses, and the optic vesicle forms a central indentation which continues growing towards the diencephalon (Figure 3B). This step in the embryological eye development is called invagination. The region of the surface ectoderm juxtaposed to the neuroepithelium differentiates to the lens placode. In an experiment of historical significance (18), Hans Spemann, who is regarded as the founder of developmental biology (19), showed that the ablation of the optic vesicle prior to invagination can prevent lens formation (20). He thereby showed that lens formation is dependent on contact between the optic vesicle and surface ectoderm (20). This was the first demonstration of the process known as embryonic induction, and Spemann was rewarded for his contribution to science with the Nobel Prize in Physiology or Medicine in 1935 (21).
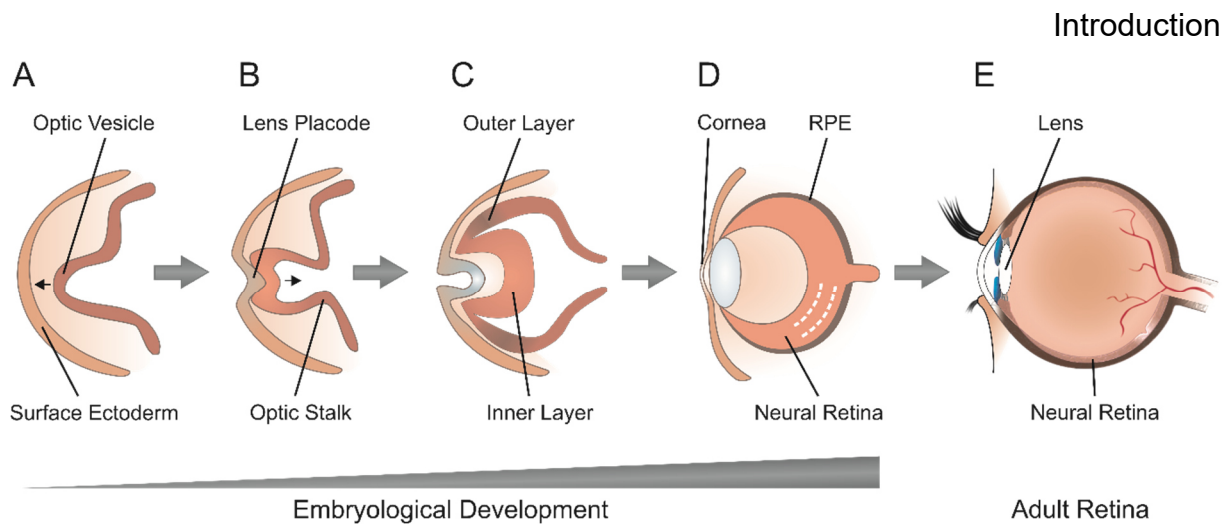
Figure 3: Retinogenesis. (**A-D**) A schematic overview of the embryological eye development and (**E**) an adult eye is shown. (**A**) The eye development begins when the diencephalon neuroepithelium evaginates towards the surface ectoderm, forming the optic vesicle. The growth direction of the neuroepithelium is indicated by a small, black arrow. (**B**) The neuroepithelium changes growth direction and invaginates along with a small portion of the surface ectoderm, known as the lens placode. The growth direction of the neuroepithelium is indicated by a small, black arrow. (**C**) The invagination of the optic vesicle forms a bilayered optic cup. The outer and inner layer are indicated. (**D**) The inner layer of the optic cup forms the neural retina (the division of the three nuclear layers is indicated by dashed, white lines). The outer layer of the optic cup forms the RPE. The lens and cornea differentiate from the lens placode and surface ectoderm, respectively. (**E**) A cross-section of an adult eye is shown in the sagittal plane. The location of the neural retina and lens are indicated. This is an original image (section 8.4).

The invagination of the optic vesicle occurs by embryonic day 32, and is crucial for the formation of a bilayered optic cup (Figure 3C). The structure of the bilayered optic cup can be used as a reference point to track the development and histoarchitecture of the adult retina. The cells of the outer layer develop to the RPE, whereas the inner layer serves as the basis for all types of retinal neurons (Figure 3D, E). The development of retinal neurons is dependent on the expression of bone morphogenic protein 4 (BMP4), as the conditional deletion of BMP4 from the optic vesicle resulted in an optic cup devoid of neural retinal markers (22). In contrast, germline deletion of BMP4 is embryologically lethal between day 6.5 and 9.5 post conception, underscoring the importance of this signaling marker (23).

In humans, retinal development extends past birth. Newborns have immature rod and cone photoreceptors, with short OS (24). At birth, retinal ganglion cells do not respond to rod and cone photoreceptor stimulation (25), indicating that the synaptic connections which transmit visual cues in the adult retina (electric stimuli are generally passed from a photoreceptor to a bipolar cell to a ganglion cell) are established postnatally (reviewed in (11)). Still, as anyone who has woken a sleeping baby with

flash photography can attest, neonate retinas can detect illumination from birth. They perceive visual cues via the melanopsin-expressing ipGCs (26), which transmit their signals directly to the region of the brain responsible for circadian rhythm, the suprachiasmatic nucleus (27,28). It is unclear whether the visual cues are interpreted simply as light/dark stimuli or as images, since some ipGCs also transmit information to the visual cortex (28). Many ipGCs succumb to an early wave of apoptosis, and only a fraction of ganglion cells in adult retinae are light sensitive (29). As the ipGCs degenerate, the photoreceptors mature morphologically and functionally, and become the predominant receptors and transmitters of visual stimuli in the adult retina.

3.3. Retinal Organoids[1]

The complexity of the human retina has hampered the study of human retinal development in health and disease. Rodent models have allowed some insight into their human counterparts, but there are important anatomical and functional differences between rodent and human retinae, such as the absence of a cone-photoreceptor exclusive macula (30,31). Recently, scientists have developed a human *in vitro* retinal model system, known as retinal organoids (ROs).

Organoids are three-dimensional (3D) *in vitro* miniature organs, which contain multiple organ-specific cell types and a comparable spatial organization to the native tissue (32). To date, differentiation protocols for many different miniature organs exist, including cerebral organoids (33–36), intestinal organoids (37,38), lung organoids (39,40), and kidney organoids (41), among others. Organoid research was pioneered in 2005 when the Sasai group developed a protocol to selectively differentiate murine embryonic stem cells to neurons (33,42). In the following years, the same group developed methods to differentiate murine and later human embryonic stem cells to optic cups ((43,44), reviewed in (19)). These advances served as a cornerstone for other groups to develop human induced pluripotent stem cell (iPSC) derived RO differentiation protocols (45–48). In contrast to embryonic stem cells, iPSCs are reprogrammed from mature primary cells such as fibroblasts, peripheral blood mononuclear cells (PBMCs), or epithelial cells (Figure 4A, B). The discovery that

---

[1]Parts of this section were adapted from Berber et al. (161).

mature cells can be reprogrammed to immature stem cells, earned Sir John B. Gurdon and Shinya Yamanaka the Nobel Prize in Physiology of Medicine in 2012 (49–51).
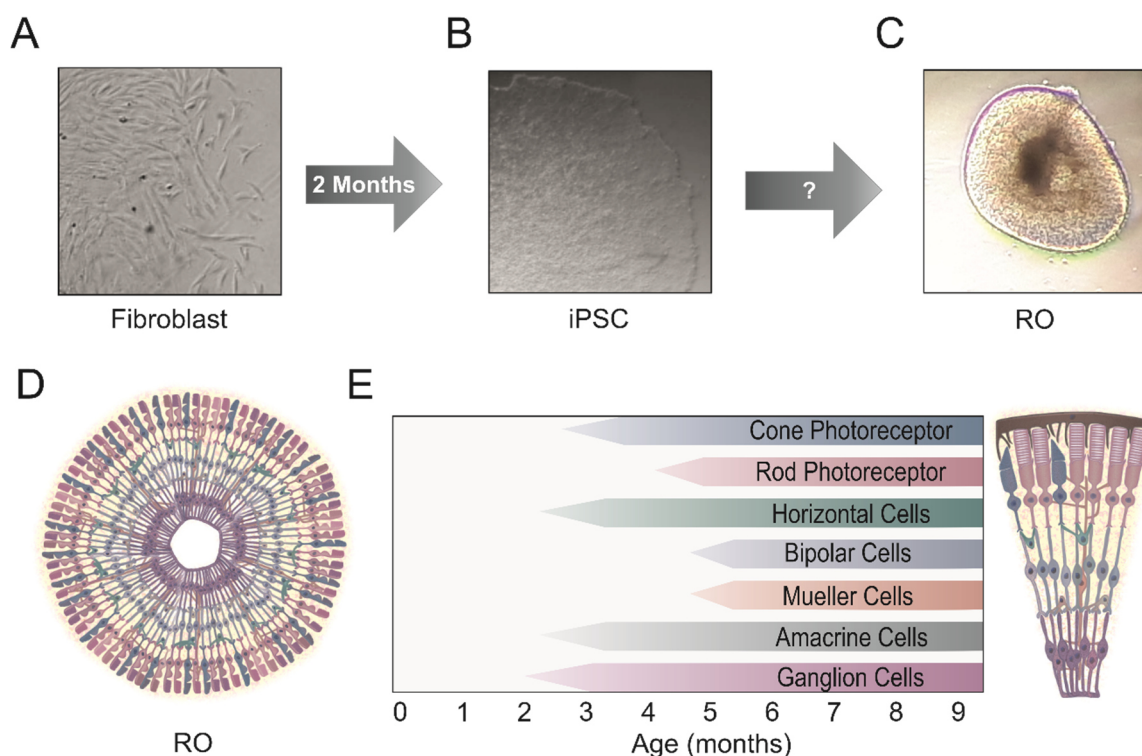

Figure 4: RO differentiation. Brightfield images of (**A**) fibroblasts, (**B**) iPSCs, and (**C**) a RO are shown. RO differentiation begins with the reprogramming of adult cells such as fibroblasts to iPSC. The derivation of fibroblasts from a dermal biopsy takes around 1 month, and the reprogramming to iPSC takes around 1-1.5 months, depending on the growth rate of the cells (2 - 2.5 months total). The time period needed to differentiate iPSC to a RO is dependent on their desired application, since the cellular development of a RO generally follows the retinal birth sequence. (**D**) A schematic depiction of an ideal RO (containing the neural retinal cell types and a pristine histoarchitecture) is shown. (**E**) The neural retina birth sequence is shown. Ganglion cells are the first cell type to differentiate, quickly followed by amacrine cells and later horizontal cells. Cone photoreceptors develop, followed by rod photoreceptors. Bipolar cells and Mueller cells are the last cell types to differentiate. A schematic overview of a retina is shown on the right, which is color-coordinated to the cell types in the retinal birth sequence. The brightfield image of iPSCs shown in (B) was kindly provided by PD Dr. Caroline Brandl and is replicated with permission (section 8.3). All other images in this figure are original (section 8.4).

ROs contain the main cell types native to the retina, and have a similar histoarchitecture to native tissue (Figure 4C, D). To date, a variety of RO differentiation protocols have been established. Broadly, the procedures can be classified into two main categories: 3D protocols and 3D-2D-3D protocols (reviewed in (52)). The 3D differentiation protocols are based on the serum-free embryoid body-like quick aggregation culture technique developed by Eiraku et al. (33,42) and Watanabe et al. (53). In this technique, the cells are cultured in suspension for the entire differentiation process (referred to as "3D" culture). Later, other groups added a temporary adherent

phase (the "2D" phase) after the aggregation step, which improved the retinal domain development (54). Retinal domains are organoid precursors, which are excised and cultured in suspension until they are harvested (the second "3D" phase; (54)). Protocols from both categories can be modified by including a variety of extrinsic chemical signals to promote retinal differentiation or enhance cell survival (reviewed in (17)).

On a cellular level, the differentiation of iPSC to ROs follows a similar timeline to *in vivo* retinogenesis. *In vivo*, neural retinal cells differentiate in a characteristic order, known as the retinal birth sequence (Figure 4E, reviewed in (16,55)). Ganglion cells develop first (starting at human fetal week ~8), closely followed by the amacrine cells and horizontal cells. Together with the cone photoreceptors, these cells can be grouped together as early-born cell types. Late-born cell types include the rod photoreceptors, bipolar cells, and Mueller cells (starting at human fetal week ~18). Of note, the retinal birth order only indicates the acquisition of cell fate, but does not reflect their maturation process. For example, photoreceptors acquire their cell fate after 3-4 months, develop IS after 5 months, and OS after 6 months (56–58).

RO differentiation follows the retinal birth sequence with two important exceptions: first, the emergence of cone photoreceptors is delayed, and occurs after RHO-positive rod photoreceptors have already developed (59). There is a second, more consequential difference between *in vitro* RO differentiation and *in vivo* retinogenesis. The invagination of the optic vesicle which results in a bilayered optic cup has not been reproducibly demonstrated *in vivo* (44). Although ROs can contain clumps of ectopic RPE cells, the monolayer of RPE cells which protect and supply the photoreceptors *in vivo* is missing from RO cultures (59,60). Nevertheless, the molecular profile of the RO cells appear to be fairly similar to their native counterparts (61,62).

3.4. Retinitis Pigmentosa

One exciting research application for ROs, is the investigation of inherited retinal dystrophies such as retinitis pigmentosa (RP, OMIM #268000, Figure 5A). RP affects ~ 1:4,000 people worldwide ((63), reviewed in (64)), and is characterized by the progressive loss of rod photoreceptors, followed by secondary cone photoreceptor degeneration (Figure 5B). RP patients experience a triphasic symptomatic course,

which begins with night blindness, progresses to tunnel vision (Figure 5C), and eventually renders the patients partially or completely blind (reviewed in (65,66)).
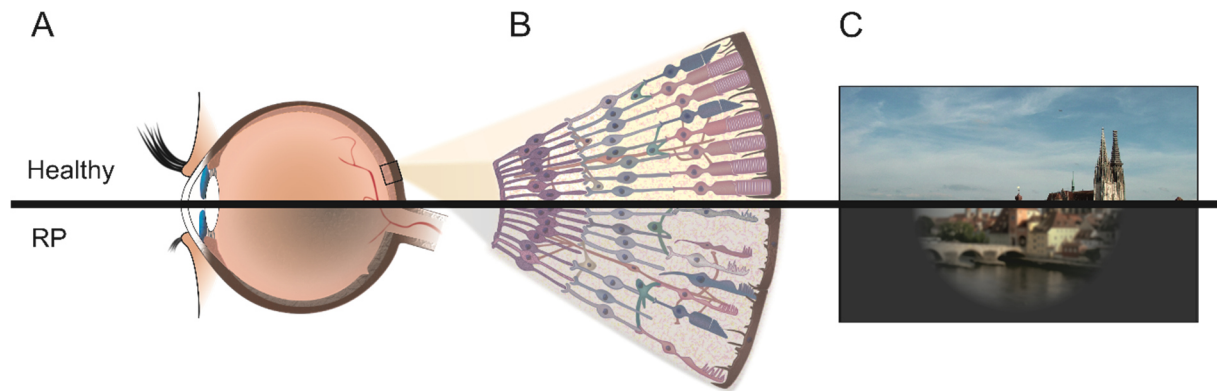

Figure 5: RP. (**A**) A schematic cross-section of a healthy eye, and an eye with RP are shown in the sagittal plane. The RP affected eye shows the attenuation of the retinal vasculature and the formation of bone spicules (shown as dark grey discoloring). (**B**) A schematic visualization of a healthy and RP retina is shown. The RP retina shows the deterioration of the rod photoreceptors. Other cell types such as the cone photoreceptors and RPE also show signs of stress. (**C**) A schematic demonstration of the visual field in a healthy and RP individual are shown. Persons with RP experience a narrowing of the visual field known as tunnel vision. The image shown in (C) was kindly provided by Prof. Dr. Klaus Stark and is replicated with permission (section 8.3). All other images in this figure are original (section 8.4).

Non-syndromal RP has been linked to mutations in over 85 causative genes/loci (67,68), and follows an autosomal recessive (arRP, 15-25 % of cases), autosomal dominant (adRP 5-20 % of cases), or X-linked (xlRP, 5-15 % of cases) mode of inheritance (69–71). Extremely rare cases of mitochondrial inheritance have also been reported (mtRP, (72)). In general, disease progression appears to be mildest in adRP and fastest in xlRP (70,73). Despite the use of multigene panels, next generation sequencing (NGS), and exome sequencing, ~ 40 % of cases remain unresolved (71).

There is evidence underscoring the application of ROs as a model system for RP. A publication from 2018 examined iPSC-derived ROs from three RP patients with mutations in the *Retinitis Pigmentosa GTPase Regulator* gene (*RPGR*, associated with xlRP) (74). The authors observed defects in RO photoreceptor morphology and localization, as well as lower opsin expression after 5.5 months (74). ROs have also been used to model other inherited retinal dystrophies such as Leber congenital amarousis (LCA). A recent publication from 2021 showed defective photoreceptor maturation by immunocytochemistry and gene profiling in 5.5-month-old LCA-ROs with an autosomal dominant mutation in the *Cone-Rod Homeobox* gene (*CRX*; (75)). Of note, another group examined LCA-ROs with an autosomal recessive mutation in the *Aryl hydrocarbon receptor-interacting protein-like 1* gene (*AIPL1*), and observed that

the ROs maintained their cellular cryoarchitecture after 6.75 months (76). So far, ROs have not been used to perform in-depth investigations into the phenotypic repercussions of RP-causing mutations in the *Retinitis Pigmentosa 1 Axonemal Microtubule Associated* gene (*RP1*) (77).

3.5. RP1

Between 4 – 10 % of adRP cases and <1 % of arRP cases are caused by pathogenic variants in *RP1* (OMIM # 180100; (78–81)). *RP1* contains four exons, although the open-reading frame does not include exon 1 (81). The location of pathogenic variants within the gene dictate their inheritance pattern (Figure 6A; (82)). Dominant pathogenic variants are clustered in a mutational hotpot region in exon 4 (adRP1; amino acid 500 – 1053; (82)). They are usually frameshift or nonsense mutations which result in the expression of a truncated RP1 protein, since mutations in final exons are insensitive to nonsense-mediated decay (83). Biallelic missense, nonsense, or frameshift variants that are located in exon 2 and 3, or flank the hotspot region in exon 4, cause recessive disease (arRP1; (82)). A genotype-phenotype relationship can be observed regarding adRP1 and arRP1: the mean age of onset is the 2nd-6th decade of life in adRP1, and the 1st-2nd decade in arRP1 (82,84,85). Furthermore, adRP1 causes a milder phenotype (refractive error interquartile range −2.50; +0.88 diopters) than arRP1 (range −9.0; 1.88 diopters) (85).
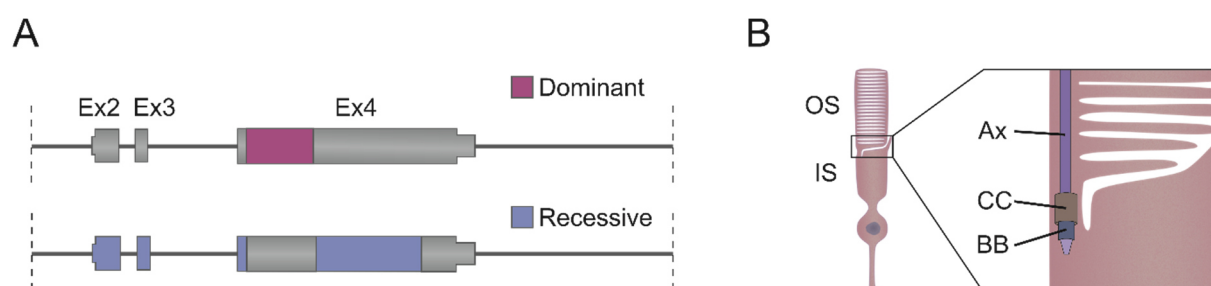

Figure 6: *RP1*. (A) A schematic representation of all coding exons of *RP1* are shown. The mutation hotspot region for autosomal dominant mutations is shown in magenta (amino acid 500-1053), and the regions for autosomal recessive mutations are shown in lavender. (**B**) A schematic overview of a rod photoreceptor, with an enlarged depiction of the transition zone between the IS and OS is shown. The transition zone contains (from the IS to OS) the basal body (BB), connecting cilium (CC), and axoneme (Ax). RP1 is expressed at the photoreceptor axoneme (Ax). This is an original image (section 8.4).

RP1 is expressed in rod and cone photoreceptors, and encodes a 240 kDa microtubule binding protein which is localized at the photoreceptor axoneme (Figure 6B; (86,87)). RP1 is involved in the transport of proteins such as RHO from the inner

to the OS, and the organization of the OS membrane discs (86,88). The phenotypic repercussions of several *RP1* mutations have been evaluated in mice. *RP1* knockout mice (*RP1$^{-/-}$*), exhibited RHO mislocalization to the IS and cell bodies, rod photoreceptor degeneration, and shortened and deformed rod and cone OS (89). In contrast, characterizing adRP1 pathogenesis in mice has proven more difficult. Investigations of up to 30 month old mice with heterozygous Q662X mutations (a nonsense mutation known to cause adRP1 in humans), failed to reveal any significant structural or functional retinal abnormalities (90). Mice with homozygous Q662X mutations, showed progressive photoreceptor degeneration, which was again characterized by the disorganization of photoreceptor OS discs (90). Similar results were obtained with mice harboring *myc*-tagged truncating mutations in exon 4: *RP1$^{myc/myc}$* mice underwent retinal degeneration characterized by incorrectly oriented OS discs, whereas *RP1$^{+/myc}$* mice only had mildly reduced rod a-waves, analyzed via electroretinogram, after 8 months (88). The incongruencies between murine adRP1 and human disease, suggest that a human model system, such as ROs, may be more suited to model adRP1.

3.6. Aim of this Study

ROs are iPSC-derived 3D human retinal model systems, that contain all main retinal cell types and have a comparable histoarchitecture to native tissue. Broadly, this thesis was grouped into two main queries: the characterization and improvement of RO differentiation (Figure 7A-D), and the application of ROs as a model system for an inherited retinal disease (Figure 7E, F). The first part of the thesis includes four distinct projects (i-iv). (i) Three previously published RO differentiation techniques were performed, and the RO quantity and quality from each technique were compared (Figure 7A). (ii) Previous studies have suggested improved photoreceptor differentiation through nonstationary culture (91,92), so the influence of an orbital shaker on RO development was determined (Figure 7B). (iii) Different techniques were implemented with the aim of improving the retention of RO photoreceptor OS (Figure 7C). (iv) The final investigation aimed to characterize ROs, was to examine up to 2-year-old ROs via immunocytochemistry and RNA sequencing to characterize the effect of long-term culture on ROs (Figure 7D).

The second part of the thesis, aimed to apply ROs as a model system for RP and encompassed two distinct projects. ROs were differentiated from two adRP1 patients and analyzed after up to 1.5 years in culture via immunocytochemistry and RNA sequencing (Figure 7E). Furthermore, the phenotypic repercussions of *RP1* knockout mutations in ROs were examined. Therefore, iPSCs were edited with the CRISPR/Cas9 system to induce frameshift mutations in *RP1*, differentiated to ROs, and are being investigated via immunocytochemistry and brightfield imaging (Figure 7F).
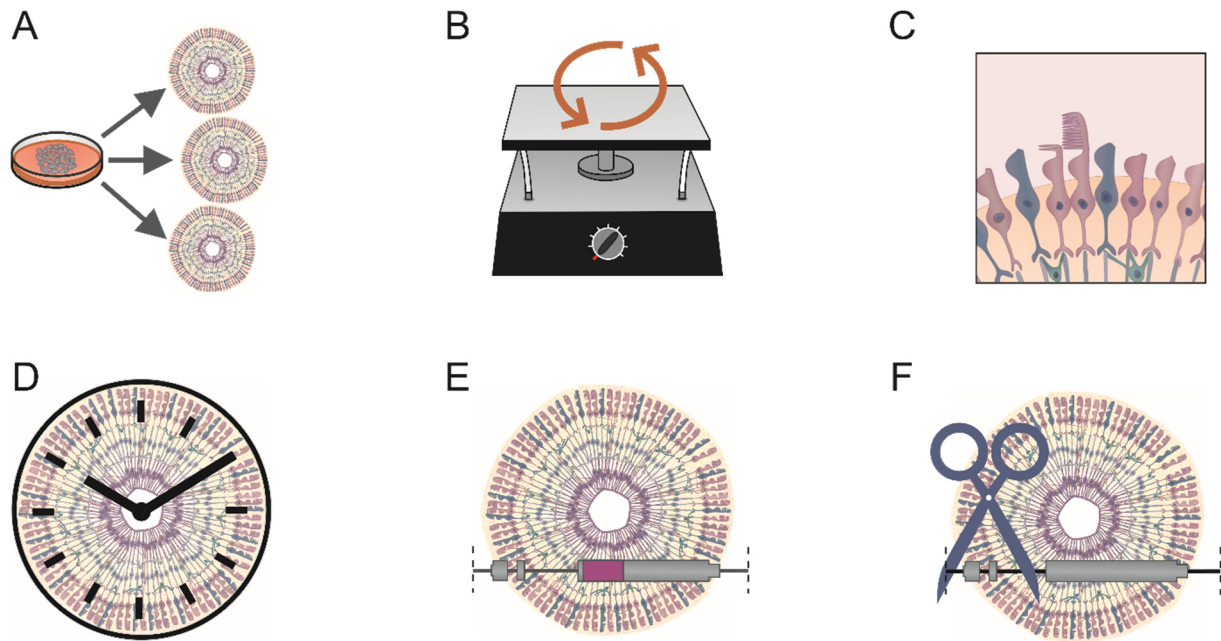
Figure 7: Aims of this study. (**A**) iPSCs were differentiated to ROs following three previously published protocols, and the RO quantity and quality were compared. (**B**) ROs cultured on an orbital shaker were investigated. (**C**) A technique to retain more of the RO photoreceptor OS was established. (**D**) ROs were cultured for up to 2 years to evaluate *in vitro* maturation. The ROs were analyzed via immunocytochemistry (ICC) and RNA sequencing. (**E**) ROs differentiated from individuals harboring autosomal dominant mutations in *RP1* were investigated. (**F**) iPSCs were treated with CRISPR/Cas9 to induce frameshift mutations in *RP1*, differentiated to ROs and examined via brightfield microscopy and ICC. This is an original image (section 8.4).

4. Material

4.1. Eukaryotic Cell Lines

Table 1: iPSC lines used in this study

iPSC line	Pseudonym	Clones	Primary Tissue	*RP1* Genotype
MK270413	HD #1	26, 27	Fibroblast	wt
NG050912	HD #2	2, 3	Fibroblast	wt
NJ250216	HD #3	105, 111	PBMC	wt
AM220316	HD #4	260	Fibroblast	wt
CW200918	adRP1 #1	266, 264	Fibroblast	+/c.2117delG
JG200918	adRP1 #2	286, 287	Fibroblast	+/c.2321_2322insAluYa5
HG200918	adRP1 #3	288, 289	Fibroblast	+/c.2321_2322insAluYa5

Reprogramming of iPSC and subsequent differentiation was approved by the local ethics committee (reference no. 11-101-0228). All primary tissues samples were acquired (either via dermal punch biopsy or blood draw) at the University Hospital Regensburg. HD: Healthy Donor; adRP1: autosomal dominant Retinitis Pigmentosa 1; PBMC: Peripheral Blood Mononuclear Cell; wt: wildtype

Table 2: CRISPR/Cas9 treated iPSC lines generated in this study

iPSC line	Pseudonym	*RP1* Genotype
MK161019B Clone 3	RP1_KO #1	c.295insC/c.295insC
MK161019B Clone 4	RP1_WT #1	wt
MK161019B Clone 107	RP1_KO #2	c.295delC/c.295delC
MK161019B Clone 109	RP1_WT #2	wt

KO: Knockout; WT: wildtype

Table 3: Additional eukaryotic cell line used in this study

Cell line	Organism	Tissue of Origin	Source
HEK293	*Homo Sapiens*	Embryonic kidney	ATCC, LGC Standards GmbH, Wesel, Germany

4.2. Bacterial Cell Lines

Table 4: Bacterial strains used in this study

Strain	Source
E. coli strain DH5α	Life Technologies, Carlsbad, USA
One Shot™ Stbl3™	Life Technologies, Carlsbad, USA

4.3. Vector

Table 5: Vectors used in this study

Vector	Application	Source
pGEM®-T	Cloning	Promega Corporation, Madison, USA
pCAG-EGxxFP	gRNA Efficiency Assay	Addgene, LGC Standards, Teddington, UK
pU6-(BbsI)_CBh-Cas9-T2A-mCherry	gRNA Efficiency Assay	Addgene, LGC Standards, Teddington, UK

4.4. Oligonucleotides

All oligonucleotide primers were purchased from Metabion, Planegg, Germany.

Table 6: Oligonucleotide primers used for the gRNA efficiency assay

Name	Sequence (5' to 3')
gRNA_RP1_KO_4_20mer_F	CACCGacttgaccttcagaagacgt
gRNA_RP1_KO_4_20mer_R	AAACacgtcttctgaaggtcaagtC
gRNA_RP1_KO_5_20mer_F	CACCGatttctacagcacctgacag
gRNA_RP1_KO_5_20mer_R	AAACctgtcaggtgctgtagaaatC
gRNA_RP1_KO_6_20mer_F	CACCGtagacctggacaaagcccgt
gRNA_RP1_KO_6_20mer_R	AAACacgggctttgtccaggtctaC
gRNA_RP1_KO_7_20mer_F	CACCGgcacagcatcacgcgcctgg
gRNA_RP1_KO_7_20mer_R	AAACccaggcgcgtgatgctgtgcC
gRNA_RP1_KO_8_20mer_F	CACCGaggaacatcagcacccctcg
gRNA_RP1_KO_8_20mer_R	AAACcgaggggtgctgatgttcctC
gRNA_RP1_KO_9_20mer_R	CACCGgagtcctacctatgttccca
gRNA_RP1_KO_10_20mer_F	AAACtgggaacataggtaggactcC
gRNA_RP1_KO_9_20mer_F	CACCGgtgaggctcaaatggcgagg
gRNA_RP1_KO_10_20mer_R	AAACcctcgccatttgagcctcacC

Uppercase letters denote the restriction enzyme cutting sites needed for cloning

Table 7: Oligonucleotide primers used to generate sgRNA for iPSC CRISPR/Cas9 treatment

Name	Sequence (5' to 3')
SZ_RP1_KO_5F	TAATACGACTCACTATAGatttctacagcacctgacag
SZ_RP1_KO_5R	TTCTAGCTCTAAAACctgtcaggtgctgtagaaat
SZ_RP1_KO_7F	TAATACGACTCACTATAGgcacagcatcacgcgcctgg
SZ_RP1_KO_7R	TTCTAGCTCTAAAACccaggcgcgtgatgctgtgc
SZ_RP1_KO_8F	TAATACGACTCACTATAGaggaacatcagcacccctcg
SZ_RP1_KO_8R	TTCTAGCTCTAAAACcgaggggtgctgatgttcct
SZ_RP1_KO_10F	TAATACGACTCACTATAGgtgaggctcaaatggcgagg

SZ_RP1_KO_10R	TTCTAGCTCTAAAACcctcgccatttgagcctcac

Uppercase letters denote the T7 promotor

Table 8: Oligonucleotide primers used for polymerase chain reaction (PCR) and Sanger sequencing

Name	Sequence (5' to 3')
M13F	cgccagggtttttcccagtcacgac
M13R	agcggataacaatttcacacagga
RP1 ex2.2 F	aggaacatcagcacccctc
RP1 ex3 F	ttcaagcctaggaggttgttg
RP1 ex3 R	attgaagcatggatttttgcc
RP1 ex4.1 F	gatatttctaacttctctgccttcc
RP1 ex4.1 R	aaactgccctcttgattactgc
RP1 ex4.2 F	tcatctggtttaaagcttgcag
RP1 ex4.2 R	ttgacttaagcagactgttttcc
RP1 ex4.3 F	gggaaagtggggaaaacaag
RP1 ex4.3 R	aatttattgcttgctgtcgag
RP1 ex4.4 F	cctctactgtcactgcaagaattg
RP1 ex4.4 R	cactttatctctttgaccgatttc
RP1_2.3_F	ccctcgctcctttaagtcct
RP1_Ex2.1_EcoR1_F	GAATTCtgcattagtattaccatgtattcgc
RP1_Ex2.2_BamHI_R	GGATCCccacacgaatccaattagtag

Uppercase letters denote the restriction enzyme cutting sites; F: forward, R: reverse

Table 9: Oligonucleotide primers and probes used for qRT-PCR

Target	Name	Sequence (5' to 3')
BEST1	BEST1-H2-F	ACATGGATCCTTATTGGGCC
	BEST1-H2-P	ACCTGCTTCCTAATGGGGATGCTTCGC
	BEST1-H2-R	CTGTGACTGGATCAGTGTCC
HPRT1	HPRT1-H1-F	CTTTGCTTTCCTTGGTCAGG
	HPRT1-H1-P	GCTTGCTGGTGAAAAGGACCCCACG
	HPRT1-H1-R	TCAAATCCAACAAAGTCTGGC
MITF	MITF-H3-F	TATGGAAACCAAGGTCTGCC
	MITF-H3-P	CCACCAGGCCTCACCATCAGCAACT
	MITF-H3-R	CTTCAGACTCTGTGAGCTCC
PMEL	PMEL-H3-F	CTGGTGAAGAGACAAGTCCC
	PMEL-H3-P	AAGTGCCGAGATCCTGCAGGCTGT
	PMEL-H3-R	CAGTCAGCTCAAATGCATCC
RHO	RHO-H3-F	CCTACATGTTTCTGCTGA
	RHO-H3-P	CATCAACTTCCCACGCTCTACG
	RHO-H3-R	CAGGATGTAGTTGAGAGG
RP1	RP1-H1-F	AGGCAGCCATTTAAACCAGG
	RP1-H1-P	TCTCTCAGCGTGTGTACCCCAAGGGA

	RP1-H1-R	AGCTTGAAGACATATGTGTGC
	RPE65-H2-F	AGAATTTAGTCACGCTCCCC
RPE65	RPE65-H2-P	GCAGTGACGAGACTATCTGGCTGGAGC
	RPE65-H2-R	AACTCAAATGCTTGACGAGG

F: forward, R: reverse, P: probe

4.5. Molecular Weight Standard

Table 10: Molecular weight standard used in this study

Standard	Source
GeneRuler™ DNA Ladder Mix	Life Technologies, Carlsbad, CA, USA

4.6. Enzymes

Table 11: Enzymes used in this study

Enzyme	Source
Antarctic Alkalic Phosphatase	New England Biolabs, Ipswich, MA, USA
Dispase in DMEM/F12	STEMMCELL Technologies Inc., Vancouver, BC, Canada
Exonuklease I	Life Technologies, Carlsbad, CA, USA
GoTaq® DNA Polymerase	Promega Corporation, Madison, WI, USA
Pronase E (from Streptomyces griseus)	Merck KGaA, Darmstadt, Germany
ReLeSR™	STEMMCELL Technologies Inc., Vancouver, BC, Canada
RevertAid™ Reverse Transcriptase	Thermo Fisher Scientific, Waltham, MA, USA
RNase-free DNase I	QIAGEN GmbH, Hilden, Germany
StemPro™ Accutase™	Life Technologies, Carlsbad, CA, USA
T4-DNA Ligase	New England Biolabs, Ipswich, MA, USA
TrueCut™ Cas9 Protein	Life Technologies, Carlsbad, CA, USA
TrypLE™ Select (1x)	Life Technologies, Carlsbad, CA, USA

4.7. Kits

Table 12: Kits used in this study

Kit	Source
BigDye Terminator v3.1 Cycle Sequencing Kit	Life Technologies, Carlsbad, CA, USA
GoTaq® Long Expand PCR Master Mix	Promega Corporation, Madison, WI, USA
Human Dermal Fibroblast Nucleofector™ Kit VPD-1001	Lonza Bioscience, Basel, Switzerland
Human Stem Cell Nucleofector™ Kit 2	Lonza Bioscience, Basel, Switzerland

NEXTFLEX® Poly(A) Beads	PerkinElmer, Waltham, MA, USA
NEXTFLEX® Rapid Directional RNA-Seq Library Prep Kit	PerkinElmer, Waltham, MA, USA
NEXTFLEX® RNA-Seq Barcodes 1 - 48	PerkinElmer, Waltham, MA, USA
NucleoSpin Tissue Genomic DNA Purification Kit	Machery-Nagel GmbH & Co. KG, Dueren, Germany
NucleoSpin® Gel and PCR Clean-up	Machery-Nagel GmbH & Co. KG, Dueren, Germany
NucleoSpin® Plasmid Mini Kit	Machery-Nagel GmbH & Co. KG, Dueren, Germany
pGEM®-T Vector	Promega Corporation, Madison, WI, USA
Precision gRNA Synthesis Kit	Life Technologies, Carlsbad, CA, USA
PureLink™ RNA Micro Kit	Invitrogen, Carlsbad, CA, USA
PureLink™ RNA Mini Kit	Invitrogen, Carlsbad, CA, USA
RevertAid™ H Minus First Strand cDNA Synthesis Kit	Life Technologies, Carlsbad, CA, USA

4.8. Chemicals

Table 13: Chemicals used in this study

Chemical	Source
4',6-Diamidin-2-phenylindol (DAPI)	Life Technologies, Carlsbad, CA, USA
4% Paraformaldehyde	Life Technologies, Carlsbad, CA, USA
5-Bromo-4-chloro-3-indolyl β-D-glucopyranoside ($C_{14}H_{15}BrClNO_6$, X-Gal)	AppliChem GmbH, Darmstadt, Germany
Agarose	Biozym Scientific GmbH, Hessisch Oldendorf, Germany
Albumin from human serum	Merck KGaA, Darmstadt, Germany
Bacto Yeast Extract	BD Bioscience, Heidelberg, Germany
Bacto Agar	BD Bioscience, Heidelberg, Germany
Boric acid (H_3BO_3)	Fisher Scientific UK Ltd, Loughborough, Great Britain
Dako Fluorescence Mounting Medium	Agilent, Santa Clara, CA, USA
Dimethylsulfoxid (DMSO)	Carl Roth GmbH + Co. KG, Karlsruhe, Germany
dNTPs (dATP, dGTP, dCTP, dTTP)	Genaxxon Bioscience, Ulm, Germany
Epredia™ Neg-50™ Frozen Section Medium	Fisher Scientific GmbH, Schwerte, Germany
Ethanol ≥99,8 p.a, C_2H_6O	Carl Roth GmbH + Co. KG, Karlsruhe, Germany
Ethidium bromide solution 0.07 %	AppliChem GmbH, Darmstadt, Germany
Ethylendiamintetraacetate (EDTA)	Merck KGaA, Darmstadt, Germany
Glucose ($C_6H_{12}O_6$)	Merck KGaA, Darmstadt, Germany
Glutaraldehyd 25 %	Carl Roth GmbH + Co. KG, Karlsruhe, Germany
Hi-Di™ Formamid	Life Technologies, Carlsbad, CA, USA
Human BMP4 Recombinant Protein	Life Technologies, Carlsbad, CA, USA

Isopropanol (C$_3$H$_8$O)	Merck KGaA, Darmstadt, Germany
Magnesiumchloride (MgCl$_2$)	Merck KGaA, Darmstadt, Germany
Nuclease-free H$_2$O	Carl Roth GmbH + Co. KG, Karlsruhe, Germany
Pepton	Carl Roth GmbH + Co. KG, Karlsruhe, Germany
Potassium chloride (KCl)	Merck KGaA, Darmstadt, Germany
RDD buffer	Qiagen, Hilden, Germany
RNASE AWAY®	Molecular BioProducts Inc., San Diego, CA, US
Saccharose (C$_{12}$H$_{22}$O$_{11}$)	Merck KGaA, Darmstadt, Germany
Sodium azide (NaN$_3$)	Merck KGaA, Darmstadt, Germany
Sodium chloride (NaCl)	VWR International Germany GmbH, Darmstadt, Germany
Sodium dodecyl sulfate (SDS), ≥ 99% (C$_{12}$H$_{25}$NaO$_4$S)	VWR International Germany GmbH, Darmstadt, Germany
ß-Mercaptoethanol	AppliChem GmbH, Darmstadt, Germany
Tris(hydroxymethyl)aminomethane (Tris)	Affymetrix, Santa Clara, CA, US
Triton® X-100	AppliChem GmbH, Darmstadt, Germany
Trypan Blue Solution	Merck KGaA, Darmstadt, Germany

4.9. Antibodies

Table 14: Primary antibodies used in this study

Antibody	Clonality	Species	Dilution	Source
ATP1A3	mAb	mouse	1:500	ab2826, Abcam, Cambridge, UK
BEST1	mAb	mouse	1:500	ab2182, Abcam, Cambridge, UK
BRN3A	mAb	rabbit	1:250	ab245230, Abcam, Cambridge, UK
CALB1	mAb	mouse	1:1000	C9848, Merck KGaA, Darmstadt, Germany
CRX	mAb	mouse	1:1000	H00001406-M02, Abnova, Taipeh, Taiwan
KCNB1	mAb	mouse	1:800	K89/34, NeuroMab Facility, UC Davis, Davis, CA, USA
KI67	pAb	rabbit	1:100	ab15580, Abcam, Cambridge, UK
OPN1M/LW	pAb	rabbit	1:1000	JH492, gift from Jeremy Nathans, Johns Hopkins University, Baltimore, MD, USA
OPN1SW	pAb	rabbit	1:1000	JH455, gift from Jeremy Nathans, Johns Hopkins University, Baltimore, MD, USA
PRKCα	mAb	mouse	1:100	P5704, Merck KGaA, Darmstadt, Germany

PROX1	pAb	rabbit	1:4000	AB5475, Merck KGaA, Darmstadt, Germany
PRPH2	mAb	mouse	1:2	gift from Robert S. Molday, University of British Columbia, Vancouver, BC, Canada
RCVRN	pAb	rabbit	1:1000; 1:2000*	AB5585, Merck KGaA, Darmstadt, Germany
RHO1D4	mAb	mouse	1:1000	gift from Robert S. Molday, University of British Columbia, Vancouver, BC, Canada
RLBP1	mAb	mouse	1:500	ab15051, Abcam, Cambridge, GB
ROM1	mAb	mouse	1:2	gift from Robert S. Molday, University of British Columbia, Vancouver, BC, Canada
RS1	pAb	rabbit	1:1000	gift from Robert S. Molday, University of British Columbia, Vancouver, BC, Canada
SNCG	mAb	mouse	1:500	H00006623-M01, Abnova, Taipeh, Taiwan
TFAP2A	mAb	rabbit	1:250	ab108311, Abcam, Cambridge, UK
VSX2	pAb	rabbit	1:1000	HPA003436, Merck KGaA, Darmstadt, Germany
ZO-1	pAb	rabbit	1:500	61-7300, Life Technologies, Carlsbad, CA, USA

*dilution used for the RO embedding experiments only

Table 15: Secondary antibodies used in this study

Antibody	Dilution	Source
Alexa Fluor® 488 goat anti-rabbit IgG	1:667	Life Technologies, Carlsbad, CA, USA
Alexa Fluor® 594 goat anti-mouse IgG	1:667	Life Technologies, Carlsbad, CA, USA

4.10. Buffers

Table 16: Buffers used in this study

Buffer	Component	Amount
Blocking Solution	Goat Serum	10 % (v/v)
	Triton X-100	0.3 % (v/v)
	PBS	-
IPTG	IPTG	0.1 M
	H_2O dest.	-
Laird's buffer + SDS	Tris (0.5 M, pH 8.0)	10 % (v/v)

	NaCl (5 M)	4 % (v/v)
	EDTA (0.5 M, pH 8.0)	1 % (v/v)
	SDS 20 %	1 % (v/v)
	H_2O (Millipore)	-
Lysogeny Broth (LB) medium	Pepton	1 % (w/v)
	Yeast extract	0.5 % (w/v)
	NaCl	1 % (w/v)
	H_2O dest.	-
LB Agar	Pepton	1 % (w/v)
	Yeast extract	0.5 % (w/v)
	NaCl	1 % (w/v)
	Bacto Agar	15 % (w/v)
	H_2O dest.	-
Primary Antibody Solution	Goat Serum	2.5 % (v/v)
	TritonX-100	0.1 % (v/v)
	PBS	-
Secondary Antibody Solution	Goat Serum	2.5 % (v/v)
	DAPI	0.5 % (v/v)
	TritonX-100	0.1 % (v/v)
	Alexa Fluor® 594 goat anti-mouse IgG	0.15 % (v/v)
	Alexa Fluor® 488 goat anti-rabbit IgG	0.15 % (v/v)
	PBS	-
SOC Medium	Tryptone	2 % (w/v)
	Yeast extract	0.5 % (w/v)
	NaCl	10 mM
	KCl	2.5 mM
	$MgCl_2$	10 mM
	Glucose	20 mM
TBE	Tris	100 mM
	Boric acid	100 mM
	EDTA (pH 8.0)	1 mM
	H_2O dest.	-
X-Gal	X-Gal	0.04 % (w/v)
	DMSO	-

4.11.　　Cell Culture Media and Supplements

Table 17: Media and supplements used in this study

Component	Source
All-*trans* retinoic acid (ATRA)	Cayman Chemical, Michigan, USA
Ampicillin	Carl Roth GmbH + Co. KG, Karlsruhe, Deutschland
Antibiotic-Antimycotic (100x)	Life Technologies, Carlsbad, CA, USA
B27 Supplement	Life Technologies, Carlsbad, CA, USA

B27 Supplement without Vitamin A	Life Technologies, Carlsbad, CA, USA
Blebbistatin	Cayman Chemical, Michigan, USA
CloneR™	STEMMCELL Technologies Inc., Vancouver, BC, Canada
CryoStor® CS10	STEMMCELL Technologies Inc., Vancouver, BC, Canada
Dulbecco's Modified Eagle Medium (DMEM) Ham's F12 Medium	Life Technologies, Carlsbad, CA, USA
DMEM High Glucose Medium (4.5 g/L)	Life Technologies, Carlsbad, CA, USA
Dulbecco's PBS (DPBS)	Life Technologies, Carlsbad, CA, USA
Fetal Bovine Serum (FBS)	Life Technologies, Carlsbad, CA, USA
Fibronectin	Life Technologies, Carlsbad, CA, USA
Gentamicin (50 mg/ml)	Merck KGaA, Darmstadt, Germany
Gibco™ MEM Non-Essential Amino Acids Solution	Life Technologies, Carlsbad, CA, USA
GlutaMAX™	Life Technologies, Carlsbad, CA, USA
Ham's F-12 Nutrient Mix	Life Technologies, Carlsbad, CA, USA
Heat Inactivated Fetal Bovine Serum (HI-FBS)	Life Technologies, Carlsbad, CA, USA
Heparin sodium salt from porcine intestinal mucosa	Merck KGaA, Darmstadt, Germany
Hepes Buffer solution (1 M)	Life Technologies, Carlsbad, CA, USA
HyStem-C Hydrogel	Merck KGaA, Darmstadt, Germany
Inhibitor of Wnt response compound-1-endo (IWR-1e)	Merck KGaA, Darmstadt, Germany
Insulin-Transferrin-Selenium	Life Technologies, Carlsbad, CA, USA
Laminin	Cayman Chemical, Michigan, USA
L-Ascorbic Acid	Life Technologies, Carlsbad, CA, USA
L-Glutamine 200 mM (100x)	Life Technologies, Carlsbad, CA, USA
Matrigel® Growth Factor Reduced Basement Membrane Matrix	Corning, New York, NY, USA
Matrigel® hESC-qualified Matrix	Corning, New York, NY, USA
mTeSR™ Plus medium	STEMCELL Technologies Canada Inc., Vancouver, BC, CA
mTeSR™ Plus 5X Supplement	STEMCELL Technologies Canada Inc., Vancouver, BC, CA
mTeSR™ Plus Basal Medium	STEMCELL Technologies Canada Inc., Vancouver, BC, CA
Mycoplasma Removal Agent	Bio-Rad Laboratories Inc., Hercules, CA, USA
N-[N-(3,5-difluorophenacetyl-L-alanyl)]-S-phenylglycine t-butyl ester (DAPT)	Cayman Chemical, Michigan, USA
N2 Supplement	Life Technologies, Carlsbad, CA, USA
Nicotinamide	Merck KGaA, Darmstadt, Germany
Penicillin (10.000 units)/Streptomycin (10 mg/ml), (Pen/Strep)	Life Technologies, Carlsbad, CA, USA
Pyruvate	Cayman Chemical, Michigan, USA
Smoothened agonist (SAG)	Merck KGaA, Darmstadt, Germany
Taurine	Merck KGaA, Darmstadt, Germany
Vitronectin	Institute of Human Genetics, Regensburg, Germany*

Y-27632 RHO/ROCK pathway inhibitor	STEMCELL Technologies Canada Inc., Vancouver, BC, CA

*Purified Vitronectin was provided by Fabiola Biasella as described in (93)

Table 18: Cell culture stock solutions used in this study

Supplement	Solvent	Concentration	Storage Temperature
ATRA	DMSO	10 mM	-80 °C
Blebbistatin	DMSO	10 µM	-80 °C
BMP4	4 mM HCl + 0.1 % Albumin	1.5 nM	-80 °C
Heparin	H_2O (Millipore)	20 mg/ml	-20 °C
Taurine	H_2O (Millipore)	100 mM	-20 °C

4.12.   Consumables

Table 19: Consumables used in this study

Consumable	Source
24 well cell culture plate, sterile, with lid	Greiner Bio-One GmbH, Frickenhausen, Germany
25 cm^2 Flask (rectangular canted neck, with vent cap, ultra-low-attachment surface)	Corning, New York, NY, USA
96 well plate (ultra-low cluster, round bottom, ultra-low attachment)	Corning, New York, NY, USA
BD Microlance™ Cannulas 27 G 3/4 0,4x19 mm	Becton Dickinson, Franklin Lakes, USA
Bemis™ Parafilm™ M Laboratory Wrapping Film (PM-996)	Fisher Scientific GmbH, Schwerte, Germany
Cell scrapers, sterilized	TTP Techno Plastic Products AG, Trasadingen, Switzerland
CELLSTAR® Cell Culture 6 Well Plates	Greiner Bio-One, Kremsmuenster, Austria
Corning® 150 mL Vacuum Filter/Storage Bottle System, pore diameter: 0.22 µm	Corning, New York, NY, USA
Corning® Costar® Ultra-Low Attachment 96 Well Plate	Merck KGaA, Darmstadt, Germany
Corning™ Costar™ Ultra-Low Attachment 24 Well Plates	Life Technologies, Carlsbad, CA, USA
Disposable nitrile examination gloves, powder free	Paperlynen GmbH, Krailling, Germany
ep Dualfilter T.I.P.S® filter tips, 20 – 300 µl	Eppendorf AG, Hamburg, Germany
Filter tips 0 – 100 µl	nerbe plus GmbH & Co. KG, Winsen/Luhe, Germany
Filter tips 100 – 1250 µl	nerbe plus GmbH & Co. KG, Winsen/Luhe, Germany
Filter tips, super slim, 0.1 – 10 µl	nerbe plus GmbH & Co. KG, Winsen/Luhe, Germany
Filtropur V25, Vacuum filtration unit, 250 ml, PES, 0.2 µm	SARSTEDT AG & Co. KG, Nuembrecht, Germany

Filtropur V50, Vacuum filtration unit, 500 ml, PES, 0.2 µm	SARSTEDT AG & Co. KG, Nuembrecht, Germany
Micro tube 0.5 ml SafeSeal	SARSTEDT AG & Co. KG, Nuembrecht, Germany
Micro tube 2.0 ml SafeSeal	SARSTEDT AG & Co. KG, Nuembrecht, Germany
MicroAmp™ Optical 384-Well Reaction Plate	Life Technologies, Carlsbad, CA, USA
MicroAmp™ Optical Adhesive Film	Life Technologies, Carlsbad, CA, USA
Multiply®-µStrip, 0.2 ml chain	SARSTEDT AG & Co. KG, Nuembrecht, Germany
PARAFILM® M Sealing foil	A. Hartenstein
Petridish (10 cm)	SARSTEDT AG & Co. KG, Nuembrecht, Germany
Pipet 5 ml disposable, glass, serological, sterile	Corning, New York, NY, USA
Pipette 10 ml, sterile, single packed	Greiner Bio-One GmbH, Frickenhausen, Germany
Pipette 25 ml, sterile, single packed	Greiner Bio-One GmbH, Frickenhausen, Germany
Pipette 50 ml, sterile, single packed	SARSTEDT AG & Co. KG, Nuembrecht, Germany
Pipette tips, 0,1 – 20 µl	nerbe plus GmbH & Co. KG, Winsen/Luhe, Germany
Pipette tips, 1 – 200 µl	VWR International, West Chester, PA, US
Pipette tips, 100 – 1250 µl	nerbe plus GmbH & Co. KG, Winsen/Luhe, Germany
PTFE-membrane	Merck KGaA, Darmstadt, Germany
QIAshredder® Collums	Qiagen, Hilden, Germany
Reagent reservoir, 25 ml, disposable, pre-sterile	VWR International, West Chester, PA, US
Safe-Lock Tubes (1.5 ml)	Eppendorf AG, Hamburg, Germany
Single use embedding molds	PLANO GmbH, Wetzlar, Germany
Sterile 50 ml Disposable Vacuum Filtration System, 0.45 µm Durapore®	Merck KGaA, Darmstadt, Germany
SuperFrost®Plus Microscope slides	VWR International BVBA, Leuven, BE
Syringe (1 ml)	Becton Dickinson, Franklin Lakes, USA
TC-dish, 100, standard	SARSTEDT AG & Co. KG, Nuembrecht, Germany
TC-plate, 6 well, standard	SARSTEDT AG & Co. KG, Nuembrecht, Germany
ThinCert™ 12 well plate, with lid, sterile	Greiner Bio-One GmbH, Frickenhausen, Germany
ThinCertTM Cell culture insert for 12 well plates, sterile, pore diameter: 0.4 µm	Greiner Bio-One GmbH, Frickenhausen, Germany
Tube, 15 ml, PP, conical bottom, CELLSTAR®, sterile	Greiner Bio-One GmbH, Frickenhausen, Germany
Tube, 50 ml, PP, conical bottom, CELLSTAR®, sterile	Greiner Bio-One GmbH, Frickenhausen, Germany

4.13. Instruments

Table 20: Instruments used in this study

Instrument	Source
Abi3130x1 Genetic Analyzer	Applied Biosystems, Waltham, MA, USA
Amaxa Nucleofector Electroporation device	Lonza Bioscience, Basel, Switzerland
Autoclave V-150	Systec GmbH, Wattenberg, Germany
BlueMarine 200 Electrophoresis chamber	SERVA Electrophoresis GmbH, Heidelberg, Germany
BluePower Plus Power supply unit	SERVA Electrophoresis GmbH, Heidelberg, Germany
Brady BMP61	Brady, Milwaukee, WI, USA
CASY® Cell counter and analyzer	Innovatis Roche AG, Bielefeld, Germany
Centrifuge 5415 R	Eppendorf AG, Hamburg, Germany
Centrifuge 5810	Eppendorf AG, Hamburg, Germany
Centrifuge Megafuge 1.0R	Heraeus Holding GmbH, Hanau, Germany
CO_2-Incubator Binder CB 160	Binder GmbH, Tuttlingen, Germany
CO_2-Incubator Binder CB 210	Binder GmbH, Tuttlingen, Germany
CO_2-Incubator Heraeus instruments	Heraeus Holding GmbH, Hanau, Germany
Cold microtom Leica CM1850	Leica, Solmis, Germany
Compact shaker KS 15	Edmund Bühler GmbH, Bodelshausen, Germany
Ender-3 V2 3D Printer	Shenzhen Creality 3D Technology Co., Ltd, Shenzhen, China
Ice Maker Machine KBS	KBS Gastrotechnik GmbH, Wiesbaden, Germany
Ice Machine AF 100	Scotsman, Vernicht Hills, IL, USA
Incubator for bacteria 37°C	Memmert GmbH, Schwabach, Germany
Incubator hood TH 15	Edmund Bühler GmbH, Boden, Germany
Microscope Nikon Eclipse TE2000-S	Nikon Instruments Europe BV, Amstelveen, the Netherlands
Microscope Nikon Eclipse TS100	Nikon Instruments Europe BV, Amstelveen, the Netherlands
Microwave oven Clatronic® MW 786	Clatronic International GmbH, Kempen, Germany
Milli-Q-Synthesis Water Purification System	Merck Chemicals GmbH, Schwalbach, Germany
Mini-centrifuge for strips D-6015	neoLab Migge GmbH, Heidelberg, Germany
NanoDrop® ND1000 Spectrophotometer	NanoDrop, Wilmington, Germany, USA
Neubauer counting chamber	Carl Roth GmbH + Co. KG, Karlsruhe, Germany
Olympus Flouview FV3000	Olympus Life Sciences, Hamburg, Germany
pH Meter Lab 850	SI Analytics GmbH, Mainz, Germany
QuantStudio® 5 Real-Time PCR System	Life Technologies, Carlsbad, CA, USA
Scales	SCALTEC Instruments GmbH, Heiligenstadt, Germany
Spark® Multimode Microplate Reader	Tecan Trading AG, Switzerland
The belly dancer® orbital shaker	Merck KGaA, Darmstadt, Germany

Thermocycler peqSTAR 2x Gradient	VWR International GmbH, Darmstadt, Germany
Thermocycler T1 Plus	Biometra GmbH, Goettingen, Germany
Thermocycler T3	Biometra GmbH, Goettingen, Germany
Thermomixer compact	Eppendorf AG, Hamburg, Germany
Tissue Lyser II	Qiagen GmbH, Hilden, Germany
Transferpipette® 10 µl	Brand, Wertheim, Germany
Transferpipette® 100 µl	Brand, Wertheim, Germany
Transferpipette® 1000 µl	Brand, Wertheim, Germany
Transilluminator UST-30M-8R	BioView Ltd., Billerica, MA, USA
UVP GelStudio PLUS	Analytik Jena GmbH, Jena, Germany
Vacuum pump MZ 2 C	Vacuubrand GmbH, Wertheim, Germany
Vortex Genie2	Scientific Industries, Bohemia, NY, USA
Water bath W12	Labortechnik Medingen, Arnsdorf, Germany

4.14. Software

Table 21: Software used in this study

Software	Source
Flouview FV3000	Olympus Life Sciences, Hamburg, Germany
CorelDraw	Corel Corporation, Ottawa, Canada
Microsoft Office	Microsoft Cooperation, Redmond, WA, USA
Snap Gene	GSL Biotech LLC, San Diego, CA, USA
Chromas	Technelysium Pty Ltd, South Brisbane, AU
FIJI	Wayne Rasband, National Institutes of Health, USA

5. Methods

5.1. iPSC Culture

Eleven iPSC lines were used in this study (Table 1-2). Four iPSC lines were reprogrammed from healthy donors with no history of retinal pathology (HD #1 - 4). Three iPSC lines were reprogrammed from individuals with retinitis pigmentosa type 1, harboring autosomal dominant mutations in the *RP1* gene (adRP1 #1-4). Four additional iPSC lines were generated using CRISPR/Cas9 treatment, targeting the 2nd exon of *RP1* (see also section 5.6). All iPSC lines were reprogrammed at the Institute of Human Genetics, except for HD #4 which was reprogrammed and kindly provided by Dr. Vladimir Milenkovic (Department of Psychiatry and Psychotherapy, University of Regensburg).

5.1.1. Reprogramming[2]

The isolation of adult human PBMCs and dermal fibroblasts, followed by reprogramming to iPSC (approved by the local ethics committee reference no. 11-101-0228) were conducted according to ref. (94) with modifications as per ref. (95) with additional minor modifications. iPSC lines HD #1 - 2 and adRP1 #1 - 3 were reprogrammed via polycistronic lentiviral transduction utilizing the Human STEMCCA Cre-Excisable Constitutive Polycistronic (OKS/L-Myc) Lentivirus Reprogramming Kit (Sigma-Aldrich, St. Louis, USA) according to the manufacturer's instructions. iPSC line HD #3 was reprogrammed with episomal plasmids pCBX-EBNA, pCE-hSK, pCE-hUL, pCE-hOCT3/4, and pCE-mp53DD (kindly provided by Shinya Yamanaka or purchased from Addgene, Massachusetts, USA: #41857, #41814, #41855, #41813, and #41856 (95,96)). Reprogramming was conducted using the Human Dermal Fibroblast NucleofectorTM Kit VPD-1001 (Lonza, Basel, Switzerland) on the Amaxa Nucleofector Electroporation device (program U-23).

5.1.2. Maintenance

iPSCs were maintained in mTeSR™ Plus medium with Gentamycin (25 µg/ml, mTeSR_G), and the medium was changed daily. Spontaneously differentiated cells were identified and removed via suction during the medium exchanges and prior to

---

[2]This section was adapted from Berber et al. (161).

passaging. iPSCs were passaged 1:2 – 1:5 once they reached a confluency of 50 - 80 %. To passage the iPSCs, the cells were washed using 2 mL DPBS, and then incubated in 1 mL Dispase at 37 ºC for 5 minutes. The Dispase was gently removed and the iPSCs were washed with 2 mL DPBS. The appropriate volume of mTeSR_G medium was added depending on the split ratio, which was determined by the confluency and rate of spontaneous differentiation. The iPSCs were detached from the well surface by gently scratching using a serological pipette followed by a cell scraper. The detached iPSCs were resuspended and transferred to Corning® Matrigel® hESC-qualified Matrix-coated 6 well plates.

For the coating, Matrigel® was solved in cold DMEM/F12, according to the dilution recommended by the manufacturer. The plates were incubated in the Matrigel®/DMEM/F12 mixture for at least 60 minutes at room temperature (RT), or 30 minutes at 37 ºC. Coated plates were stored at 4 ºC for up to 7 days.

5.1.3. Cryo-preservation

For long term storage, iPSCs were cryo-preserved in liquid nitrogen. To cryo-preserve the iPSCs, the method for passaging was followed until the iPSCs were detached from the wells. The iPSCs were transferred to a collection tube and centrifuged at 300 relative centrifugal force (rcf) for 5 minutes. The supernatant was removed, and the cell pellet was gently resuspended in 1 mL CryoStor® CS10. The resuspended cells were frozen at -80 ºC in Styrofoam overnight (ON) and transferred to a liquid nitrogen tank.

iPSCs were thawed by placing the vial in a 37 ºC water bath until almost melted and transferred to a collection tube containing 9 mL DMEM/F12. After centrifugation at 300 rcf for 5 minutes, the supernatant was removed, and the cell pellet was resuspended in 1mL mTeSR_G medium. The cells and medium were transferred to fresh Matrigel®-coated 6 well plates. The iPSCs were treated with Mycoplasma Removal Agent (1:100) daily for 7 days after thawing.

5.1.4. Demonstration of Pluripotency

The pluripotency of 1-2 clones from iPSC lines HD #1-2, 4 and adRP1 #1-3 (11 samples total) were confirmed via PluriTest®, a patented bioinformatic-based assay which analyses the pluripotency of cells based on their gene expression profiles (97,98). To prepare for the PluriTest, RNA samples were isolated from an aliquot of

iPSCs by following the procedure for passaging until the iPSC were detached from the wells. The iPSCs were transferred to a collection tube and centrifuged at 300 rcf for 5 minutes. The supernatant was discarded, and the cell pellet was frozen at -80 ºC. The procedure for RNA isolation was performed as described in section 5.4.1.

The PluriTest was executed by Dr. Tanja Rothhammer-Hampl (Department of Neuropathology, Regensburg University Hospital). Briefly, NGS data from all 11 iPSC samples were mapped to previously generated data sets from 70 pluripotent samples and 300 non-pluripotent samples (somatic and differentiated cells including brain tissue, glioblastoma, fetal tissue, differentiated embryonic stem cells and non-pluripotent stem cell samples) (98). Previously defined empirical pluripotency threshold score of 1450 and novelty threshold score of 2.43 were applied, which identify pluripotent cells with a specificity of 100 % and sensitivity of 82.61 % (98). According to this analysis, 10 of the 11 iPSC lines were pluripotent (Figure 8A and Supp. Figure 1). Only one sample (adRP1 #2 clone 287) did not meet the empirical cutoffs (Figure 8B). Of note, this sample met the slightly more lenient statistical threshold scores (pluripotency score cut-off: 961.24 and novelty score cut-off: 2.54) which have a lower specificity of 87,9 % (98). The second clone of this iPSC line met the empirical thresholds (Supp. Figure 1G).
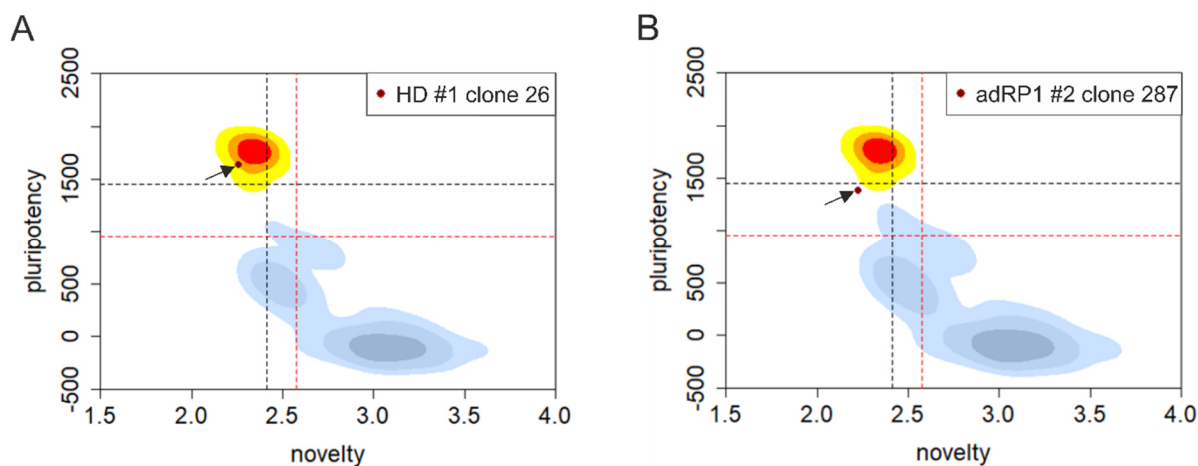
Figure 8: PluriTest results from two iPSC samples. Scatterplots showing the PluriTest results from (**A**) iPSC line HD #1 clone 26 and (**B**) iPSC line adRP1 #2 clone 287 are shown. The iPSC lines are shown as dark red points and emphasized with black arrows. HD #1 clone 26 met the strict empirical thresholds (shown as black dotted lines) whereas adRP1 #2 clone 287 only met the more lenient statistical thresholds (shown as red dotted lines). Kernel density estimations for embryonic stem cells and nuclear transfer iPSCs (yellow to red) and somatic/differentiated cells (light blue to dark grey) are shown.

5.2. RO and RPE Differentiation[3]

ROs were differentiated from iPSCs using adaptations of three previously published methods: method 1 (M1; (45)), method 2 (M2; (59)), and method 3 (M3; (48)).

5.2.1. RO Differentiation M1

ROs were differentiated according to Wahlin et al. (45) with minor modifications. All cells were cultured under normoxia. On day 0, iPSCs were treated with StemPro™ Accutase™ for 9 minutes, and 2,000 cells per well were plated on a Corning® Costar® Ultra-Low Attachment 96 Well Plate in mTeSR™ Plus medium with 5 µm Blebbistatin. Cells were weaned onto BE6.2 medium (Tables 22 and 23). Three µM Inhibitor of Wnt response compound-1-endo (IWR-1e) was added to the medium until day 7, and 1 % Corning® Matrigel® Growth Factor Reduced Basement Membrane Matrix (Matrigel-GFR) was added until day 8.

Table 22: BE6.2 medium composition

Component	Amount
high glucose DMEM	base
E6 Stock (Table 23)	4 %
B27 Supplement without Vitamin A	2 %
L-Glutamine	1 %
MEM Non-Essential Amino Acids Solution	1 %
Pyruvate	1 %
Insulin-Transferrin-Selenium	1 %

Table 23: E6 stock composition

Component	Amount
H_2O (Millipore)	base
NaHCO3	7.5 %
L-ascorbic acid	11 mM

On day 10, the aggregates which formed retinal domains were counted, and isolated with 27G cannulas attached to 1 mL syringes. Thereafter, the ROs were cultured in separate wells of Corning™ Costar™ Ultra-Low Attachment 24 Well Plates as per Hallam et al. (99). From day 10 until day 18, 100 nM SAG was added to the

---

[3]The sections 5.2.1 – 3 were adapted from Berber et al. (161).

medium. On day 12, the medium was switched to LTR medium (Table 24). After day 20, 500 nM all-trans retinoic acid, and from day 29 until day 42 10 µM DAPT, was added to the medium.

Table 24: LTR medium composition

Component	Amount
high glucose DMEM	base (3 parts)
Ham's F-12 Nutrient Mix	base (1 part)
HI-FBS	10 %
B27 Supplement	2 %
L-glutamine	1 %
MEM Non-Essential Amino Acids Solution	1 %
Pyruvate	1 %
Taurine	1 mM

5.2.2. RO Differentiation M2

ROs were differentiated according to Zhong et al. (59) with minor modifications. On day 0, iPSCs were treated with Dispase for 15 minutes and transferred to Corning® Ultra-Low attachment cell culture flasks in mTeSR™ Plus medium with 10 µM Blebbistatin to facilitate aggregate formation. Over the course of 3 days, the aggregates were weaned onto NIM medium (Table 25). The medium was changed on day 6, and on day 7 the aggregates were plated on Matrigel-GFR Basement Membrane Matrix coated CELLSTAR® cell culture 6 well plates. Plates were coated with Matrigel-GFR following the same procedure as the Matrigel coating, with one exception: the Matrigel-GFR solution was suspended 1:30 in Knockout™ DMEM.

Table 25: NIM medium composition

Component	Amount
high glucose DMEM	base (1 part)
Ham's F-12 Nutrient Mix	base (1 part)
N2 Supplement	1 %
GlutaMAX™ Supplement	1 %
MEM Non-Essential Amino Acids Solution	1 %
Heparin	2 µg/mL

Half the medium was exchanged for fresh NIM every three days. On day 16, the medium was switched to RDM medium (Table 26). On day 23, the retinal domains were counted. 10 mM HEPES was added to the medium, and the ROs were isolated

as described in M1 and transferred to separate wells of a Corning® Costar® Ultra-Low Attachment 96 Well Plate as per Hallam et al. (99). On day 43, the medium was switched to RC2 medium (Table 27). From day 63 until day 90, 1 µM ATRA was added to the medium 5 times weekly. On day 91 the medium was switched to RC1 medium (Table 28).

Table 26: RDM medium composition

Component	Amount
high glucose DMEM	base (3 parts)
Ham's F-12 Nutrient Mix	base (1 part)
B27 Supplement without Vitamin A	2 %
GlutaMAX™ Supplement	1 %
MEM Non-Essential Amino Acids Solution	1 %
Antibiotic-Antimycotic	1 %

Table 27: RC2 medium composition

Component	Amount
high glucose DMEM	base (3 parts)
Ham's F-12 Nutrient Mix	base (1 part)
HI-FBS	10 %
B27 Supplement	2 %
GlutaMAX™ Supplement	1 %
MEM Non-Essential Amino Acids Solution	1 %
Antibiotic-Antimycotic	1 %
Taurine	100 µM

Table 28: RC1 medium composition

Component	Amount
DMEM/F-12, GlutaMAX™ Supplement	base
HI-FBS	10 %
N2 Supplement	1 %
MEM Non-Essential Amino Acids Solution	1 %
Antibiotic-Antimycotic	1 %
Taurine	100 µM

5.2.3. RO Differentiation M3

ROs were differentiated as described in M2, with a single modification: on day 6, 1.5 nM BMP4 was added to the medium as demonstrated by Kuwahara et al. (48) and Capowski et al. (47).

5.2.4. RPE Differentiation and Culture

The RO M3 differentiation protocol was adapted to acquire RPE (termed byproduct RPE, bRPE) in addition to ROs using a method developed in the course of this thesis and separately validated in two medical theses (Sofiia Bondarenko and Ricarda Bühler, Institute of Human Genetics, University of Regensburg).

After the retinal domains were excised from the cell culture plates, the remaining cells were cultured in RDM with 1.2 mg/mL nicotinamide until day 42. On day 42, pigmented cells were mechanically isolated using cannulas under an inverted brightfield microscope and incubated in TrypLE at 37 ºC for 15 minutes in a water bath. The bRPE cells were centrifuged at 300 rcf for 5 minutes and the supernatant was removed. Some bRPE samples were transferred to -80 ºC for downstream RNA isolation followed by qRT-PCR (sections 5.4.1-2). The remaining cell pellets were resuspended in RC2 medium with 1.2 mg/mL nicotinamide. The bRPE were cultured on Matrigel GFR-coated plates until day 75 (± 5 days), when they were passaged 1:3 or 1:6, depending on the confluency of the cells. Plates were coated with Matrigel GFR-coating as described in section 5.5.2. During passaging, the bRPE were washed once with DPBS and incubated in TrypLE for 25 - 45 minutes at 37 ºC, until they detached from the wells by moderately forceful pipetting. The bRPE were centrifuged at 300 rcf for 5 minutes, the supernatant was removed, and the pellet was resuspended in RC2 medium with 1.2 mg/mL nicotinamide. The bRPE were seeded on Matrigel GFR-coated plates, and the medium was changed two to three times weekly, depending on the confluency of the cells. After day 91, the bRPE were cultured in RC1 medium with 1.2 mg/mL nicotinamide, and the medium was changed two to three times weekly, depending on the confluency of the cells. On day 105, the bRPE were cryo-preserved by following the procedure for passaging until the centrifugation step. Thereafter, the procedure for iPSC cryo-preservation and thawing was followed, with the following modification: RC1 medium with 1.2 mg/mL nicotinamide was used instead of mTeSR_G medium. Optionally, on day 105 some samples were transferred to -80 ºC for downstream RNA isolation followed by qRT-PCR (sections 5.4.1-2).

To evaluate the polarization of bRPE, they were cultured on transwell filters. To prepare for the transwell culture, the bRPE were thawed following the procedure for iPSC with one modification: the bRPE were resuspended in RC1 medium with 1.2 mg/mL nicotinamide instead of mTeSR_G medium. The resuspended bRPE were

cultured on Matrigel-GFR coated 6 well plates for 4 weeks. Thereafter, the bRPE were passaged as described previously, and seeded 1:12 onto Matrigel-GFR coated 12 well transwell filters. Medium was exchanged twice a week. After 6 weeks, the bRPE were harvested for ICC (section 5.3.1-2), or RNA isolation followed by cDNA synthesis and qRT-PCR (sections 5.4.1-2).

5.3. Immunocytochemistry (ICC)

5.3.1. Sample Preparation

Prior to the initiation of the harvest protocol, the correct age of the ROs was confirmed on https://www.calculator.net/age-calculator.html. ROs were harvested on the exact day the correct age was reached with very few exceptions (± 1 day). Brightfield images of each RO were taken on a Nikon Eclipse TE2 microscope.

To prepare for ICC, the ROs were rinsed in DPBS, and fixed in 4 % paraformaldehyde (PFA) for 30 minutes. The fixed ROs were washed three times in DPBS for 5 minutes and incubated in 6.75 % sucrose in DPBS (w/v) for 1 hour at RT, followed by another hour at RT in 12.5 % sucrose. The 12.5 % sucrose was replaced by 25 % sucrose and the samples were incubated while gently rocking ON at 4 ºC. The next day, the 25 % sucrose was replaced by 1:1 Epredia™ Neg-50™ Frozen Section Medium and 25 % sucrose and incubated for 1 hour at RT while gently rocking. Samples were rinsed briefly in Neg-50^{TM} and transferred to single use embedding molds in fresh Neg-50$^{TM.}$ The embedded ROs were frozen at -20 ºC and transferred to -80 ºC for long term storage.

Prior to cryo-sectioning, the embedded ROs were acclimatized to -20 ºC for at least 30 minutes. The entire RO was cryosectioned into 10 µm sections and the sections were distributed evenly on 8 SuperFrost Plus Adhesion Slides. Each slide contained two serial cryosections from as many positions in the RO as possible, given the variable RO size.

The bRPE on transwell filter inserts were rinsed with DPBS and fixed in 4 % PFA for 10 minutes. The fixed filters were washed three times in DPBS for 5 minutes and stored at 4 ºC for a maximum of 7 days prior to staining.

5.3.2.ICC

RO cryosections and bRPE filter inserts were immunostained in containers custom-made by Andreas Berber, M.Sc. (Krones AG; Figure 9A, B). Scaffolds for the slides were printed with an Ender-3 V2 3D Printer (Shenzhen Creality 3D Technology Co., Ltd). The containers were equipped with a thermometer and hygrometer which could be monitored via Bluetooth (Brifit). The lid of each container was painted black to protect the slides from light.
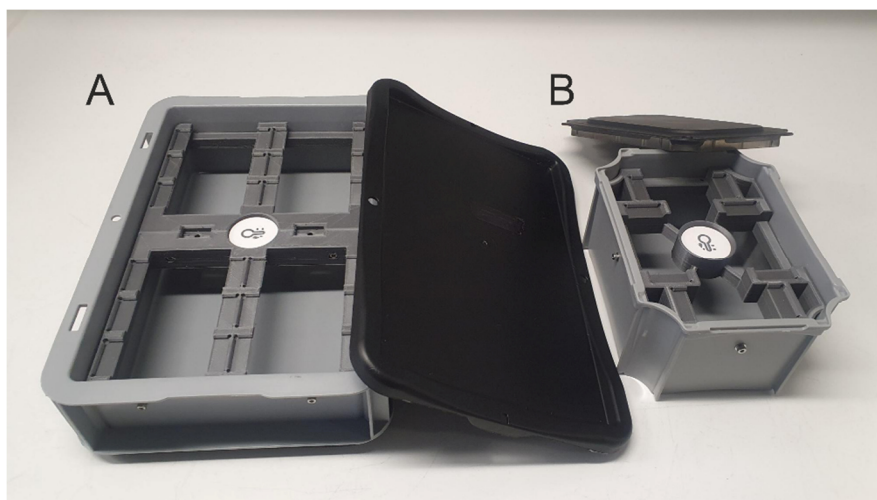
Figure 9: ICC containers. ICC was conducted in (**A**) a large container, which fit 12 object slides (7 cm x 20 cm x 30 cm), or (**B**) a small custom container, which fit 4 object slides (8.5 cm x 13 cm x 18 cm).

RO cryosections and bRPE filters were incubated in the blocking solution (Table 16) at RT for 60 or 25 minutes, respectively. The blocking solution was removed and replaced with the primary antibody solution (Table 14, 16) and incubated for one day at 8 ºC. The primary antibody was removed, and the slides were washed with DPBS three times for 5 minutes. Slides were incubated ON at 8 ºC in the secondary antibody solution (Table 15, 16) which was aliquoted and stored at -20 ºC until use. The secondary antibody solution was removed, and the slides were washed with DPBS three times for 5 minutes. Slides were mounted in Dako Fluorescence Mounting Medium and dried ON before imaging. As a negative control, the primary antibody was omitted from one cryosection per RO per immunostaining.

5.3.3.Imaging[4]

All slides were imaged on a confocal microscope Olympus Flouview FV3000. The confocal microscope was funded by a grant (INST 89/506-1 FUGG, 91b GG) from the Deutsche Forschungsgemeinschaft (DFG). To control for regional variability, images were acquired of whole organoid cryosections at 10x magnification. At least three cryosections were imaged per RO. In some cases, the cryosections were larger than the field of view of the microscope, so multiple images were taken and subsequently joined together (known as stitching). Parameters for the scan size, zoom, detector selection, laser intensity, voltage, gain and offset remained constant during each experimental series. For demonstration purposes, some closeup images of RO sections and bRPE were taken in 10x, 20x or 40x magnifications. Z-stacks were imaged at 40x magnification.

5.3.4.Analysis

On average, 4.7 ROs were analyzed per condition and timepoint (minimum 2, maximum 9). The relative area of the immunostainings was calculated relative to the Dapi-positive area for the following nuclear markers: Transcription factor AP-2 alpha (TFAP2A), POU class 4 homeobox 1 (BRN3A), CRX, Marker of proliferation Ki-67 (Ki67), and Synuclein gamma (SNCG). To determine the relative proportion of rod photoreceptors, the RHO-positive area was calculated and compared to the Recoverin-positive (RCVRN) area, as follows. Macros were written for the quantification, which converted the images to 16 bits, performed thresholding according to ref. (100), and the remaining area was measured. The average of all imaged cryosections from one RO were calculated. All quantifications were implemented in Fiji, an updated distribution of ImageJ (101).

5.3.5.Statistics

The median was calculated for at least three cryosections or three images per RO per condition. The Kolmogorov-Smirnov test was used to test for normality (102). To test for significance, a one-way ANOVA test, post hoc Tukey test, and Bonferroni correction for multiple comparisons were performed (103,104).

---

[4]The sections 5.3.3 – 5 were adapted from Berber et al. (161).

5.4. Investigations into mRNA Expression

5.4.1. RNA Isolation

RNA was isolated from iPSCs and bRPEs using the PureLink™ RNA Mini Kit according to the manufacturer's instructions with some minor modifications: All samples were suspended in Lysis Buffer with 1% ß-Mercaptoethanol. Cells were lysed in QIAshredder® columns or with a Tissue Lyser II and a clean metal bead. The manufacturer's instructions were followed until the first wash step, at which point the columns were incubated in 20 µl RNAse-Free DNAse suspended in 70 µl RDD Buffer for 15 minutes at RT. Thereafter, the manufacturer's instructions were followed until the samples were eluted twice in nuclease-free H_2O.

RNA was also isolated from ROs with the PureLink™ RNA Micro Scale Kit according to the manufacturer's instructions with minor modifications. ROs harvested for RNA isolation were rinsed once with DPBS and snap frozen on dry ice. Samples were stored at -80 ºC. The ROs were lysed via aspiration using syringes and 20G needles, in Lysis Buffer with 1 % ß-Mercaptoethanol. Samples were eluted in nuclease-free H_2O. The RNA concentration and purity of all RNA samples was measured on a NanoDrop® spectrometer, and the samples were transferred to -20 ºC for short term or -80 ºC for long term storage.

5.4.2. Reverse Transcription and qRT-PCR

For cDNA synthesis, 500 ng total RNA (for ROs) or up to 1 µg total RNA (for bRPE and iPSC) were reverse transcribed with the RevertAid™ First Strand cDNA Synthesis Kit. First, 1 µl Random Hexamer Primer was added to the sample and incubated according to Table 29 (step 1). The samples were immediately cooled on ice. cDNA synthesis was executed using the reaction mixture shown in Table 30 and thermocycler program shown in Table 29 (step 2). cDNA samples were diluted to 20 ng/µl with RNAse free H_2O and stored at -20 ºC.

Table 29: Thermocycler program for cDNA synthesis

Reaction Step	Temperature	Duration
Step 1: Annealing	65 ºC	5 min
	25 ºC	10 min
Step 2: cDNA synthesis and heat inactivation	42 ºC	60 min
	70 ºC	10 min

Table 30: Reaction mixture for cDNA synthesis. Volumes for one sample are shown.

Component	Volume
5X reaction buffer for RevertAid™ Reverse Transcriptase	4 µl
dNTPs (1.25 mM)	2 µl
RevertAid™ Reverse Transcriptase	1 µl

qRT-PCR was performed in technical duplicates or triplicates according to the reaction mixture shown in Table 31. Reactions were conducted in a MicroAmp™ Optical 384-Well Reaction Plate on a QuantStudio® 5 Real-Time PCR Systems for 40 cycles according to the settings shown in Table 32.

Table 31: Reaction mixture for qRT-PCR. Volumes for one sample are shown.

Component	Volume
Taykon Low ROX Probe 2x MasterMix dTTP blue	5 µl
Primer forward (1:10 dilution)	1 µl
Primer reverse (1:10 dilution)	1 µl
Probe (1:4 dilution)	0.125 µl
H_2O (Millipore)	0.375 µl
cDNA (20 ng/µl)	2.5 µl

Table 32: Thermocycler program for qRT-PCR.

Reaction Step	Temperature	Duration
Step 1: Denaturation	95 ºC	40 seconds
Step 2: Annealing	60 ºC	60 seconds
Step 3: Elongation	72 ºC	120 seconds

Data were analyzed according to the ΔΔCt approach (105). Measurements with a SD greater than 0.4 Ct values were excluded. Expression was first normalized to the expression of housekeeper gene Hypoxanthine Phosphoribosyltransferase 1 (HPRT1), followed by normalization to the mean Ct value in iPSC samples. To test for significance, a one-way ANOVA test, post hoc Tukey test, and Bonferroni correction for multiple comparisons were performed (103,104). Some qRT-PCR replicates were conducted in medical theses (Sofiia Bondarenko and Ricarda Bühler, Institute of Human Genetics, University of Regensburg), and analyzed in parallel to replicates executed as part of this thesis.

5.4.3. Library Preparation and NGS

cDNA libraries were prepared from 48 ROs (Figure 10). cDNA libraries were prepared in batches containing samples from each maturation stage and the adRP1 #1 samples were processed in parallel to samples from HD #1 and #2. If possible, 600 ng total RNA was purified per sample. Thirteen samples did not yield 600 ng of RNA, so the maximum amount possible was used instead (at least 216 ng). The samples were purified using NEXTFLEX® Poly(A) Beads. Libraries were processed with the NEXTFLEX® Rapid Directional RNA-Seq Library Prep Kit according to manufacturer's instructions, using NEXTFLEX® RNA-Seq Barcodes 1 - 48. Fifteen PCR cycles were performed.
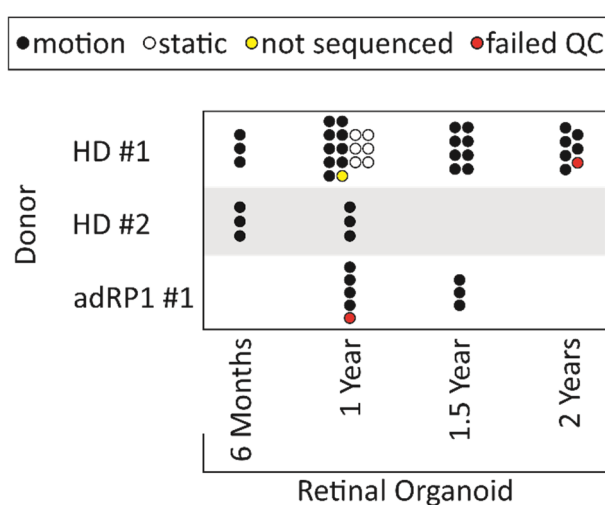
Figure 10: RNA-seq sample overview. A sample overview of the 48 ROs used for RNA seq is shown. Each RO is represented by a circle. ROs were cultured on an orbital shaker (black circles) or stationary (white circles). One RO did not yield a detectable peak in the final library evaluation and was not sequenced (HD #1, 1-year, represented by a yellow circle). Two ROs failed the quality control parameters set during data analysis (HD #1, 2-year, and adRP1 #1, 1-year, represented by red circles).

The size distribution and concentration of each final library preparation was evaluated using a Bioanalyzer High Sensitivity DNA Assay (Agilent Technologies). One sample did not yield a detectable peak, so it was excluded from sequencing which was conducted by the Kompetenzzentrum für Fluoreszente Bioanalytik (Head: Dr. Thomas Stempfl, University of Regensburg) on an Illumina NextSeq 2000 with a P3-50 Flow Cell, single-end. On average, 24.6 ± 3 million reads were generated per sample.

The analysis of NGS data for the identification of differentially expressed genes (DEGs) was performed by Dr. Tobias Strunz (Institute of Human Genetics, University of Regensburg; section 8.2). All subsequent analyses were part of this thesis.

Gene enrichment analyses were executed for gene ontology biological process (GO:BP) pathways using g:Profiler (version e104_eg51_p15_3922dba) with a significance threshold of 0.01 (106). Markers used for cell type specific heatmaps were manually curated from literature (107,108) and cross-referenced with The Human Protein Atlas (109–111). Markers which could not be assigned to a specific cell type to a reasonable degree of certainty were excluded from further analysis. Boxplots of VST normalized expression data were created in Excel.

5.5. bRPE and RO Coculture

Multiple techniques for bRPE and RO coculture were tested: coculture with bRPE grown on transwell filters with or without the addition of ECM-like compounds or a PTFE-membrane, coculture with dissociated bRPE with or without the addition of blebbistatin or adhesive glycoproteins, and coculture with bRPE suspended in Matrigel-GFR. The coculture on transwell filter inserts (without the ECM-like compounds or PTFE-membrane) and coculture with dissociated bRPE (with blebbistatin) were validated separately in a medical thesis (Sofiia Bondarenko, Institute of Human Genetics, University of Regensburg).

For the coculture on transwell filter inserts, bRPE were cultured as described previously (section 5.2.4). The RO were gently added to the filter inserts and incubated for at least 2 days. The RO spontaneously detached from the inserts while handling, during medium changes, and/or during fixation. After detachment, the filter inserts were stained with Tight junction protein 1 (ZO-1) and RHO as described in section 5.3.2. Optionally, 200 µl Matrigel-GFR or 200 µl hyaluronic acid-based hydrogel HyStem-C was added to the coculture, according to ref. (112). Optionally, a PTFE-membrane was added on top of the RO to stabilize the coculture, according to ref. (113).

For the coculture with dissociated bRPE, bRPE were dissociated as described during the procedure for passaging the bRPE (section 5.2.4). After centrifugation, the bRPE were suspended in RC1 medium (optionally with 5 µM Blebbistatin or 5 µl/mL Fibronectin, 47.5 µg/mL Laminin, and 16.6 µl/mL Vitronectin) and counted using a CASY® Cell counter and analyzer. One RO and approximately 100,000 bRPE cells (from the same iPSC line and usually the same differentiation) were added to one well of a Corning® Costar® Ultra-Low Attachment 96 Well Plate with round bottoms. ROs were harvested after 24 hours.

For the coculture with bRPE suspended in Matrigel-GFR, bRPE were dissociated as described in the coculture with dissociated bRPE, according to (114);. After centrifugation, approximately 500,000 bRPE were suspended in 10 µl Matrigel-GFR. The RO was transferred to sterile PARAFILM® M sealing foil molds, embedded in the bRPE-Matrigel-GFR mixture and incubated for 20 - 30 minutes at 37 ºC. Optionally, 10 µl Matrigel-GFR were added to the embedded ROs followed by an additional 10-minute incubation. ROs were harvested after 4 hours, 24 hours, 48 hours, 1 week, or 3 weeks.

5.5.1.Matrigel Embedding

For Matrigel embedding, ROs were embedded in 20 µl Matrigel-GFR as described in the bRPE-Matrigel-GFR coculture (section 5.5). Embedded ROs were harvested after 4 hours, 24 hours, 48 hours, or 1 week, and fixed in 0.1 % Glutaraldehyde, 2 % PFA for 30 minutes at RT. ROs were prepared for ICC as described in section 5.3.1. Fixed ROs were embedded as follows: the ROs were fixed for 20 minutes in 4 % PFA, embedded in Matrigel-GFR as described, and fixed for 10 minutes in 0.1 % Glutaraldehyde, 2 % PFA. Control ROs were not embedded in Matrigel-GFR. Sucrose infiltration, cryo-sectioning and immunostaining was conducted as described in sections 5.3.1-2. Imaging was conducted as described in section 5.3.3 with the following modification: at least three images of the ONL were taken at 20x magnification. Only cryosections from the center of an RO were imaged and analyzed. RCVRN-positive IS and positive staining with anti-Peripherin 2 (PRPH2) or anti-Retinal outer segment membrane protein 1 (ROM1), two OS markers, were manually counted using the cell counter plugin in Fiji (101). Statistical analysis was conducted as described in section 5.3.5.

5.6. Generation of *RP1* Knockout iPSC using CRISPR/Cas9

To generate *RP1* knockout iPSC lines using the CRISPR/Cas9 system, 7 potential guide RNAs (gRNAs) were predicted bioinformatically, while their efficiency was tested experimentally using a HEK293-based assay. The 4 gRNAs with the highest efficiency were transfected in iPSC line HD #1, and the CRISPR treated iPSCs were dissociated to single cells. Unless otherwise stated, all work was performed as part of this thesis.

5.6.1.Prediction and Evaluation of gRNA Efficiency

The bioinformatic prediction of gRNAs yielded 7 distinct gRNAs within the 2nd exon of *RP1*, which had a predicted on- and off-target score above 40 % ("Benchling CRISPR Design Tool" (115)). Evaluation of the efficiency of all 7 gRNAs was based on a fluorescence-based assay (116). This work was part of a bachelor thesis by Alexandra Tschiruchina (Institute for Human Genetics, University of Regensburg) with the following modifications. gRNAs were cloned into a pU6-(BbsI) CBh-Cas9-T2A-mCherry vector containing a Cas9 (*SpCas9*) expression cassette (Table 6). The ~500 bp target region of *RP1* was cloned into a pCAG-EGxxFP vector, thereby interrupting an enhanced green fluorescent protein (EGFP) fragment. 1.5 µg of each vector was co-transfected into HEK293 cells via calcium-phosphate transfection and incubated for total of 3 days. The fluorescence intensity was measured on a Spark® multimode microplate reader. The EGFP fluorescent signal was normalized to the mCherry fluorescence intensity (to account for fluctuations in transfection efficiency), and to the Hoechst fluorescence intensity (to account for fluctuations in the cell number and confluence). If the target sequence was cleaved by the gRNA guided *SpCas9*, the EGFP expression cassette reconstitutes resulting in a fluorescent signal. The intensity of the fluorescent signal was therefore used to gain insight into the efficiency of gRNAs. The 4 gRNAs with the highest green fluorescent signal were identified and used to treat the iPSCs.

5.6.2.CRISPR/Cas9 Treatment of iPSCs

Single guide RNA (sgRNA) was synthesized from each of the 4 gRNAs (Table 7) using the Precision gRNA synthesis kit according to the manufacturer's instructions with one modification: the final elution volume was increased to 12 µl of nuclease-free H_2O. The RNA concentration and purity were measured on a NanoDrop® spectrometer and the samples were transferred to -80 ºC. On the day of the CRIPSR/Cas9 treatment, ribonucleoprotein (RNP) complexes were generated with the reaction mixture shown in Table 33 by incubating for 10 minutes at RT.

Table 33: Reaction mixture for RNP complex generation. Volumes for one sgRNA sample are shown.

Component	Volume/Amount
prepared sgRNA	2.5 µg
TrueCut™ Cas9 Protein (diluted 1:5 with nuclease-free H_2O)	2 µl

Cas9 Buffer	0.8 µl
nuclease-free water	to 8 µl

Prior to transfection, one well per sgRNA of 80 % confluent iPSC from HD #1 clone 26 were treated with StemPro™ Accutase™ for 9 minutes, transferred to sterile 15 mL tubes and centrifuged at 300 rcf for 5 minutes. The supernatant was discarded, and the cell pellet was resuspended in 1 mL mTeSR_G medium. The cell number was determined in a Neubauer counting chamber with 20 µl of the cell suspension, 50 µl sterile Trypanblue Solution and 30 µl DPBS. 800,000 iPSCs per sgRNA were transfected with the prepared RNP complexes using the Human Stem Cell Nucleofector™ Kit 2 according to manufacturer's instructions. After the transfection, the iPSCs were transferred to Matrigel-coated 6 well plates and cultured in mTeSR_G with Y-27632 (10 µM). After two days, the iPSCs were passaged 1:2 as described previously (section 5.1.2). Once the iPSCs reached 70 % confluency they were cryo-preserved as described previously (section 5.1.3) and samples for genomic DNA (gDNA) extraction were harvested.

5.6.2.1. gDNA Extraction

For gDNA extraction, the cells were lysed in 500 µl Lairds Buffer with SDS and 50 µl Pronase E by incubating for several hours at 50 ºC and ON at 37 ºC. Samples were centrifuged at 16,000 rcf for 15 minutes, 450 µl isopropanol was added to the supernatant and mixed thoroughly. The samples were centrifuged as described in the previous step. The supernatant was removed, and the pellet was washed once with 70 % Ethanol and centrifuged as described. The DNA pellet was dried at RT and eluted in 15 µl H_2O (Millipore). The DNA concentration and purity were measured on a NanoDrop® spectrometer, and the samples were stored at -20 ºC.

5.6.2.2. Polymerase Chain Reaction (PCR) amplification of the target site

The sgRNA target site was amplified via PCR with the reaction mixture shown in Table 34 using oligonucleotide primers RP1_Ex2.1_F and RP1 Ex2.2_BamHI_R (Table 8). The thermocycler reaction is shown in Table 35. The elongation was performed for 50 seconds (s).

Table 34: Reaction mixture for PCR. Volumes for one sample are shown.

Component	Volume
H_2O (Millipore)	13.9 µl

45

5X GoTaq® Reaction Buffer	5 µl
dNTPs (10 mM)	2 µl
Forward primer (10 µM)	1 µl
Reverse primer (10 µM)	1 µl
GoTaq® Polymerase	0.1 µl
DNA template	2 µl

Table 35: Thermocycler program for PCR

Reaction step	Temperature	Duration	Cycles
Initial denaturation	94 °C	3 min	
Denaturation	94 °C	30 s	
Annealing	58 °C	30 s	32
Elongation	72 °C	60 s per 1000 bp	
Final elongation	72 °C	2 min	
Pause	10 °C	∞ min	

5.6.2.3.   Agarose Gel Electrophoresis

The PCR products were run on agarose gels to confirm the correct size of the PCR products and confirm their purity. To prepare the gels, 1.5 % (w/v) agarose was heated in TBE buffer until the agarose had completely dissolved, and then cooled in ice water to ~ 55 ºC before 1 – 3 drops 0.07 % ethidium bromide were added. 5 µl GeneRuler™ DNA Ladder mix was used as a size standard. The gels were run at 190 V for 25 – 35 minutes. PCR products were visualized on an UVP GelStudio PLUS.

5.6.2.4.   Purification of PCR Products

The PCR products were excised from the agarose gels and purified with the NucleoSpin® Gel and PCR Clean-up kit according to the manufacturer's instructions with one exception: 25 µl of H_2O (Millipore) were used for the final elution, instead of the elution buffer provided in the kit. The DNA concentration and purity were measured on a NanoDrop® spectrometer, and the samples were stored at -20 ºC.

5.6.2.5.   Ligation into pGEM®-T

The purified PCR products were ligated into the pGEM®-T vector using the reaction mixture shown in Table 36. The samples were ligated in a thermocycler at 14 ºC ON.

Table 36: Reaction mixture for ligation. Volumes for one sample are shown.

Component	Volume
T4 DNA Ligase Puffer (2x)	5 µl

46

PCR fragment	3.5 µl
T4 DNA Ligase	1 µl
pGEM®-T vector	0.5 µl

5.6.2.6.   Transformation of *E. coli*

After ligation, the samples were transformed in DH5α *E. coli* by heat shock treatment. The ligation reaction was added to the thawed cells on ice, gently mixed, and incubated at 42 ºC for 45 seconds. The samples were cooled briefly on ice, and then incubated with 600 µl SOC-medium at 37 ºC for 1.5 hours under constant shaking. LB plates with 100 µg/ml ampicillin were prepared for plating with 20 µl IPTG and 100 µl X-Gal for a blue/white screen. 200 µl of the cell suspension was evenly distributed and incubated ON at 37 ºC.

5.6.2.7.   Isolation of Plasmid DNA

White colonies were mechanically isolated and cultured ON in 5 mL LB-medium with 100 µg/ml ampicillin at 37 ºC under constant shaking. The samples were centrifuged at 2,900 rcf for 5 minutes and the supernatant was completely removed. The plasmid DNA was isolated from the cell pellets using the NucleoSpin® Plasmid kit according to the manufacturer's instructions with one exception: the final elution was executed in 40 µl H_2O (Millipore), instead of the elution buffer provided in the kit. The DNA concentration and purity were determined using a NanoDrop® ND1000 Spectrometer and the samples were diluted to 40 ng/µl with H_2O (Millipore).

5.6.2.8.   Sanger Sequencing of Plasmid DNA

Sanger sequencing was performed with plasmid DNA using the BigDye® Terminator Cycle Sequencing Kit v3.1. The reaction mixture is shown in Table 37 and the thermocycler program is shown in Table 38. Sequencing was conducted with the oligonucleotide primers RP1_Ex2.1_EcoR1_F (samples treated with SZ_RP1_KO_5), RP1_Ex2.1_F (samples treated with SZ_RP1_KO_7 or 8), or RP1_Ex2.1_R (samples treated with SZ_RP1_KO_10). Primer sequences are listed in Table 8.

Table 37: Reaction mixture for Sanger sequencing of plasmid DNA. Volumes for one sample are shown.

Component	Amount
H_2O (Millipore)	5.7 µl
5x Big Dye® Terminator Sequencing Buffer	2 µl
Primer (10 µM)	1 µl
Big Dye® Terminator	0.5 µl

Plasmid DNA (40 ng/µl)	1 µl

Table 38: **Thermocycler program for Sanger sequencing of plasmid DNA**

Reaction step	Temperature	Duration	Cycles
Initial denaturation	94 °C	3 min	
Denaturation	94 °C	30 s	
Annealing	58 °C	30 s	30
Elongation	60 °C	3 min	
Final elongation	60 °C	5 min	
Pause	15 °C	∞	

After the sequencing reaction was completed, the DNA was precipitated with 100 µl chilled 100 % ethanol. Samples were mixed thoroughly and centrifuged at 2,900 rcf for 45 minutes at 4 ºC. The DNA pellet was washed with 70 µl chilled 70 % ethanol and centrifuged at 2,900 rcf for 30 minutes at 4 ºC. The DNA pellet was solved in 20 µl Hi-Di™ Formamide and sequenced on an Abi3130x1 Genetic Analyzer. The sequences were analyzed in Chromas and SnapGene by searching for insertions or deletions (indels) at the target site in comparison to a reference sequence (NCBI reference sequence: NM_001375654.1). At least 20 sequences were analyzed per sgRNA. The efficiencies of each sgRNA were calculated by determining the percentage of sequences with indels at the target site. While the iPSC treated with the sgRNAs SZ_RP1_KO_8 and 10 did not show any indels (0 % efficiency), SZ_RP1_KO_5 and 7 had an acceptable efficiency rate of 20 % and 23.3 %, respectively.

5.6.3. Single Cell Dissociation of CRIPSR/Cas9 treated iPSCs

iPSCs treated with SZ_RP1_KO_5 and 7 were thawed as described in section 5.1.3 and dissociated to single cells using StemPro™ Accutase™, as described in section 5.6.2. iPSC single cells were diluted to a final concentration of 1 cell / 100 µl in mTeSR_G medium with 10 % CloneR™ (v/v). 100 µl of the cell suspension was plated per well on Matrigel-coated 96 well plates. Medium was changed daily. After two days, the iPSCs were switched to mTeSR_G medium. The iPSCs were inspected daily and wells with single iPSC cells were identified. Once the respective wells reached a confluency of 90 % (approximately 10-15 days), the iPSCs were passaged onto Matrigel-coated 24 well plates by incubating in 50 µl ReLeSR™ for 5 minutes at 37 ºC. Medium exchanges with mTeSR_G medium were conducted daily. Once the iPSCs

reached a confluency of ~90 % they were cryo-preserved, and samples were harvested for gDNA isolation as described in section 5.6.2.1. PCR was conducted as described in section 5.6.2.2. PCR products were run on agarose gels described in section 5.6.2.3, excised and purified as described in section 5.6.2.4, and prepared for Sanger sequencing as follows.

5.6.3.1.   PCR Cleanup and Sanger Sequencing

An enzymatic digestion was performed with the reaction mixture shown in Table 39. The digestion was executed in a thermocycler set to 37 ºC for 15 minutes, then to 80 ºC for 15 minutes and cooled to 15 ºC.

Table 39: Reaction mixture for oligonucleotide digestion. Volumes for one sample are shown.

Reagent	Volume
H_2O (Millipore)	3.65 µl
Exonuclease I	0.1 µl
Antarctic Alkalic Phosphatase	0.25 µl
PCR Product	1 µl

Sanger sequencing was applied to determine the genomic integrity of *RP1* at the sgRNA target site in the iPSC single clones. The reaction mixture is shown in Table 40 and the thermocycler program is shown in Table 41. Sequencing was conducted with the primer RP1_Ex2.1_EcoR1_F, listed in Table 8. Some samples were initially sequenced as part of a medical thesis (Sofiia Bondarenko, Institute of Human Genetis, University of Regensburg). Sequencing of these iPSC single clones was replicated in the course of this thesis.

Table 40: Reaction mixture for Sanger sequencing of PCR products. Volumes for one sample are shown.

Component	Amount
5x Big Dye® Terminator Sequencing Buffer	2 µl
H_2O (Millipore)	1.5 µl
Primer (10µM)	1 µl
Big Dye® Terminator	0.5 µl
PCR sample after enzymatic digestion	5 µl

Table 41: Thermocycler program for Sanger sequencing of PCR products.

Reaction step	Temperature	Duration	Cycles
Initial denaturation	94 °C	5 min	

Denaturation	94 °C	30 s	
Annealing	55 °C	30 s	27
Elongation	60 °C	3 min	
Final elongation	60 °C	5 min	
Pause	15 °C	∞	

After the sequencing reaction was complete, the DNA was precipitated as described in section 5.6.2.8 with one modification: the initial precipitation was conducted with 25 µl chilled 100 % ethanol and 2 µl sodium azide. Sequences were analyzed in SnapGene by aligning to a reference (NCBI reference sequence: NM_001375654.1), and examining the sgRNA target site for indels. Two iPSC single clones treated with SZ_RP1_KO_7 had homozygous frameshift mutations (RP1_KO #1 and 2, Table 2). None of the iPSC single clones treated with SZ_RP1_KO_5 had homozygous or compound heterozygous frameshift mutations.

5.6.4. Differentiation, Harvest, and Analysis of *RP1* Knockout ROs

RP1_KO #1 was differentiated, harvested, and analyzed together with RP1_WT #1. RP1_KO #2 was handled in parallel to RP1_WT #2. iPSCs were thawed and passaged according to section 5.1.2-3, ROs were differentiated according to section 5.2.3. The age of the ROs was determined as described above (section 5.3.1). ROs were harvested on day 180 (± 1 day). Some immunostainings and imaging were performed in a medical thesis (Anne-Sophie Pieger, Institute of Human Genetics, University of Regensburg). Immunostainings shown in this thesis were prepared independently.

6. Results

6.1. Differentiation Protocols Influence RO Cellular Composition[5]

Multiple RO differentiation protocols have been established so far, but there is little consensus as to which protocol produces the highest quantity and best quality of ROs. In this study, we differentiated the same iPSC line using three published RO differentiation protocols termed M1 (based on ref. (45)), M2 (based on ref. (59)), and M3 (based on ref. (47)), and compared their efficiency and cellular composition. M1 is a 3D differentiation technique that utilizes several extrinsic factors to induce differentiation (Figure 11A). The signaling factors used in M1 modulate three pathways involved in retinogenesis namely the hedgehog, Wnt, and Notch pathway (17). M2 and M3 are 3D-2D-3D differentiation techniques that follow the same basic differentiation procedure (Figure 11A). M2 exploits intrinsic cues to guide differentiation, instead of strong extrinsic factors. M3 uses one main extrinsic factor, BMP4, which is an activator of the BMP signaling pathway (Figure 11A).

First, we investigated whether each differentiation method could successfully generate ROs. In our hands, each differentiation method successfully produced ROs showing a phase bright outer rim, which corresponds to the developing neuroepithelium (Figure 11B; (45,47,59)). This neuroepithelial layer is regarded as a characteristic morphological feature of viable ROs. To further confirm proper retinal differentiation, the expression of the ganglion cell marker SNCG (117,118), and two early photoreceptor markers RCVRN (119) and CRX (120,121), were confirmed in ROs from each differentiation method (Figure 11B). These results indicate that each method successfully produced ROs, so further analyses were performed to determine their quantity and quality.

---

[5]This section was adapted from Berber et al. (161).
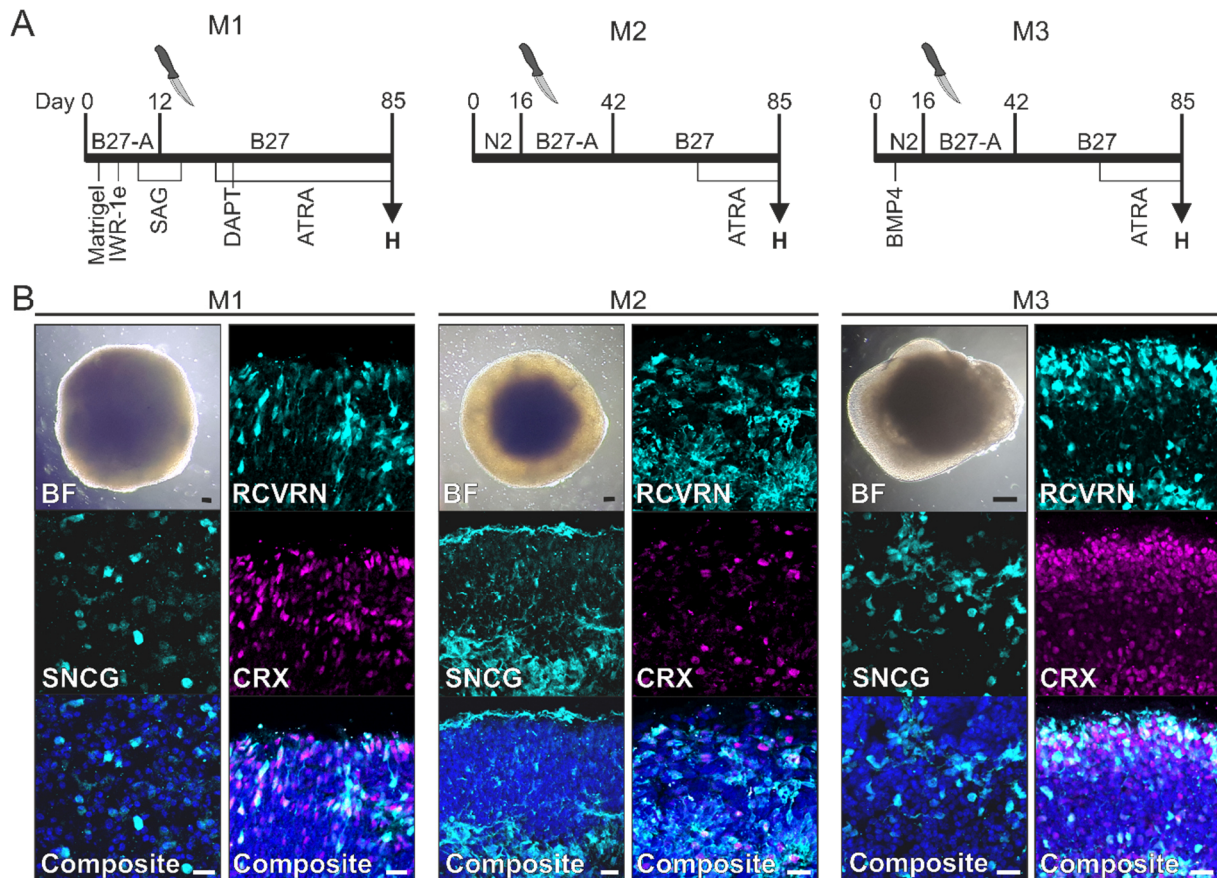
Figure 11[6]: Overview of RO differentiation protocols. (**A**) A timeline of each RO differentiation protocol is shown. The supplements and extrinsic factors used in each protocol are denoted above and below the timeline, respectively. The timepoint of excision is indicated with a knife. "H" indicates the timepoint when the ROs were harvested for the comparative analyses (day 85). (**B**) Each differentiation method successfully produced ROs (shown on day 85). ROs from each method contained ganglion cells (SNCG-positive) and photoreceptor cells (RCVRN-positive, CRX- positive). Composite images were counterstained with Dapi. Black scale bar: 100 µm; white scale bar: 50 µm.

To determine the method with the highest quantity, we counted the retinal domains (RO precursors), produced using M1 on day 10 and using M2 and M3 on day 23 (Figure 12A, B). These timepoints were chosen based on recommendations given in the respective protocols, concerning the optimal timepoint for retinal domain excision (45,59). M3 produced strikingly more retinal domains per differentiation (65 ± 27) than M1 (12.3 ± 11.2) and M2 (6.3 ± 6.7; p = 0.01), despite some variability. Furthermore, the retinal domains from M3 were more clearly defined, and therefore easier to excise (Figure 12A). The retinal domains which matured to ROs were counted on day 63. Again, M3 yielded more viable ROs than M2 (24.7 ± 17.2 vs. 1.7 ± 0.6; p = 0.05).

---

[6] This figure is modified after Berber et al. (161).
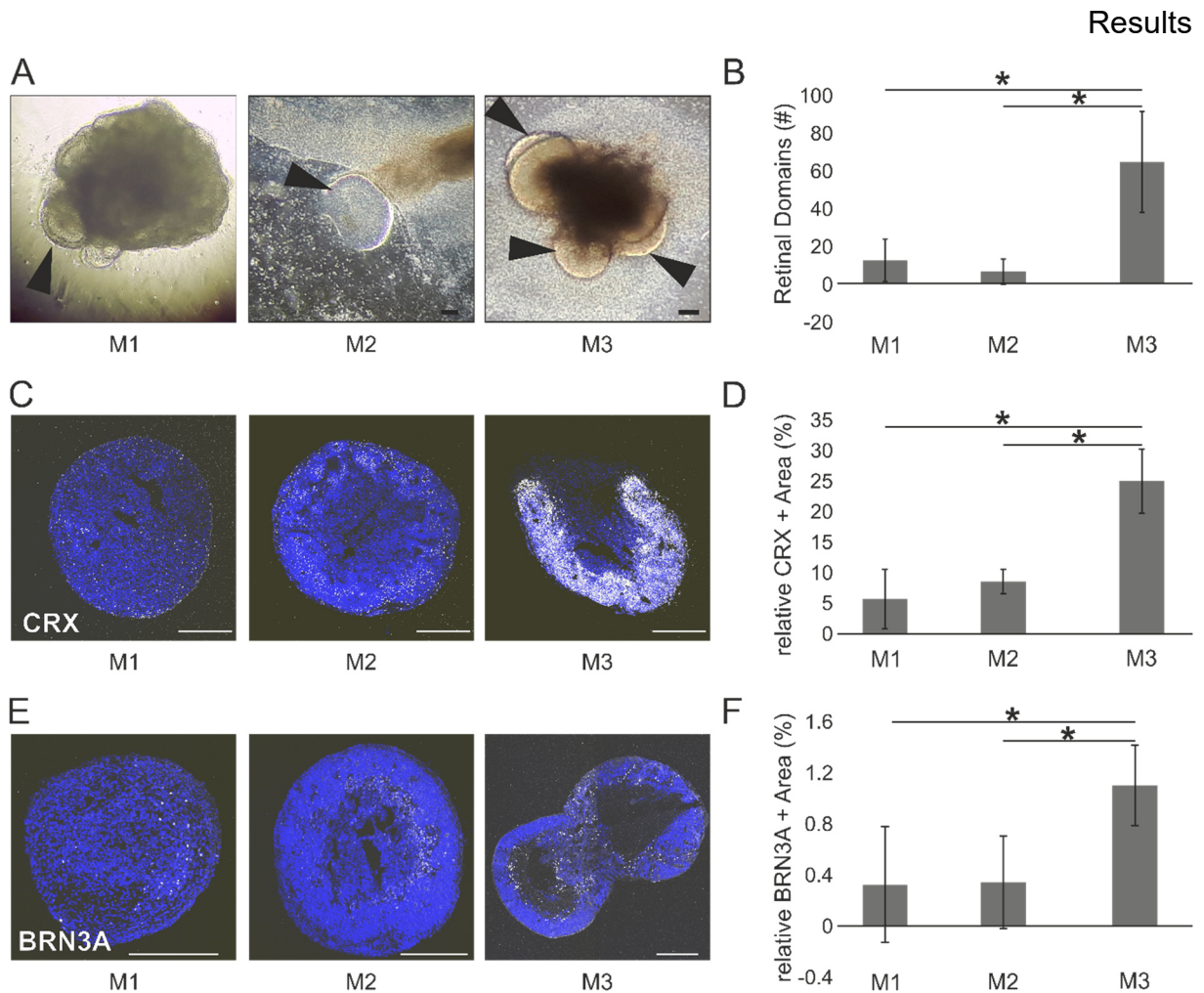
Figure 12[7]: M3 produced a larger quantity and higher quality of ROs. (**A**) Brightfield images show proper differentiation of retinal domains pre-excision (arrowheads indicate retinal domains). (**B**) More ROs per differentiation were acquired using M3 compared to M2. (**C**) Whole cryosections of 85-day-old ROs from each differentiation method, stained with a photoreceptor marker (CRX) are shown. (**D**) The relative CRX-positive area was greatest in the ROs differentiated using M3. (**E**) Whole cryosections of 85-day-old ROs stained with a ganglion cell marker (BRN3A) are shown. (**F**) The relative BRN3A-positive area was greatest in the ROs differentiated using M3. Images were counterstained with Dapi. Scale bars: (A) 100 μm; (C, E) 300 μm. (B, D, F) *p < 0.017 (Bonferroni-corrected); error bars indicate the standard deviation from the mean.

To determine the method with the highest RO quality, we quantified the expression of several retinal markers in 85-day-old ROs. This timepoint was chosen, because the cellular composition of ROs on or near day 85 has been well documented by previous groups (47,59,122). First, we investigated the expression of CRX, a transcription factor which is one of the earliest genes expressed in photoreceptor precursors, as well as mature photoreceptors (120,121,123). RO cryosections were immunostained for CRX (Figure 12C), and the CRX-positive area was quantified relative to the Dapi-positive area (blue staining). This quantification technique allows

---

[7] This figure is modified after Berber et al. (161).

the quick and reliable quantification of whole RO cryosections, thereby accounting for regional variability. We found the highest CRX expression in the M3 ROs (25 ± 5.3 %), whereas the M1 (5.7 ± 4.8 %) and M2 ROs (8.6 ± 2 %) demonstrated a significantly lower expression profile and were comparable to each other (p = 0.003; Figure 12D). Next, we evaluated the expression of BRN3A, a transcription factor and an early ganglion cell marker (124–126) (Figure 12E). Again, the M3 ROs showed the highest BRN3A expression compared to M1 and M2 (M1: 0.3 ± 0.5 %; M2: 0.3 ± 0.4 %; M3: 1.8 ± 0.3 %; p = 0.006; Figure 12F). In contrast, the different methods did not have a significant effect on the expression of the amacrine cell marker TFAP2A, the ganglion cell marker SNCG, or the photoreceptor marker RCVRN (Supp. Figure 2).

6.2. ROs Contain all Main Retinal Cell Types

The final investigation evaluated whether M3 ROs provide a suitable retinal model system for downstream experiments, by characterizing their individual cellular diversity. Therefore, the presence of the eight main retinal cell types was examined including the RPE, cone and rod photoreceptors, amacrine cells, bipolar cells, Mueller cells, horizontal cells, and ganglion cells (Figure 13A). The presence of RPE cells could be easily detected based on their unique pigmentation in whole ROs (Figure 13B inlay) and RO cryosections (Figure 13B). The remaining seven retinal cell types were detected by immunostaining. M3 ROs contained OPN1SW-positive cone photoreceptors (Figure 13C), RHO-positive rod photoreceptors (Figure 13D), TFAP2A-positive amacrine cells (Figure 13E), Protein kinase C alpha-positive (PRKCA) bipolar cells (Figure 13F), Calbindin 1-positive (CALB1) horizontal cells (Figure 13G), Retinaldehyde binding protein 1-positive (RLBP1) Mueller cells (Figure 13H), BRN3A-positive ganglion cells (Figure 13I). Hereafter, all downstream experiments were performed with ROs differentiated following M3.
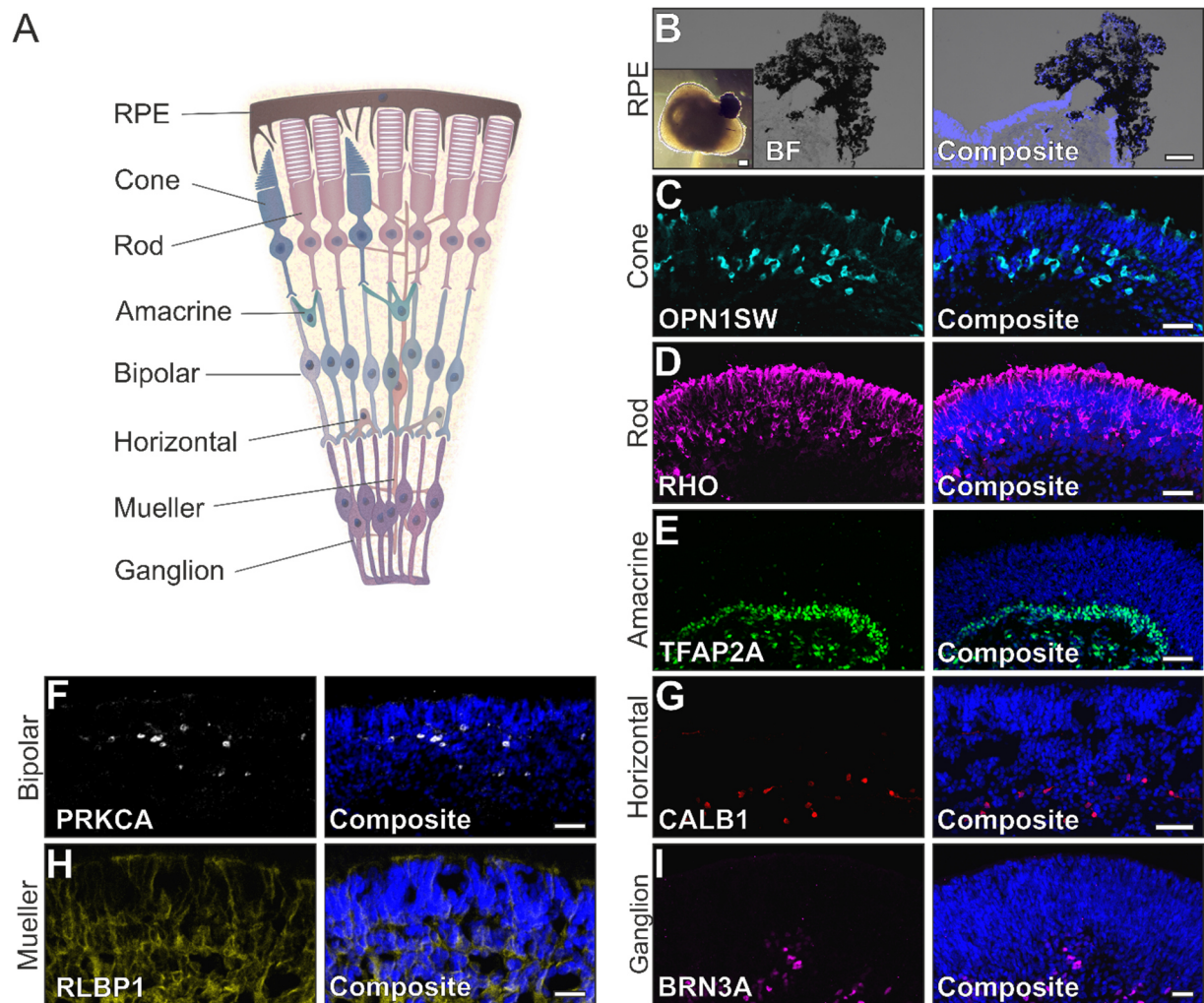
Figure 13: ROs contain all main retinal cell types. (**A**) Schematic representation of the main retinal cell types and their histoarchitecture is shown. (**B-H**) ROs differentiated according to M3 contain all main retinal cell types: (**B**) brightfield image of pigmented RPE cells in a 5-month-old RO, (**C**) OPN1SW-positive cone photoreceptors in a 7-month-old RO, (**D**) RHO-positive rod photoreceptors in a 5-month-old RO, (**E**) TFAP2A-positive amacrine cells in a 4-month-old RO, (**F**) PRKCA-positive bipolar cells in a 6-month-old RO, (**G**) CALB1-positive horizontal cells in a 6-month-old, (**H**) RLBP1-positive Mueller cells in a 6-month-old, and (**I**) BRN3A-positive ganglion cells in a 3-month-old RO. Composite images are counterstained with Dapi. Scale bars: 50 µm except in (B) inlay 200 µm. PR: photoreceptor.

6.3. RO Cellular Composition Variability

ROs were differentiated from two healthy donors with no history of inherited retinal dystrophy (HD #1 and 2). These ROs showed a donor-dependent effect on cellular composition. ROs from HD #1 and 2 were immunostained for several retinal markers (amacrine cells: TFAP2A, ganglion cells: SNCG, and photoreceptors: CRX, RCVRN, and RHO) and one proliferation marker (KI67). HD #1 ROs had a higher relative TFAP2A-positive area than HD #2 ROs (7.9 ± 1.9 % vs. 3.3 ± 2%; p = 0.004; Figure 14A, B), whereas HD #2 ROs had a higher relative SNCG-positive area than

HD #1 (1.5 ± 0.004 % vs. 0.2 ± 0.2 %; p = 0.004; Figure 14C, D). These results indicate that HD #1 ROs contain more amacrine cells, while HD #2 ROs contain more ganglion cells. In contrast, the relative CRX-, RHO-, or KI67-positive area was not significantly altered among HD #1 and #2 ROs.
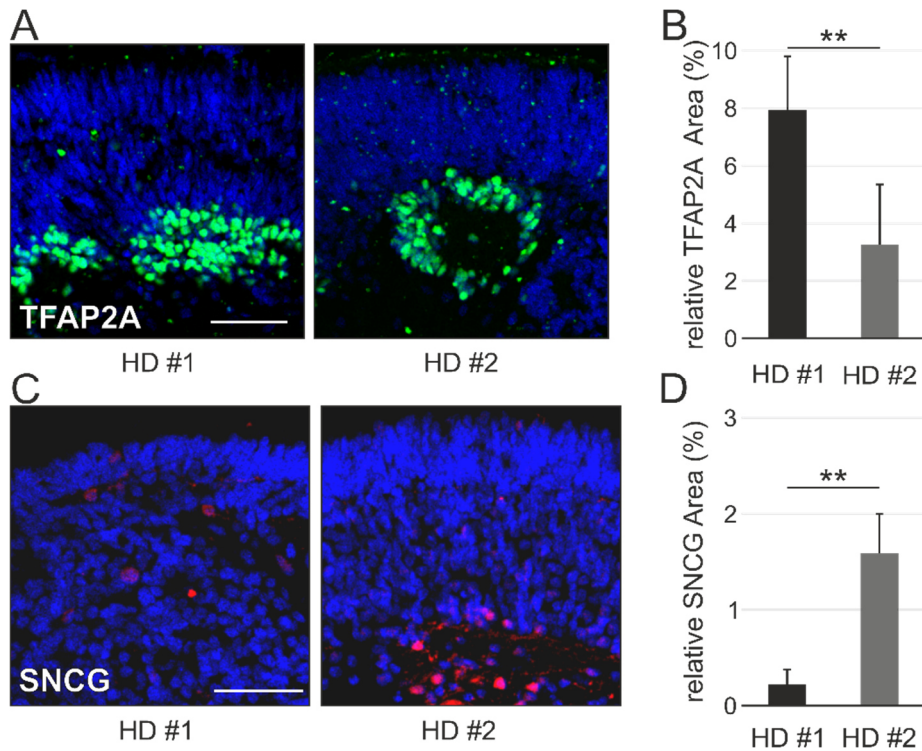
Figure 14: ROs show donor-dependent effects on cellular composition. (**A**) TFAP2A-positive amacrine cells are shown in 4-month-old HD #1 and HD #2 ROs. (**B**) The relative TFAP2A-positive to Dapi-positive area is shown. HD #1 ROs have a higher relative TFAP2A-positive area than HD #2. (**C**) SNCG-positive ganglion cells are shown in 5-month-old HD #1 and HD #2 ROs. (**D**) The relative SNCG-positive to Dapi-positive area is shown. HD #1 ROs have a lower relative SNCG-positive area than HD #2. Scale bars: 50 µm; ** p < 0.01 (Bonferroni-corrected); error bars indicate the standard deviation from the mean

RNA-seq was performed to investigate the mRNA expression profiles of HD #1, HD #2 and adRP1 #1 ROs at four total timepoints (6, 12, 18, and 24 months; sample overview shown in Figure 10). A principal component analysis (PCA) of the expressed CPM values of each RO, revealed that PC1 (explaining 24.37 % of variance) reflects RO maturation (light blue to black gradient; Figure 15A). PC2 (explaining 11.41 % of variance) most likely reflects an inter-organoid variability (Figure 15A). ROs from the same donor (and even from the same differentiation) sometimes do not cluster together. Of note, the inter-organoid variability was most prominent in the younger ROs (6 and 12-month-old ROs, light-blue and sky-blue samples), and the expression profiles appeared to harmonize over time (18 and 24-month-old ROs, cobalt-blue and black samples). PC3 (explaining 7 % of variance) likely portrays a donor-dependent

effect on expression (Figure 15B). In PC3, the HD #1 ROs (squares), HD #2 ROs (triangles), and adRP1 #1 ROs (circles) clustered together.
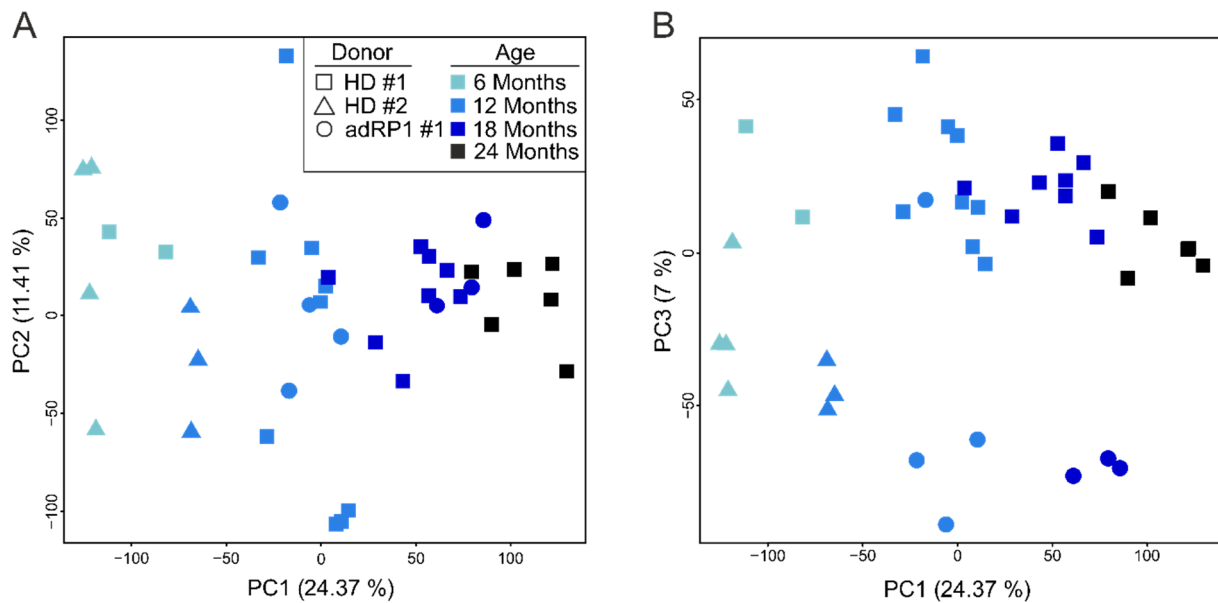
Figure 15: PCA of RNA-seq data from ROs. (**A**) A PCA of PC1 vs. PC2 is shown. PC1 reflects RO maturation (light blue to black gradient, from left to right) while PC2 shows the inter-organoid variability. (**B**) A PCA of PC1 vs. PC3 is shown. PC3 reflects a donor-dependent effect on expression (HD #1 ROs are represented by squares; HD # 2 ROs are represented by triangles; adRP1 #1 ROs are represented by circles). A sample legend is shown in (A) inlay.

To further characterize the donor-dependent effect on expression, the DEGs from each donor (compared to the other two donors) were determined. The top five up and downregulated DEGs are shown as a heatmap in the 12-month-old ROs (Figure 16). There were a total of 1,350 DEGs in HD #1 ROs (567 upregulated and 783 downregulated) and 1,329 DEGs in HD #2 ROs (619 upregulated and 710 downregulated; Supp. Figure 3). In contrast, adRP1 #1 ROs had a milder donor effect (769 DEGs: 398 upregulated and 371 downregulated). As seen in the PCA, the maturation effect of the ROs appears to be stronger than the donor effect. For example, in the comparison between the 6 and 24-month-old ROs, there were 6,171 DEGs (3326 upregulated and 2845 downregulated).
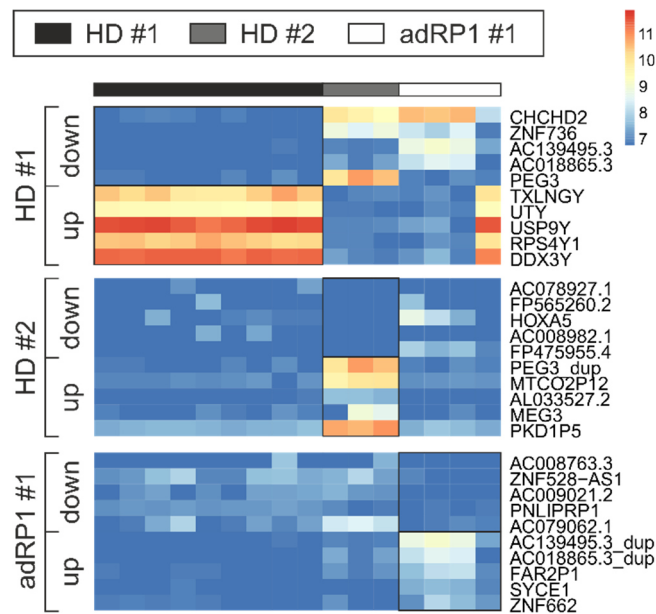
Figure 16: Heatmaps of donor-dependent up- and downregulated DEGs. The top five upregulated and top five downregulated DEGs from each donor (in comparison to the other two donors) are shown in a heatmap of 12-month-old ROs. The black, grey, and white bar directly above the heatmap denotes the origin of the samples shown in the heatmap.

The variability of ROs was not limited to the donor-dependent effect and inter-organoid variability. In fact, regional differences were also observed within the same RO. This effect was most apparent in the subtype specification of photoreceptor precursors to rod photoreceptors. A whole RO cryosection was immunostained with RCVRN (expressed by precursors, rod, and cone photoreceptors), and RHO (specifically expressed by rod photoreceptors; Figure 17A). While RCVRN-positive photoreceptors were evenly distributed around the entire RO perimeter (corresponding to the ONL), the distribution of RHO-positive rod photoreceptors was not homogenous. There were low-density regions with few or no rod photoreceptors (Figure 17B1), which were sharply delineated (Figure 17B2), from high-density regions with many rod photoreceptors (Figure 17B3). The uneven rod photoreceptor distribution suggests that RO photoreceptor subtype specification does not occur in the entire ONL simultaneously. Instead, it appears that rod-dense clusters arise, and then expand over time.
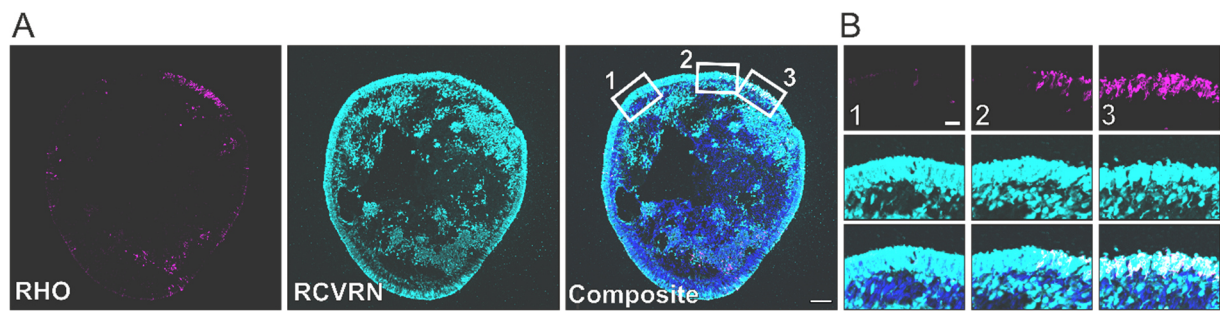
Figure 17: Intra-organoid variability. (**A**) A whole cryosection of a 5-month-old RO is shown. The entire perimeter of the RO shows RCVRN-positive photoreceptors, whereas the development of RHO-positive rod photoreceptors is region-dependent. White boxes (labelled 1, 2, and 3) denote the position of three magnified images. (**B**) Three magnified images are shown. Image 1 shows a region with very few RHO-positive rod photoreceptors, whereas image 3 shows a region with many RHO-positive rod photoreceptors. Image 2 shows the transition zone. All three zones show a high-density of RCVRN-positive photoreceptors. Composite images are counterstained with Dapi. Scale bars: (A) 100 μm (B) 50 μm

To summarize, it was observed that the cellular composition and expression profiles of ROs is variable. In-depth analyses allowed for the characterization of a donor effect, inter-organoid variability, and intra-organoid variability. All downstream experiments were designed to control for RO variability. To control for intra-organoid variability, all ICC quantifications were conducted with whole cryosections, and at least three cryosections were included per RO. Whenever possible, multiple donors were analyzed. Many investigations were also performed with long-term RO cultures, since the inter-organoid variability decreased over time (Figure 15A).

6.4. Mobile RO Culture on an Orbital Shaker

Previous reports indicated that culturing ROs in bioreactors, which facilitate the distribution of fresh media, improve the photoreceptor yield (91), and accelerate differentiation (92). Based on these data, we cultured ROs on an orbital shaker to emulate the same effect of distributing fresh media. The RO morphology, cellular composition, and expression profiles were evaluated (Figure 18).
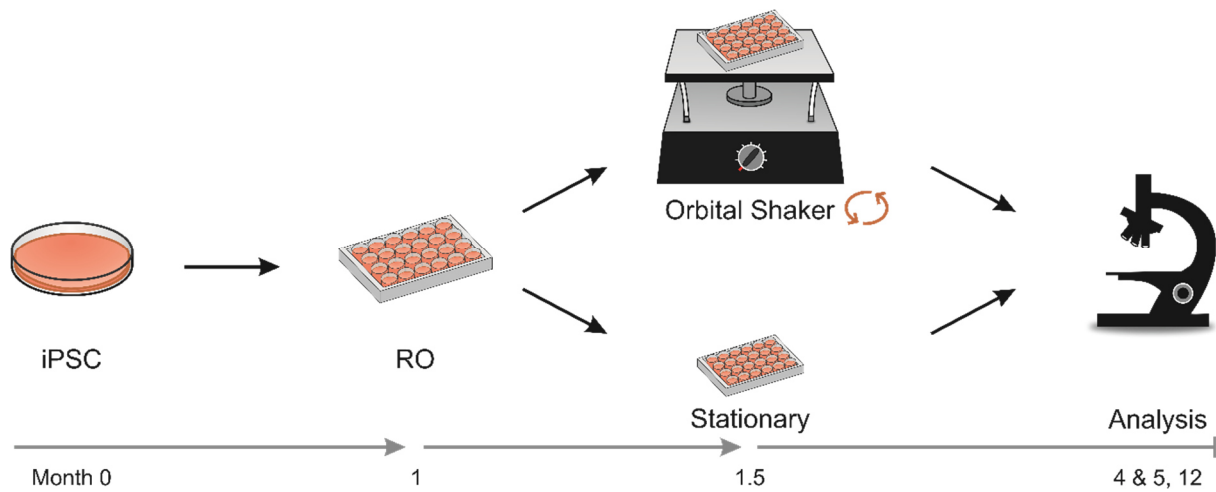
Figure 18: Schematic representation of the experimental design used to investigate ROs cultured on an orbital shaker. iPSCs were differentiated to ROs. After 1 month, the developing ROs were excised and cultured in 24 well plates. After 1.5 months (precisely 43 days), ROs were transferred to an orbital shaker or kept in stationary culture. After 4 or 5 months in culture, the morphological development of ROs was evaluated via brightfield microscopy, and the cellular composition was determined via ICC. After 12 months in culture, the expression profiles were investigated via RNA-seq.

First, the orbital shaker ROs (orbRO) and stationary ROs (statRO) from HD #1 and 2 were evaluated via brightfield microscopy, which revealed a comparable morphological development (Figure 19A). Next, the general histoarchitecture of the ROs was examined via immunostaining for RHO, since the expression of this marker should be limited to the ONL. While most RHO-positive rod photoreceptors were correctly localized to the ONL (Figure 19B, circumscribed with a dashed line), both orbROs and statROs contained some mislocalized RHO-positive rod photoreceptors, which were located towards the RO core (Figure 19B, indicated with arrows).
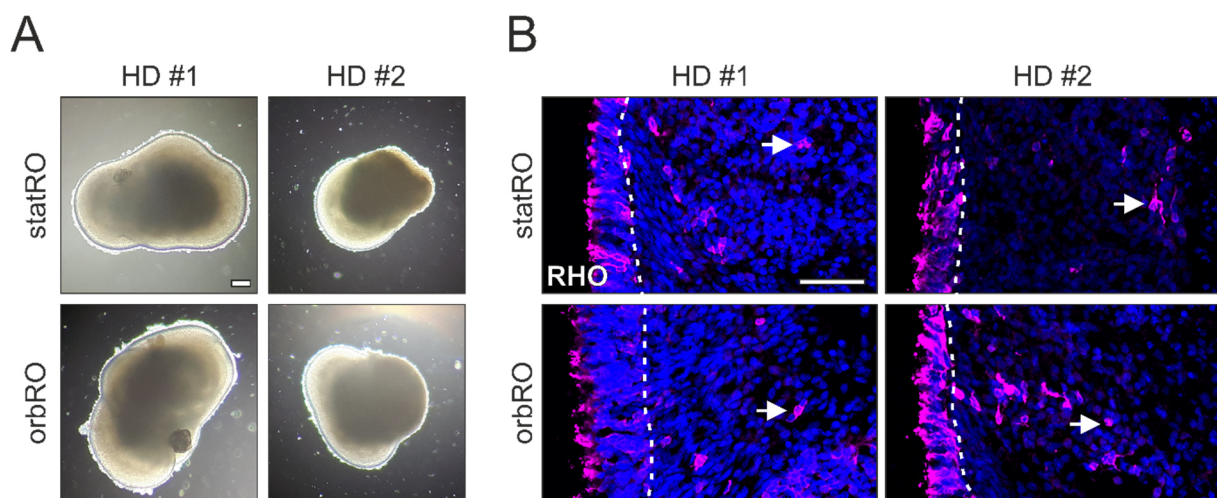
Figure 19: statROs and obROs show comparable morphological development and histoarchitecture. (**A**) Brightfield images of 5-month-old ROs from HD #1 and 2 show the morphological development of ROs was not overtly impacted by the culture on an orbital

shaker. (**B**) The immunostaining of RHO in statROs and orbROs is shown. Most RHO-positive rod photoreceptors were correctly localized within the ONL (circumscribed with a white dashed line), but some mislocalized rod photoreceptors were located outside the ONL (indicated with arrows). Images are counterstained with Dapi. Scale bars: (A) 200µm (B) 50µm

To further characterize the cellular composition of HD #1 and #2 orbROs and statROs, immunostaining for several retinal markers was performed: RHO, RCVRN (Figure 20A, B), CRX (Figure 20C, D), and SNCG (Figure 20E, F). Despite some replicates which suggested an increase of the relative RHO-positive to RCVRN-positive area in 5-month-old ROs (Figure 20A), no significant differences in the cellular composition of orbROs and statROs were noted.
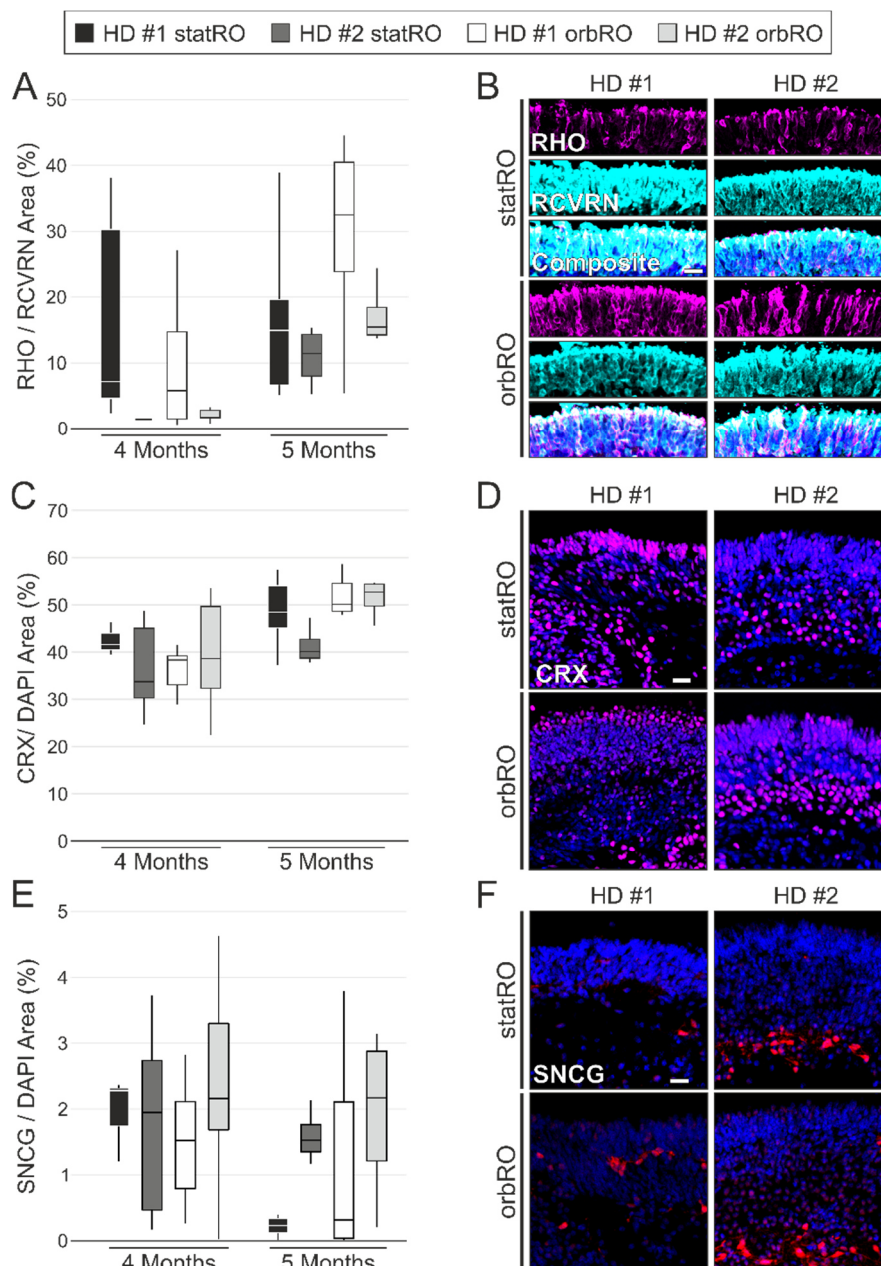
Figure 20: statROs and orbROs show comparable cellular composition. (**A**) The ratio of RHO- to RCVRN-positive area in 4 and 5-month-old statROs and orbROs is shown. Despite

some replicates which indicated an increase of RHO-positive rod photoreceptors (HD #1, 5 months) in orbROs, effects were not significant after Bonferroni correction for multiple testing. (**B**) RCVRN-positive photoreceptors and RHO-positive rod photoreceptors are shown in 5-month-old statROs and orbROs from HD #1 and 2. (**C**) The relative CRX-positive area in 4 and 5-month-old statROs and orbROs is shown. (**D**) CRX-positive photoreceptors are shown in 5-month-old statROs and orbROs from HD #1 and 2. (**E**) The relative SNCG-positive area in 4 and 5-month-old statROs and orbROs is shown. (**D**) SNCG-positive ganglion cells are shown in 5-month-old statROs and orbROs from HD #1 and 2. Scale bars: 20 μm

Finally, the expression profiles of statROs and orbROs were analyzed in 12-month-old ROs. When the expression profiles were compared, there were only 45 DEGs (7 upregulated and 38 downregulated), indicating that the expression profiles of statROs and orbROs were very similar (Supp. Figure 3). In conclusion, no significant effects of the orbital shaker on the morphological development, cellular composition, or expression profile were observed.

6.5. Photoreceptor OS and mechanical stress in RO analysis

One aspect of ROs which make them a highly sophisticated *in vitro* retinal model, is that they contain photoreceptors with developed IS and OS. This is particularly important for the study of rod- or cone-related disease such as RP1, as the disease-associated protein is localized to the photoreceptor axoneme (86). The IS and OS of RO photoreceptors protrude from the RO surface, making them vulnerable to mechanical stress. Repeatedly, ROs with strong IS and OS outgrowth lost much of this outgrowth during processing (a particularly dramatic example is shown in Figure 21A, B).
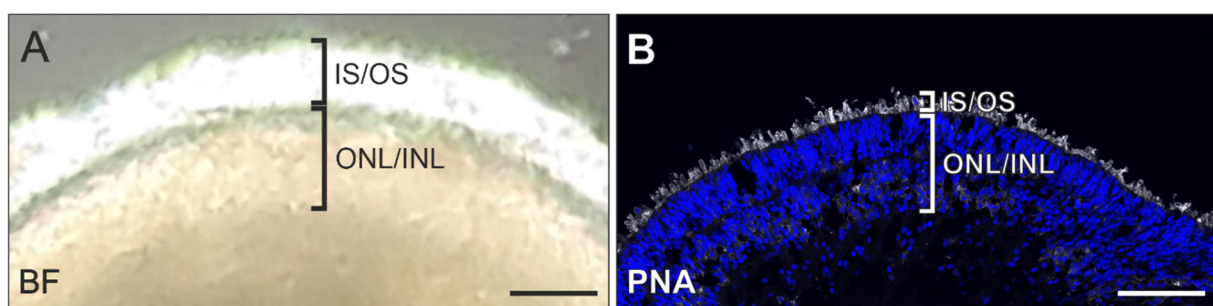
Figure 21: Photoreceptor IS and OS are lost during processing. (**A**) A brightfield image and (**B**) PNA-positive photoreceptor IS and OS of the same RO are shown. Prior to processing, the RO showed considerable IS and OS outgrowth, but after processing for ICC, the outgrowth was considerably reduced. THE ONL/INL width was not affected by the processing. Counterstained with Dapi. Scale bars: 200 μm

In vivo, photoreceptor OS are enveloped by the RPE, but this is not the case in ROs. To address this incongruency, we explored coculturing ROs and RPE cells, with

the aim of stabilizing the RO photoreceptor OS. We theorized, that the likelihood of an efficacious interaction between the RPE and RO photoreceptors would be more likely if the RPE and ROs were differentiated from the same starting point. To this end, a technique was developed to simultaneously differentiate ROs and RPE (Figure 22). The initial steps of M3 were followed as usual, but after RO excision, the remaining cells were treated with nicotinamide, and pigmented RPE clusters were isolated (termed byproduct RPE, bRPE). The bRPE were evaluated to determine whether they exhibit typical mRNA and protein expression of RPE markers, and multiple coculture techniques with ROs were performed.
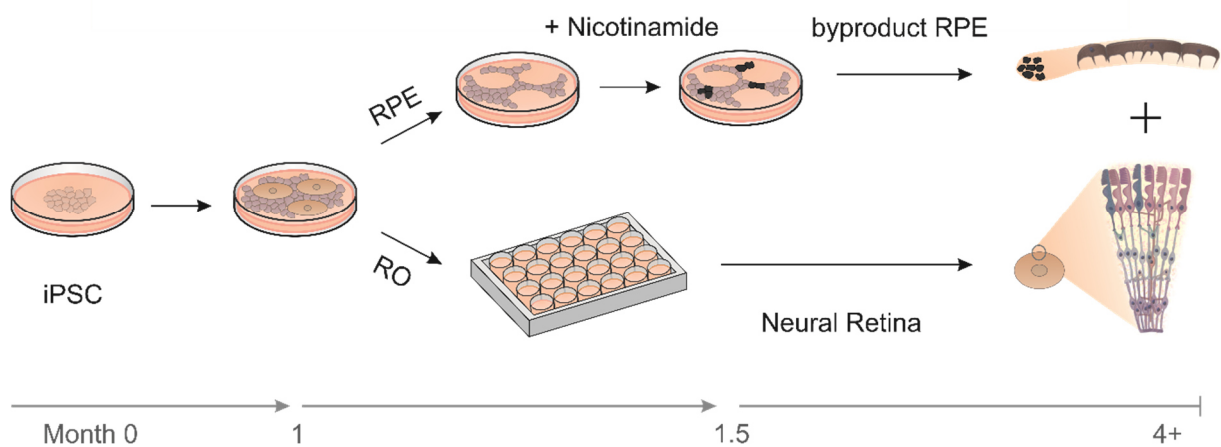
Figure 22: Schematic representation of the experimental design used for dual-differentiation and coculture of bRPE with ROs. iPSCs were differentiated to ROs and bRPE. After 1 month, ROs were excised and transferred to 24 well plates. The remaining cells were treated with nicotinamide, and after 1.5 months pigmented cell clusters (representing bRPE) were excised. Different coculture techniques were conducted to reunite the bRPE and ROs.

The expression of four RPE markers was tested via qRT-PCR, namely, Melanocyte Inducing Transcription Factor (MITF), Premelanosome Protein (PMEL), Bestrophin 1 (BEST1), and Retinoid Isomerohydrolase RPE65 (RPE65) (Figure 23A). All four markers were significantly upregulated in the bRPE in comparison to undifferentiated iPSCs. The bRPE also exhibited the RPE-typical cobblestone morphology (Figure 23B). To determine whether bRPE can acquire an apical-basal polarity, they were cultured on transwell filter inserts for 6 weeks and immunostained for BEST1 (an RPE marker localized at the basolateral aspect of the RPE (94,127)) and ZO-1 (which is part of the zona occludens at the apical aspect of the RPE (128,129); Figure 23C). BEST1 and ZO-1 immunostaining revealed the RPE-typical honeycomb pattern. Finally, the ability of bRPE to phagocytose RO photoreceptor OS was evaluated. Therefore, bRPE cells on a transwell filter insert were cultured with a

single RO for two weeks. The RO spontaneously detached from the bRPE lawn, and the bRPE were immunostained with ZO-1 and RHO (Figure 23D). Intracellular RHO-positive photoreceptor OS were observed (Figure 23D, arrowhead), indicating that the bRPE could execute this critical function.
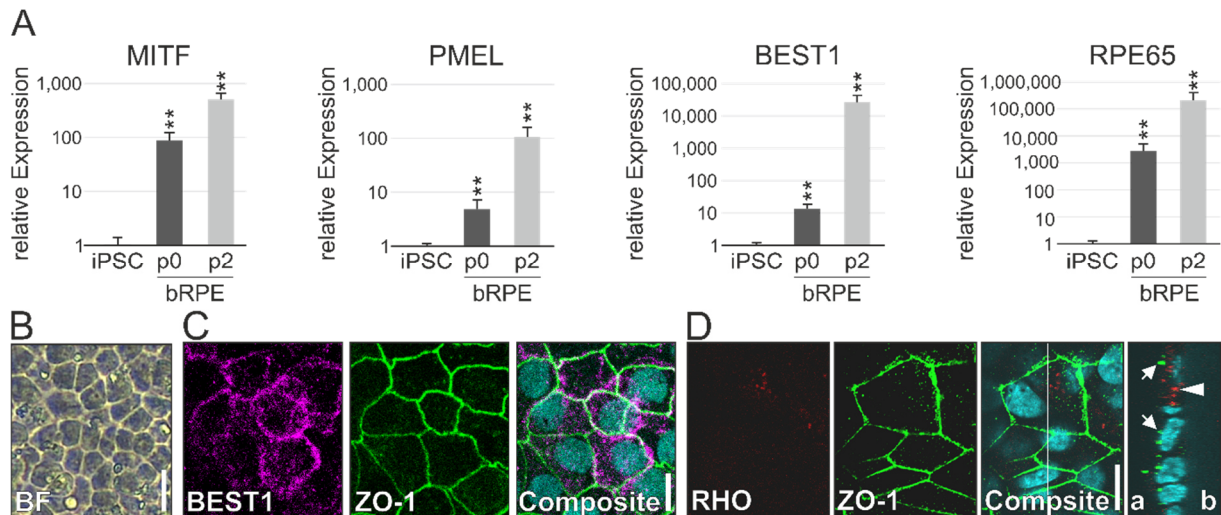
Figure 23: bRPE express characteristic RPE markers and phagocytose photoreceptor OS. (**A**) The relative expression of RPE markers MITF, PMEL, BEST1, and RPE65 in bRPE cells during differentiation (p0) and after 2 passages (p2), in comparison to undifferentiated iPSC is shown. (**B**) A brightfield image of bRPEs exhibiting cobblestone morphology is shown. (**C**) bRPE cells show expression of BEST1 (an RPE marker) and ZO-1 (a tight junction marker), forming a honeycomb pattern. (**D**) After coculture with a RO, bRPE show uptake of RHO-positive photoreceptor OS. Z-stack demonstrates the intracellular localization of RHO-positive OS (arrowhead: RHO-positive photoreceptor OS; arrow: ZO-1-positive tight junctions; a: apical; b: basal). Composite images are counterstained with Dapi. Scale bars: 10 μm, ** $p < 0.01$ (Bonferroni-corrected)

Several bRPE-RO coculture techniques were compared. First, a coculture was induced by plating ROs on bRPE cultured on a transwell insert. The ROs frequently detached from the bRPE lawn despite very careful handling (Figure 24A). Hydrogel or Matrigel were added to stabilize the RO attachment (112), but the gels created a gap between the RO and bRPE, thereby obstructing a proper interaction between the bRPE and RO photoreceptors (Figure 24B). Next, cocultures were induced by adding dissociated bRPE to ROs in low-attachment chambers (Figure 24C, D). Again, most of the bRPE spontaneously detached from the RO surface. Investigations at a high magnification revealed a gap between the remaining bRPE and RO photoreceptors (Figure 24E). A variety of substances were added to the coculture with dissociated bRPE, to improve bRPE attachment. Those substances proved to be either toxic to the RO (Blebbistatin) or failed to improve the bRPE attachment (adhesive glycoproteins found in the photoreceptor extracellular matrix: Fibronectin, Vitronectin, and Laminin).

A final coculture technique was performed by suspending dissociated bRPE in Matrigel and coating the RO (114) (Figure 23F, G). While the bRPE formed clusters within the Matrigel (indicating that the bRPE cells were viable and could migrate within the Matrigel), an interaction between the bRPE and RO photoreceptors was not observed (Figure 23H).
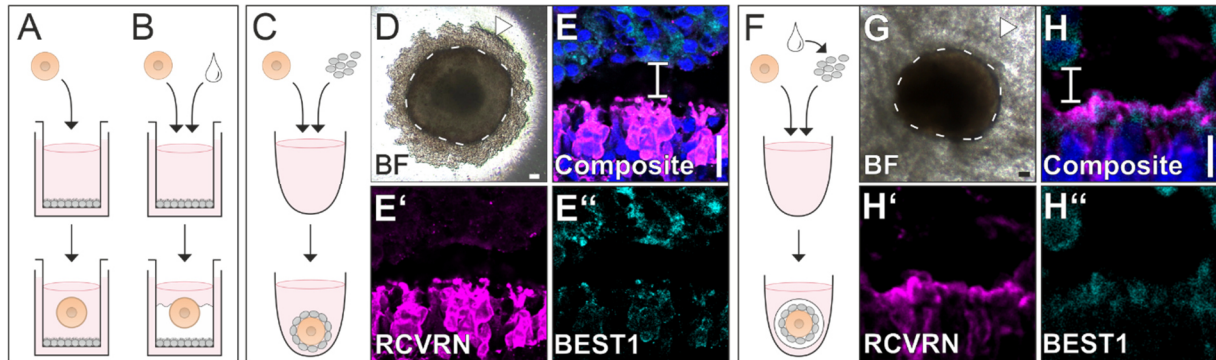
Figure 24: bRPE-RO coculture techniques. (**A**) Coculture was induced by plating ROs on bRPE cultured on a transwell filter insert, but the ROs did not adhere to the bRPE lawn. (**B**) Coculture on transwell filter inserts was stabilized by adding hydrogel or Matrigel (white droplet), which resulted in a gap between the RO and bRPE lawn. (**C**) Coculture was induced by culturing the RO with dissociated bRPE in a round-bottomed chamber. (**D**) Brightfield image of RO (denoted with a white dashed line) and dissociated bRPE (denoted with an arrowhead). (**E, E', E''**) BEST1-positive bRPE did not attach to the RCVRN-positive photoreceptors in the RO (gap indicated by a bracket in the composite image). (**F**) Coculture was induced by culturing the RO with bRPE suspended in Matrigel (white droplet). (**G**) Brightfield image of RO (denoted with a white dashed line) and bRPE in Matrigel (denoted with an arrowhead). (**H, H', H''**) bRPE did not attach to the RCVRN-positive photoreceptors in the RO (gap indicated by a bracket in the composite image). Composite images are counterstained with Dapi. Scale bars: (D, G) 100 µm (E, H) 10 µm

To stabilize the RO photoreceptor OS, another approach was conducted which did not involve a coculture with RPE. Instead, ROs were embedded in Matrigel (Figure 25A, B). The embedding was performed with fixed ROs, or with viable ROs which were cultured in Matrigel for four different time spans (4 hours, 24 hours, 48 hours, or 7 days) prior to harvest. Control ROs were not embedded in Matrigel. The number of PRPH2- or ROM1-positive OS relative to the number of RCVRN-positive IS was determined in HD #1, #2, and 3 ROs. All embedded ROs retained more of their photoreceptor OS than the control ROs (Figure 25C-F). The highest rate of retention was observed in the viable ROs embedded for 24 hours. Interestingly, the ROs embedded for 7 days showed a lower rate of retention (and disorganized histoarchitecture), which may indicate that the Matrigel negatively affects RO viability, perhaps by obstructing nutrient accessibility.
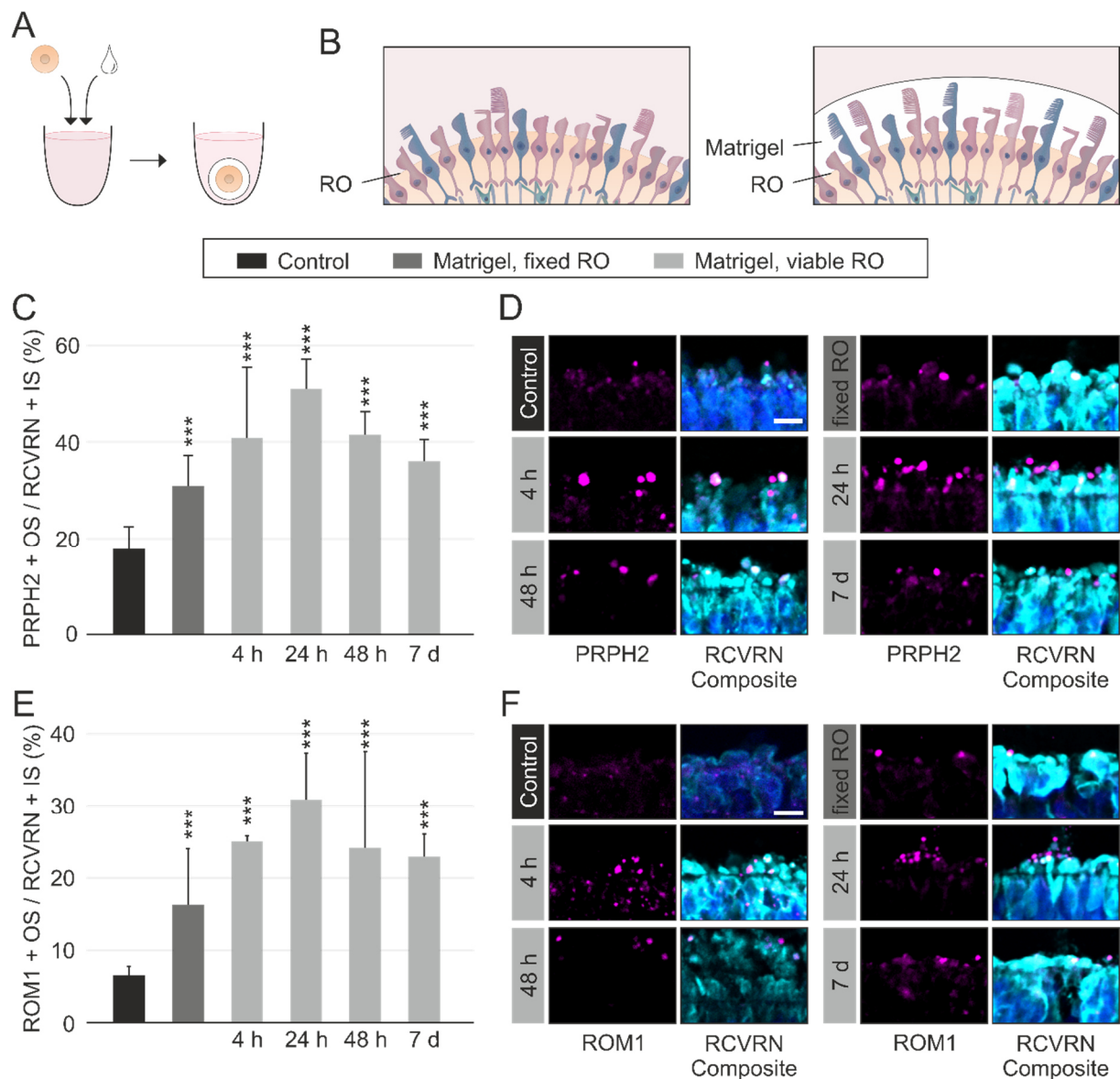
Figure 25: Matrigel-embedding of viable and fixed ROs improve photoreceptor OS retention. (**A**) A schematic representation of the Matrigel-embedding procedure is shown (Matrigel is depicted as a white droplet). (**B**) A schematic representation of photoreceptor OS loss during processing without Matrigel-embedding (left image), and improved photoreceptor OS retention in Matrigel-embedded ROs (right image), is shown. (**C**) The percentage of PRPH2-positive photoreceptor OS relative to the number of RCVRN-positive photoreceptor IS is shown. ROs embedded in Matrigel for 24 hours showed the highest proportion of photoreceptors with preserved OS (51 ± 6.1 % vs. 17.8 ± 4.6 % in control ROs, $p = 0.0001$). (**D**) Exemplary PRPH2- and RCVRN-immunostained images quantified in (C) are shown. (**E**) The percentage of ROM1-positive photoreceptor OS relative to the number of RCVRN-positive photoreceptor IS is shown. ROs embedded in Matrigel for 24 hours showed the highest proportion of photoreceptors with preserved OS (30.9 ± 6.4 % vs. 6.6 ± 1.2 % in control ROs, $p = 0.003$). (**F**) Exemplary ROM1- and RCVRN-immunostained images quantified in (E) are shown. Composite images are counterstained with Dapi. Scale bars: 10 µm, ** $p < 0.01$ (Bonferroni-corrected)

6.6. RO Maturation

To date, very little is known about *in vitro* organoid maturation beyond ~10 months. The oldest organoids ever investigated are cerebral organoids which were cultured for 23 months (130). In this study, the expression profile and cellular composition of ROs, was evaluated at four timepoints: 6, 12, 18 and 24 months.

First, the expression profiles were analyzed. PCA analysis indicated an effect of RO maturation in PC1 (24.37 % of variance, Figure 15) and the number of DEGs was highest in the comparison of 6 and 24-month-old ROs (6,171 DEGs, Supp. Figure 3), suggesting a strong effect of RO maturation on mRNA expression. To characterize this effect, pathway enrichment was performed with DEGs upregulated over time. The top 10 pathways enriched in DEGs upregulated at 12 months (in comparison to 6 months, Figure 26A), 18 months (in comparison to 12 months, Figure 26B), 24 months (in comparison to 18 months, Figure 26C), and 24 months (in comparison to 6 months, Figure 26C), are shown. Enriched pathways included anatomical structure development, nervous system development, multicellular organism development, cell differentiation, and regulation of cell communication.
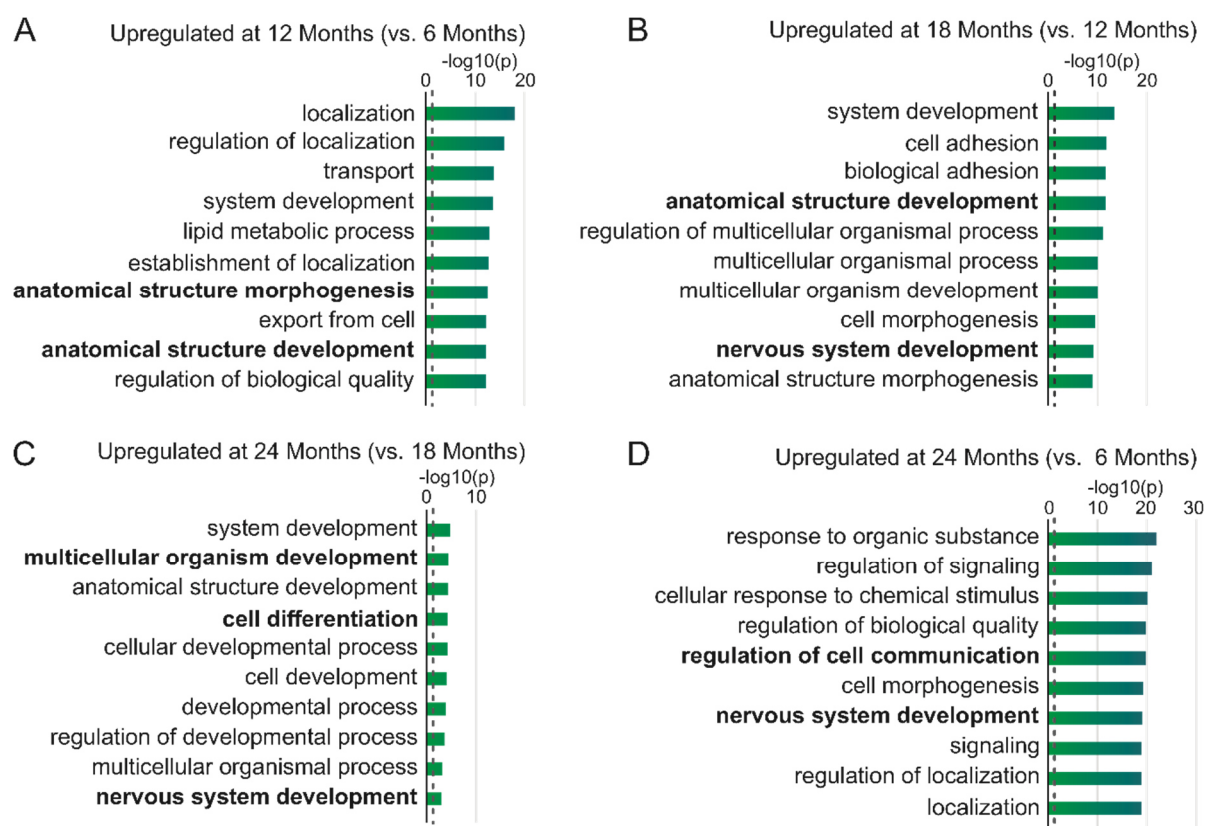
Figure 26: Top ten enriched pathways of DEGs upregulated over time. The top ten enriched GO:BP pathways for four comparisons are shown: (**A**) DEGs upregulated at 12

months (in comparison to 6 months), (**B**) DEGs upregulated at 24 months (in comparison to 18 months), (**C**) DEGs upregulated at 18 months (in comparison to 12 months), and (**D**) DEGs upregulated at 24 months (in comparison to 6 months). Several important pathways are written in bold. Green bars indicate -log10(p), and the threshold for significance (p = 0.05) is shown as a dashed line.

To characterize the effect of RO maturation on cellular composition, the expression of cell-type specific markers for several retinal cell types was determined. Mueller cell marker expression steadily increased over time (Figure 27A). Immunostaining for a Mueller cell marker (RLBP1) confirmed the presence of Mueller cells in ROs up to 24 months (Figure 27B).
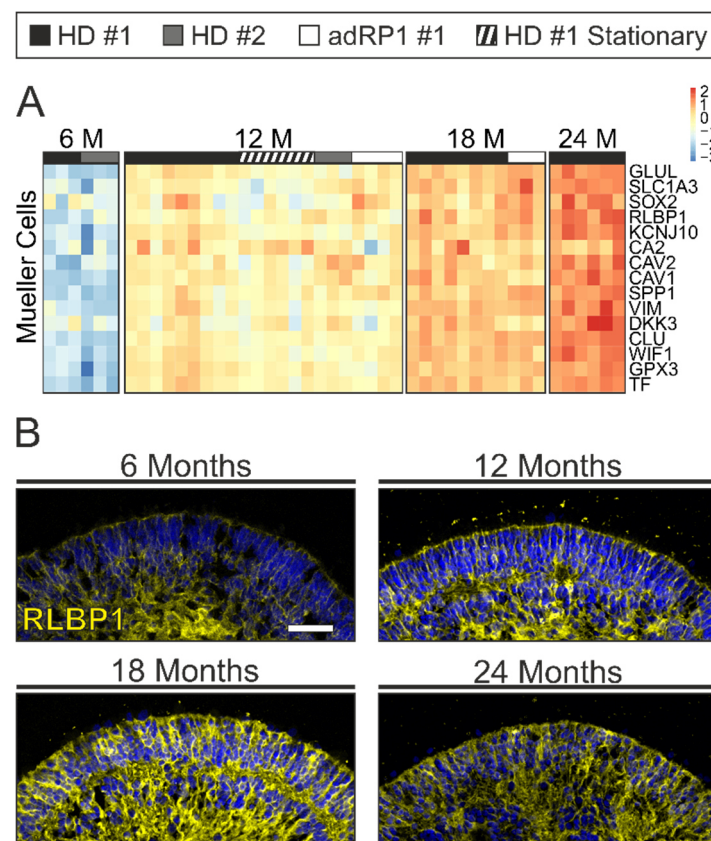
Figure 27: Mueller cell marker expression increases over time. (**A**) A heatmap of 15 Mueller cell markers is shown. The black, grey, white, and striped bar directly above the heatmap denotes the origin of the samples. The expression of all 15 markers increased gradually over time and was significantly higher in 24-month-old ROs than in 6-month-old ROs. (**B**) ROs from four timepoints (6 months, 12 months, 18 months, and 24 months) show the preservation of the Mueller cell marker RLBP1 expression over time. Images are counterstained with Dapi. Scale bar: 50 µm

Pathway enrichment was also conducted for DEGs downregulated over time. The top 10 pathways enriched in DEGs downregulated at 12 months (in comparison to 6 months, Figure 28A), 18 months (in comparison to 12 months, Figure 28B), 24 months (in comparison to 18 months, Figure 28C), and 24 months (in comparison to 6 months, Figure 28D), are shown. Downregulated pathways indicated an effect of RO

maturation on photoreceptor activity: detection of light stimulus, visual perception, and neuron development pathways were enriched in DEGs downregulated over time.
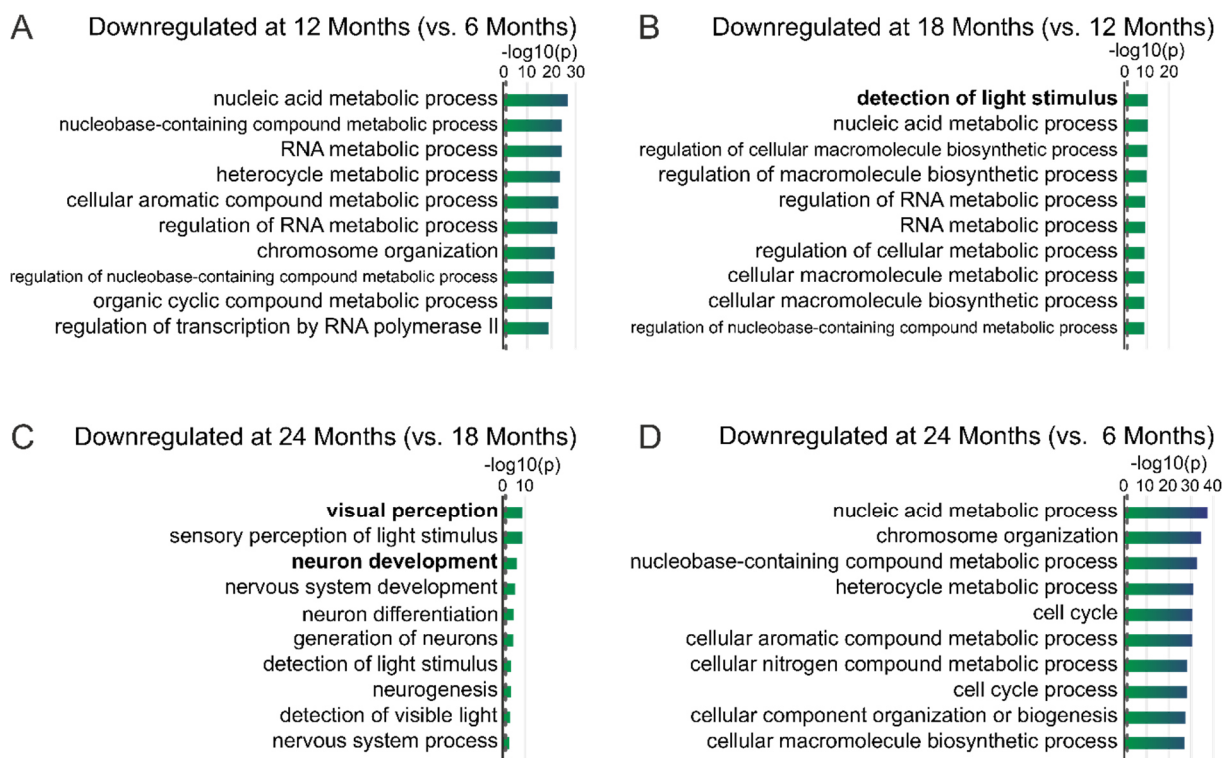
Figure 28: Top ten enriched pathways of DEGs downregulated over time. The top ten enriched GO:BP pathways for four comparisons is shown: (**A**) DEGs downregulated at 12 months (in comparison to 6 months), (**B**) DEGs downregulated at 18 months (in comparison to 12 months), (**C**) DEGs downregulated at 24 months (in comparison to 18 months), and (**D**) DEGs downregulated at 24 months (in comparison to 6 months). Several important pathways are written in bold. Green bars indicate -log10(p) and the threshold for significance (p = 0.05) is shown as a dashed line.

To further characterize the effect of RO maturation on photoreceptor viability, heatmaps were constructed with markers for photoreceptors (expressed by rod and cone photoreceptors) and markers specific to cone photoreceptors (Figure 29A, B). The marker genes were manually curated from literature (107,108), and cross-referenced with The Human Protein Atlas (109–111). All photoreceptor markers were significantly downregulated in the 24-month-old ROs compared to the 6-month-old ROs. To confirm this effect on protein level, ROs from each timepoint were immunostained with several photoreceptor markers. The immunostaining revealed an expression pattern which was reminiscent of *in vivo* photoreceptors: Retinoschisin 1 (RS1), ATPase Na+/K+ transporting subunit alpha 3 (ATP1A3), and Potassium voltage-gated channel subfamily B member 1 (KCNB1) are all expressed at the photoreceptor IS membrane. As suggested by the mRNA expression profiles, the number of RS1-positive cells decreased over time (Figure 29C). Interestingly, within

the remaining photoreceptors, the protein expression pattern appeared to improve over time, and the best RS1- and ATP1A3 expression at the IS membrane was observed in a 24-month-old RO (Figure 29D). Similarly, KCNB1-positive cells appeared to decrease over time, but there were still photoreceptors with KCNB1 expression at the IS membrane after 24 months in culture (Figure 29E). The mRNA expression data also reflected a general reduction of RS1, ATP1A3 and KCNB1 expression over time (Figure 29F).

Figure 29: Photoreceptor marker expression decreases over time. Heatmaps of (**A**) photoreceptor markers (these markers are not subtype specific for rod or cones) and (**B**) cone photoreceptor markers are shown. The expression of all 15 markers decreased over time and was significantly lower in 24-month-old ROs than in 6-month-old ROs. The black, grey, white, and striped bar directly above the heatmap denotes the origin of the samples. (**C**) In general, few photoreceptors showed RS1 or ATP1A3 expression. (**D**) Individual photoreceptors showed pristine RS1 and ATP1A3 expression correctly localized at the membrane of photoreceptor IS. The best RS1 and ATP1A3 expression pattern was seen in a 24-month-old RO. The position of the magnified images shown in (D) are denoted as white boxes in (C). (**E**) In general, few

photoreceptors showed KCNB1 expression, although individual photoreceptors showed KCNB1 expression correctly localized at the membrane of photoreceptor IS (arrowheads). (**F**) The normalized expression levels of the markers stained in (C-E) is shown. ATP1A3 and KCNB1 were significantly downregulated over time, whereas the reduction in RS1 expression was not significant. Scale bars: 10 µm. *** $p < 0.001$

One interesting cell type in the context of RO maturation is the retinal ganglion cell. Previous reports indicate that RO ganglion cells do not survive past a few months in culture (126). We examined the mRNA expression of four ganglion cell markers (BRN3A, POU4F2, ATOH7, ISL1) and observed that they were still expressed even after 24 months in culture (Figure 30A). This indicates that there may still be a small population of ganglion cells that survive in long-term RO cultures. To test this theory, ROs were immunostained for SNCG, a ganglion cell marker. Immunostainings suggested several SNCG-positive cells, but the identity of these cells was still unclear, since some horizontal and amacrine cells also express SNCG. To further clarify the identity of the SNCG-positive cells, the ROs were counterstained with Prospero homeobox 1 (PROX1; a horizontal cell marker) and TFAP2A (an amacrine cell marker). The immunostainings revealed the presence of PROX1-positive / SNCG-positive horizontal cells (Figure 30B, blue arrows) and TFAP2A-positive / SNCG-positive amacrine cells (Figure 30C, blue arrows) at every timepoint. Many ROs also contained PROX1-negative / SNCG-positive cells or TFAP2A-negative / SNCG-positive putative ganglion cells, located towards the RO core (Figure 30B, C; yellow arrows). Furthermore, the immunostainings showed preserved stratification with the ONL, OPL, INL, IPL, and GCL (Figure 30B, C).

Figure 30: Long-term ROs retain low expression of ganglion cell markers. (**A**) The normalized expression of four ganglion cell markers (BRN3A, POU4F2, ATOH7 and ISL1) is shown. All four markers were expressed in ROs at all timepoints. (**B**) 6-, 12-, 18-, and 24-month-old ROs contain SNCG-positive (white) and PROX1-positive (green) cells. The SNCG-positive plexiform layers demarcate the ONL and INL. Magnified images show the presence of SNCG-positive / PROX1-positive horizontal cells (blue arrows) and SNCG-positive / PROX1-negative putative ganglion cells (yellow arrows). The location of the magnified images is denoted with a yellow square. (**C**) 6-, 12-, 18-, and 24-month-old ROs contain SNCG-positive (white) and TFAP2A-positive (magenta) cells. Magnified images show the presence of SNCG-positive / TFAP2A -positive amacrine cells (blue arrows) and SNCG-positive / TFAP2A-negative putative ganglion cells (yellow arrows). The location of the magnified images is denoted with a yellow square. Images were counterstained with Dapi. Scale bar: overview 50 µm, magnified images 10 µm

6.7. adRP1 ROs

ROs were used to determine the phenotypic repercussions of adRP1 in a culture *in vitro* model system. Therefore, ROs were differentiated from two adRP1 patients (Figure 31A-C, Supp. Figure 4) and the morphological development, differentiation efficiency, cellular composition and expression profiles were characterized after 4, 5, 12 and 18 months.
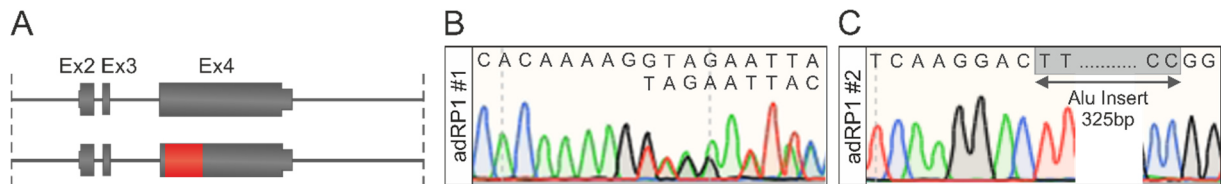
Figure 31: adRP1 iPSC lines. (**A**) Schematic representation of *RP1*. The region which harbors autosomal dominant mutations is shown in red. (**B**) Sanger sequencing of the cell line adRP1 #1, showing the location of the disease-causing single nucleotide deletion (c.2117delG). (**C**) Sanger sequencing of the cell line adRP1 #2, showing the location of the disease-causing retrotransposon insert (c.2321_2322insAluYa5). The full retrotransposon sequence is shown in Supp. Figure 4.

First, aspects of early development were analyzed in 4- and 5-month-old ROs. The RO differentiation efficiency, RO survival, and general morphological development were not significantly different in the patient ROs when compared to control ROs (Figure 32A-C). Next, in-depth analyses were conducted to characterize their cellular composition. The relative CRX-positive area and ONL length were comparable in the patient and control ROs (Figure 32D, E). Since RP primarily affects the rod photoreceptors, the relative RHO- to RCVRN-positive area was quantified (Figure 32F, G). While adRP1 #1 ROs had a lower relative RHO-positive area than HD #1 ROs, it was not lower than the HD #2 ROs, indicating that the observation may not have been a direct repercussion of the *RP1* mutation, but instead may reflect a donor-dependent effect. In humans, the age of symptom onset for adRP1 is the 2nd-6th decade of life (82,84,85), so further experiments were performed to characterize aged ROs.
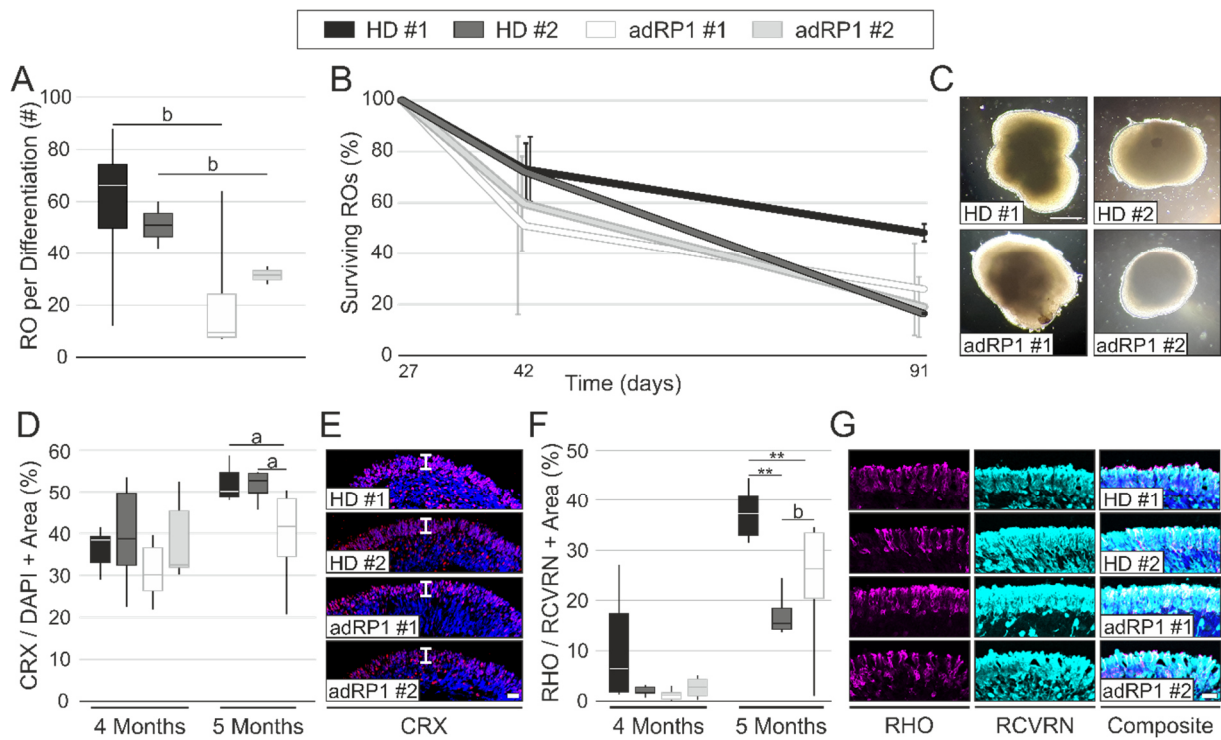
Figure 32: Short-term adRP1 and HD ROs are generally comparable. (**A**) The number of ROs acquired per differentiation are shown. The adRP1 RO yield was slightly lower than the HD RO yield, although this trend was not significant. (**B**) The percentage of surviving adRP1 and HD ROs was comparable over time. (**C**) Brightfield images show that adRP1 and HD ROs are morphologically similar. (**D**) The relative CRX-positive area in 4- and 5-month-old ROs is shown. The 5-month-old adRP1 #1 ROs tended to have fewer CRX-positive photoreceptors, although this effect was not significant. (**E**) 4-month-old adRP1 and HD ROs contain a comparable number of CRX-positive photoreceptors and similar ONL thickness (denoted as brackets). (**F**) The ratio of RHO- to RCVRN-positive area in 4- and 5-month-old ROs is shown. 5-month-old adRP1 #1 ROs had a lower proportion of rod photoreceptors than HD #1 ROs but tended to have a higher proportion of rod photoreceptors than HD #2 ROs. (**G**) 4-month-old adRP1 and HD ROs contain RHO-positive rod photoreceptors and RCVRN-positive photoreceptors. Composite images were counterstained with Dapi. Scale bars: 25 µm; ** $p < 0.01$; a: $0.05 < p < 0.06$; b: $p \geq 0.06$

The cellular composition and expression profiles of 12- and 18-month-old adRP1 and HD ROs were evaluated. While the relative CRX-positive and RHO- to RCVRN-positive area was comparable in the 12-month-old ROs, both were reduced in the 18-month-old adRP1 ROs (Figure 33A-D). This effect was remarkable, but not significant due to low sample size ($p = 0.053$). To confirm the effect, the mRNA expression of seven rod photoreceptor markers was evaluated. All seven rod markers were downregulated in 18-month-old ROs, while NR2E3 expression was downregulated in the 12- and 18-month-old ROs (Figure 33E). Taken together, these results indicate that ROs may be a suitable model system for adult-onset RP such as adRP1, but the phenotype onset in ROs may require a prolonged cultivation period.
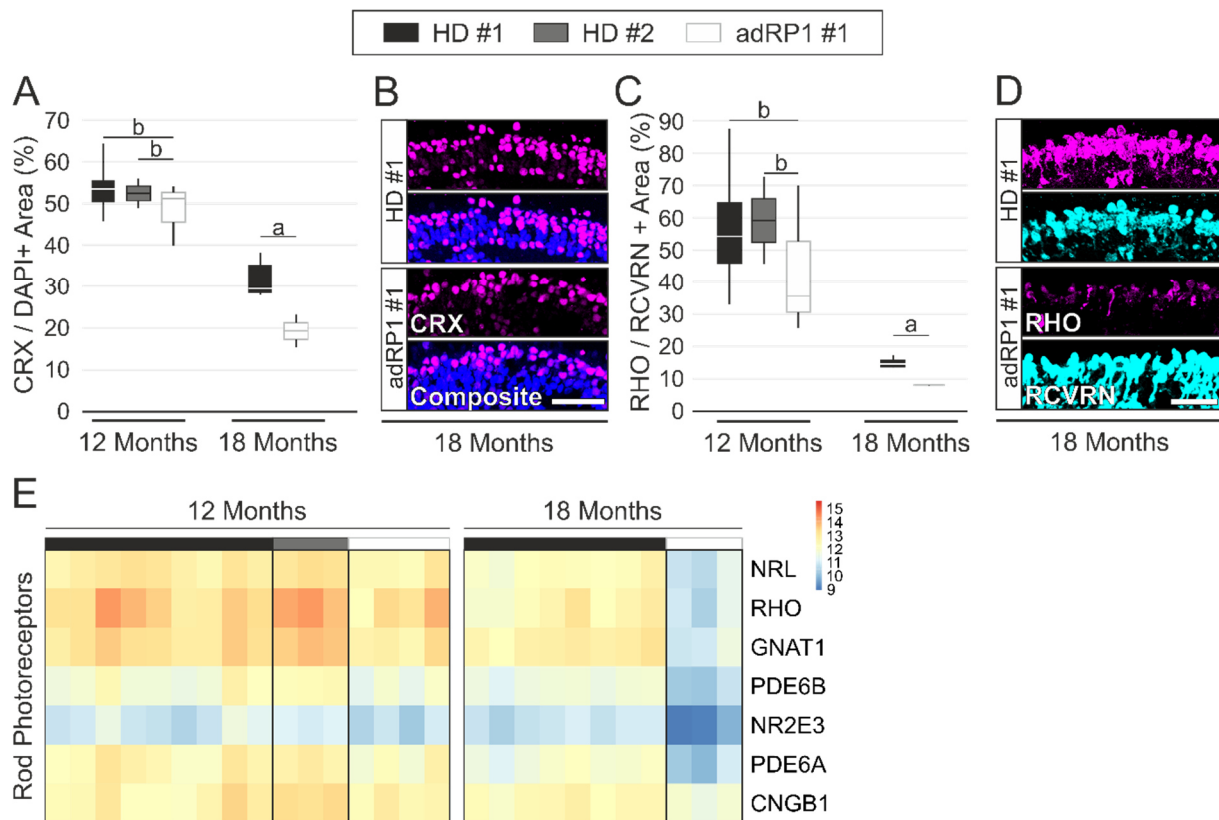
Figure 33: Long-term adRP1 ROs contain fewer rod photoreceptors. (**A**) The ratio of CRX-to Dapi-positive area in 12- and 18-month-old ROs is shown. The relative CRX-positive area was comparable in 12-month-old ROs. The 18-month-old adRP1 #1 ROs tended to have a lower relative CRX-positive area ($p = 0.053$). (**B**) CRX-positive photoreceptors in 18-month-old adRP1 #1 and HD #1 ROs are shown. (**C**) The ratio of RHO- to RCVRN-positive area in 12- and 18-month-old ROs is shown. The relative RHO-positive area in 12-month-old ROs was comparable, but the 18-month-old adRP1 #1 ROs tended to have a lower RHO-positive proportion. (**D**) 18-month-old adRP1 #1 and HD #1 ROs contain RHO-positive rod photoreceptors and RCVRN-positive photoreceptors. (**E**) A heatmap of rod photoreceptor markers in 12- and 18-month-old ROs is shown. The black, grey, and white bar directly above the heatmap denotes the origin of the samples. All 7 rod photoreceptor markers were downregulated in 18-month-old ROs. NR2E3 was downregulated at 12 and 18 months. Scale bars: 50 µm; a: $0.05 < p < 0.06$; b: $p \geq 0.06$

6.8. *RP1* Knockout ROs

Finally, *RP1* knockout ROs were investigated in comparison to isogenic control ROs. *RP1* knockout iPSC were generated by using the CRISPR/Cas9 technology to target the 2nd exon of *RP1* in iPSC from a healthy donor (Figure 34A). First, seven gRNAs were designed using the "Benchling CRISPR design tool" (115). The editing efficiency of all seven gRNAs was tested in HEK293 cells using an established fluorescence based assay (116). The four gRNAs with the highest efficiency were chosen to edit iPSCs from a healthy donor. Two gRNAs had an acceptable indel rate ($\geq 20\%$), and the iPSC were dissociated to single cells and expanded to single clones.

The single clones were sequenced and two lines with homozygous frameshift mutations (RP1_KO #1 and 2) and two control lines without indels at the target site (RP1_WT #1 and 2) were identified (Figure 34B, C). ROs were differentiated from each iPSC line.
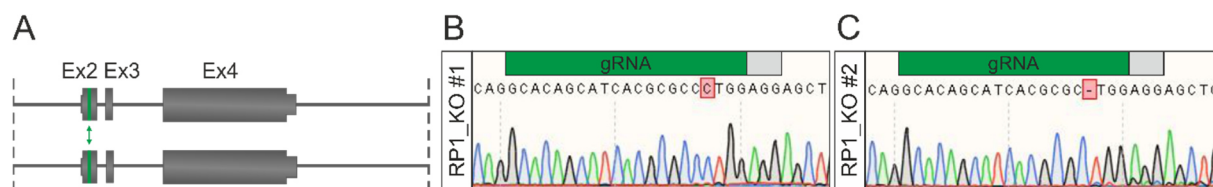
Figure 34: CRISPR/Cas9 mediated gene editing produced RP1_KO iPSC lines. (**A**) Schematic representation of *RP1*. The region targeted with CRISPR/Cas9 is shown in green and emphasized with an arrow. (**B**) Sanger sequencing of the cell line RP1_KO #1, showing the location of the homozygous single nucleotide insertion (c.295insC). The position of the gRNA and PAM sequence are shown. (**C**) Sanger sequencing of the cell line RP1_KO #2, showing the location of the homozygous single nucleotide insertion (c.295delC). The position of the gRNA (green) and PAM (grey) are shown.

The morphological development and cellular composition of the RP1_KO and WT ROs was evaluated after 6 months. The ROs showed comparable morphological development (Figure 35A) and photoreceptor IS and OS outgrowth (Figure 35B). RCVRN and RHO were expressed in all ROs, and RHO transport to the OS was seen in ROs from each genotype (Figure 35C).
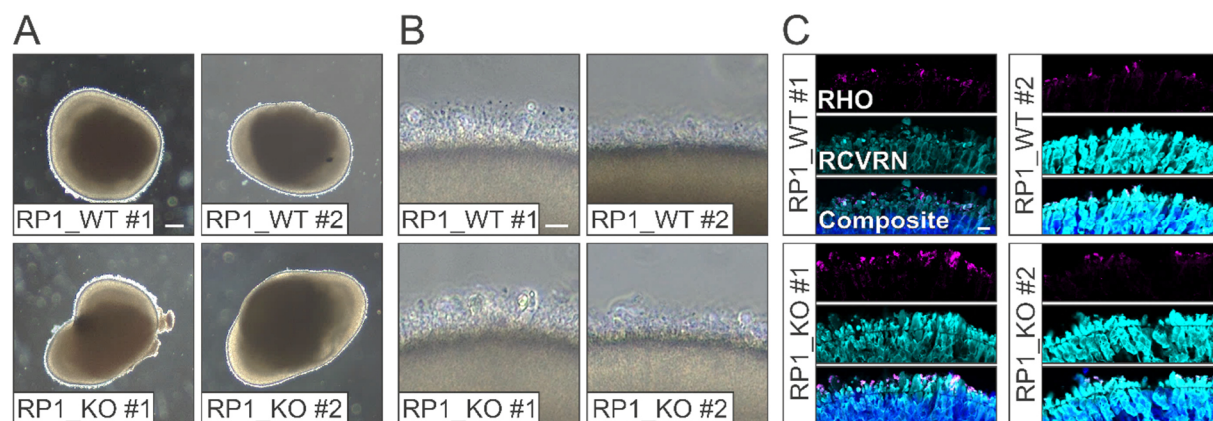
Figure 35: Short-term RP1_KO and WT ROs are comparable. (**A**) Brightfield images of 6-month-old ROs show that RP1_KO and WT ROs are morphologically similar (2x magnification). (**B**) Brightfield images of 6-month-old ROs show photoreceptor IS and OS outgrowth from RP1_KO and WT cell lines (10x magnification). (**C**) ROs from all four lines contain RCVRN-positive photoreceptors. Weak RHO expression is seen in the photoreceptor OS of RP1_KO and WT ROs. Composite images are counterstained with Dapi. Scale bars: 10 μm

7.   Discussion

ROs allow the study of human retinal tissue *in vitro* (60). Nevertheless, they also present challenges, some of which were successfully resolved in this study. One challenge is that several RO differentiation protocols exist, and the impact that each protocol has on the ensuing ROs is unclear. In the present study, ROs were differentiated according to three previously published protocols, and the method which produced the highest quantity and best quality of ROs was identified (Figure 36A). Next, ROs cultured on an orbital shaker were compared to stationary ROs, which revealed no significant differences (Figure 36B). Through these investigations, the variability of ROs was uncovered and characterized. A donor-effect (the iPSC line influenced the ROs protein and mRNA expression), intra-RO variability (regional differences in RO cellular composition), and inter-RO variability (ROs from the same differentiation showed differences in maturation) were observed. Since RO photoreceptors IS and OS were vulnerable to mechanical stress during processing, a technique which doubled the amount of retained photoreceptor OS was developed (Figure 36C).

Another challenge that was addressed here, is the lack of insight into RO development past 11 months. The protein expression, mRNA expression, histoarchitecture, and methylation signature of up to 2-year-old ROs was analyzed (Figure 36D), which revealed that the preservation of retinal histoarchitecture and upregulation of Mueller cell markers over time. Pathway analysis also revealed the upregulation of anatomical structure development and nervous system development pathways. In general, photoreceptor marker expression decreased over time, but immunostaining revealed photoreceptors with pristine morphological development were present in 2-year-old ROs. The analysis of RO methylation signatures is currently underway, but preliminary analyses indicate that 1-year-old ROs cluster close to adult human retinal samples.

In the second part of this study, two genetically distinct causes for RP were investigated. First, ROs were used as a model system for adRP1, which causes adult-onset RP with degeneration of rod photoreceptors (131). Investigations of 4-, 5-month-old, and 1-year-old adRP1 ROs and HD ROs showed comparable photoreceptor development. In contrast, 1.5-year-old adRP1 ROs showed a reduction in rod photoreceptor marker expression, indicating that long-term RO cultures may be

suitable to model adult-onset RP (Figure 36E). ROs were also used to evaluate an RP subtype with an earlier age of symptom onset (85). In this project, CRISPR/Cas9-mediated gene editing was used to produce *RP1* knockout and isogenic control iPSC, thereby reducing the likelihood of a donor-effect overshadowing a RP phenotype. Investigations into 6-month-old ROs showed comparable morphological development, cellular composition, photoreceptor IS and OS outgrowth, and RHO trafficking to the OS (Figure 36F). Overall, the broad range of topics addressed in this study helped provide in-depth insight into RO development, techniques to improve ROs as a human retinal model, and their applicability as a model system for inherited retinal dystrophies.
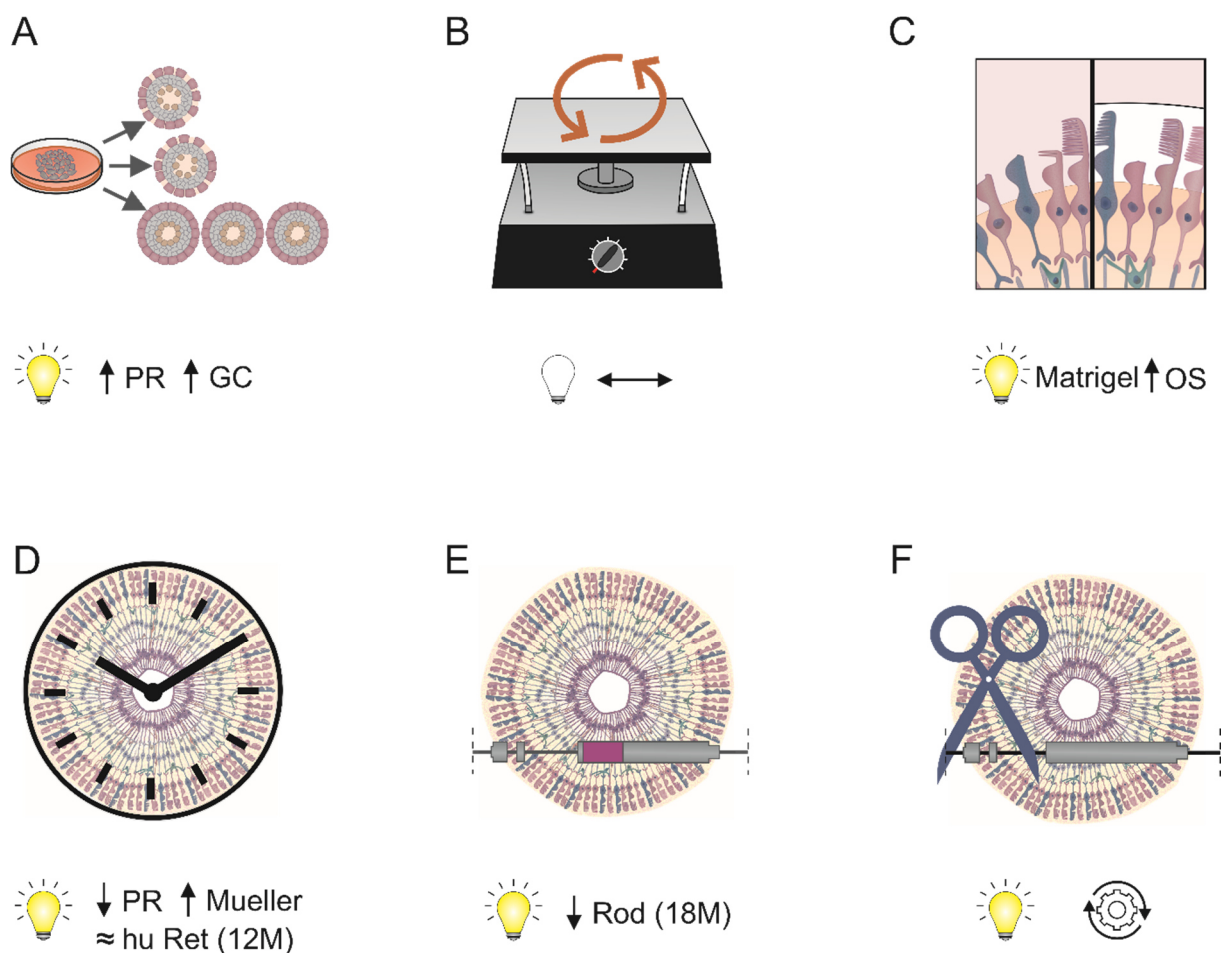
Figure 36: RO characterization and application as an RP model system. (**A**) ROs were differentiated following three published methods (M1-3). M3 produced more ROs, which contained more CRX-positive photoreceptors and BRN3A-positive ganglion cells than ROs produced with M1 and M2. (**B**) orbROs were comparable to statROs in terms of their histoarchitecture, cellular composition and expression profiles. (**C**) The retention of RO photoreceptor OS was improved by embedding viable ROs in Matrigel for 24 hours. (**D**) Long-term culture of ROs revealed the downregulation of photoreceptor markers and upregulation of Mueller markers after 2 years. Methylation profiles of 1-year-old ROs were most comparable to the methylation profiles of human retina samples. (**E**) adRP1 ROs showed a downregulation

of rod photoreceptor markers after 1.5 years. (**F**) *RP1* knockout iPSC were generated using CRISPR/Cas9 and differentiated to ROs. 6-month-old edited and control ROs were comparable in terms of IS and OS outgrowth and RHO trafficking to the OS.

Despite the breadth of knowledge gained in the course of this study, challenges and unresolved questions about ROs remain. Analyses of protein and mRNA expression, as well as morphological development and histoarchitecture, revealed no significant differences between orbROs and statROs. This result is surprising, specifically as two independent research groups have previously reported improved photoreceptor yield and accelerated differentiation in mobile RO cultures (91,92). Also, brain organoids are regularly cultured in mobile conditions, demonstrating its relevance in a related model system (35,132–134). Besides the encouraging data by other groups, a positive impact of a mobile culture system on 3D tissue development intuitively makes sense. Organoids do not develop a vascular system making them vulnerable to hypoxia, and mobile culture facilitates the aeration and distribution of fresh media. This should be especially helpful for *in vitro* cerebral and retinal development, since these tissues have a high metabolic demand (4,135–137).

There are several possible explanations why the orbROs and statROs failed to show significant differences in this study, although some explanations are more likely than others. Here, orbROs were placed on the orbital shaker after 42 days, which is later than previous reports (31 days (91), or 10 days (92)). Still, we characterized up to 1-year-old orbROs and statROs, at which point the orbROs had been in mobile culture for over 10 months. So, a later starting time is not a satisfying explanation for the lack of significant results in the orbROs. As mentioned above, many previous publications have leveraged mobile culture conditions for organoid development, but most groups use very different procedures to perform mobile culture, ranging from stirred tank bioreactors (91), rotating-wall vessel bioreactors (92), custom 3D-printed SpinΩ bioreactors (132), or the scrappy albeit unsophisticated bioreactors created by gluing pieces of reaction tubes to 6-cm petri dishes on an orbital shaker (138). Still, each of these bioreactors produces a mobile culture system, so the difference in the exact type of mobile culture we used (an orbital shaker) cannot explain our lack of significant differences. Instead, the most likely explanation is that in this experiment, the effect of mobile culture was likely overshadowed by RO variability.

RO variability was not a unique finding of this study. Hallam et al. showed that five different iPSC lines exhibited significant variability in their efficiency to generate

ROs (99). Chichagova et al. demonstrated that RO differentiation was line- and method-dependent using three independent iPSC clones (139). Mellough et al. further underscored cell-line specific effects, and theorized that inconsistencies introduced during early differentiation likely drive the variability in differentiation efficiency (140). Taken together, these data indicate that RO variability is a prevalent and pressing issue and is not isolated to one lab or differentiation method. The surprising insight into RO variability, which was gained in this study, was that a high degree of RO variability persisted, even though several measures were taken from the outset to reduce and control for RO variability.

First, to account for regional variability, at least three complete cryosections were analyzed per RO, instead of the widely accepted approach of focusing on highly magnified images for quantification (74,141–143). Second, ROs were cultured in solitary wells instead of grouping them together, since this culture technique had reduced RO variability in a previous study (99). This approach was further supported by data from an independent study, showing that group cultures induce batch effects on mRNA expression (36). Third, to confirm comparable pluripotency of the iPSC, a mRNA-based PluriTest was conducted, which is a far more sophisticated analysis than the traditional demonstration of pluripotency via ICC (97,98,144). While all iPSC lines passed the PluriTest statistical thresholds, a donor effect was still observed on RO protein and mRNA expression. The donor effect is a particularly interesting aspect of RO variability. The iPSC lines were derived from healthy individuals with no history of retinal disease, so it is curious why they produced ROs with variable efficiency and quality. Possible explanations for the iPSC donor effect include incongruences introduced during reprogramming, changes in epigenetic profiles due to suboptimal handling, or the acquisition of spontaneous genetic insults during culture. Still, if the iPSC donor effect on ROs cannot be largely resolved, this would greatly hinder further studies which aim to characterize disease phenotypes with a mild phenotypic manifestation.

So far, one group has documented reproducible differentiation of ROs across multiple iPSC lines, when they successfully differentiated 16 iPSC lines to ROs (47). While they successfully differentiated ROs from each iPSC line, they also experienced RO variability. In particular, the formation of photoreceptor IS and OS was observed after as little as 4.25 months, while other ROs did not show outgrowth until month 6. This underscores that the rate of RO maturation is not uniform among the ROs. It is

quite curious, why the development of a tissue which underlies strict temporal regulation *in vivo* (reviewed in (16,19)), shows such inconsistent development timing *in vitro*. In contrast to the donor effect discussed earlier, the crux of inter-RO variability may not lie within the iPSC themselves. Instead, a logical conclusion may be that the RO differentiation techniques developed so far (although remarkable in their ability to produce ROs with a cellular diversity and histoarchitecture similar to native tissue), are still suboptimal in terms of consistency (reviewed in (145)). To truly tackle the problem of RO variability, the differentiation protocols should be further adapted and optimized with a focus on producing uniform ROs.

The next steps to solving 3D culture variability may currently elude RO researchers, but it is not unattainable for organoid researchers as a collective. In 2019, a truly remarkable body of work was published, which debuted a dorsal forebrain organoid differentiation protocol producing organoids with a virtually indistinguishable cellular composition, as demonstrated via single-cell RNA-sequencing (36). It appears fitting, that brain organoid researchers are the first to resolve the challenge of organoid variability, since brain organoids were the first organoid system to be developed. In late 2008, two research groups independently published the differentiation of mouse embryonic stem cells to 3D cortical tissue, thereby replicating spatial and temporal corticogenesis *in vitro* (33,146). In the same issue of Cell Stem Cell, Au et al. lauded the researchers remarkable achievements in an article entitled "Cortex Shatters the Glass Ceiling" (147). At the time, this was understandably seen as a most innovative advancement, but as the years passed, researchers began trying to answer increasingly complex questions with cerebral organoids. As is currently the case within the RO research community, brain organoid researchers began to uncover and appreciate organoid variability, and documented their findings and concerns ((148,149) reviewed in (150,151)). Initially, it was proposed that researchers should construct their experiments to compensate for inter-organoid variability and donor-effects by using multiple patient and control iPSC lines when leveraging organoids as a disease model (151). This is a justifiable suggestion, but it is hard to translate to real-life working conditions. Brain organoid (and RO) cultures are time- and labor-intensive, and if multiple differentiations are conducted simultaneously, the body of work quickly escalates to require active handling on 365 days a year. Furthermore, organoid cultures require a heightened attention to detail, as bacterial or fungal contaminations render affected cultures unsalvageable. Ultimately, increasing the number of iPSC

lines and differentiations per experimental approach do not address the root of the problem. As long as the cellular composition, maturation, and temporal regulation of organoid development is inhomogeneous, there will always be a risk that variability could overshadow the results of an experiment.

Brain organoid variability stifled progress until 2019, when it was successfully resolved by the Arlotta group (36). Velasco et al. started with a previously developed differentiation protocol and implemented multiple small modifications with the aim of enhancing reproducibility. The parameter used to measure uniformity was the organoid size and shape. This parameter may initially appear to be rather crude. After all, the real aim was to improve much more sophisticated aspects of brain organoids, e.g. the cellular composition, maturation and temporal regulation. After careful consideration however, it becomes clear that organoid size and shape are well thought parameters, because these aspects of brain development are tightly regulated *in vivo*. 3D MRI imaging revealed that brain volume was highly correlated in monozygotic twins, but not in dizygotic twins (152,153), indicating that brain volume is greatly heritable. Therefore, organoids differentiated from the same iPSC line should be of the same size. Velasco et al. went even further and optimized their differentiation protocol to produce similar sized brain organoids across 4 induced pluripotent and embryonic stem cell lines. Their optimized protocol produced organoids with a cellular composition that had a sample-to-sample reproducibility similar to that of endogenous human and mouse brains (36).

The optimization of this protocol is clearly a remarkable achievement and was certainly a massive undertaking. The logical next question is whether a similar approach could help RO researchers to overcome variability. Unfortunately, the exact steps implemented by Velasco et al. cannot be directly applied to RO differentiation, as those differentiation stimuli guided the cells towards a dorsal forebrain fate, not a retinal fate. Still, there are ways with which to emulate the strategy used by Velasco et al. For example, using RO size as a parameter to optimize RO reproducibility may work nicely, since eye size is also highly heritable (154–156). The question remains, however, which specific steps should be modified within the RO differentiation protocol to enhance reproducibility. The best strategy to tackle this question is probably to consider physical and chemical differentiation stimuli separately. Many organoid differentiation protocols start with the dissociation and reaggregation technique originally pioneered by Pierce et al. in 1961 (157). The RO differentiation protocol used here, induces dissociation and reaggregation on the first day of differentiation. The

ensuing aggregates, however, are not uniform in size or shape (59). This procedure could be optimized either by plating the dissociated cells in a micro- or milliwell platform (158,159), or simply by passing the aggregates through filters to sort out the aberrantly sized ones. Of note, the latter strategy was attempted during this study, but the filter clogged easily, resulting in a vast decrease in the number of aggregates. At the time, the decision was made to omit the filtration step, since literature reviews had underscored the importance of using large sample sizes to control for variability (151,160). In retrospect, this filtration step may have improved RO uniformity, thereby making up for a reduction in sample size. To address the blockages, the filtration could have been performed stepwise to progressively sort out the aberrant aggregates. Alternatively, the starting number of aggregates could have been increased, to compensate for the reduction during filtration.

Next, the chemical differentiation stimuli should be examined and optimized. Currently, there are two main approaches for orchestrating the chemical microenvironment during RO differentiation: cell-led differentiation with mild chemical stimuli (59), or layered chemical stimuli where multiple pathways are concurrently or consecutively manipulated to induce retinal differentiation (45). One achievement of this project was to uncover the improvements of RO differentiation quality following BMP4 treatment (161). Besides the BMP signaling pathway, there are three other important pathways which are involved in retinogenesis: hedgehog, Wnt and Notch (reviewed in (17)). These pathways are involved in retinogenesis *in vivo*, so it stands to reason that they could also be beneficial for RO differentiation *in vitro*. Of note, all three of these pathways were manipulated in the M1 RO differentiation method (45), which produced poor quality ROs (161), but that may not have been caused by a suboptimal chemical microenvironment. M1 utilized a 3D differentiation approach, as opposed to the 3D-2D-3D approach used in M2 and M3. In general, it is difficult to decide whether 3D-2D-3D protocols are better than 3D protocols per se, but it might be worthwhile to combine the most promising aspects of each differentiation technique. Therefore, one could combine M3 (with the BMP4 treatment) with the signaling factors used in M1, in a M1-3 hybrid differentiation protocol.

If the cellular diversity and spatiotemporal maturation of ROs could be standardized, this could lead to a major improvement for RO research, hopefully allowing more groups to successfully leverage ROs as disease models. Still, even uniform ROs are not ideal to model diseases such as RP or LCA which primarily affect

the photoreceptors. As long as the photoreceptors in ROs are not physically protected by the RPE as they are *in vivo*, the photoreceptors in the ROs are subjected to an inherently fragile condition. In this study, several bRPE-RO coculture techniques were designed and tested, but reproducible and intimate contact between the bRPE and RO photoreceptors was not achieved. Previous studies have also attempted to establish RPE-RO coculture systems, but in those reports, the authors did not focus on the physical interaction between the RPE and photoreceptors (112,162). In this project, we focused on the photoreceptor axoneme, since this is where RP1 is expressed and likely produces a pathologic phenotype in adRP1 and arRP1 (86,87). Ultimately, we successfully stabilized the photoreceptor OS through Matrigel embedding. Still, it is curious why the bRPE and RO photoreceptors do not show robust interaction *in vitro*. Poor bRPE quality was probably not the cause for the lack of interaction, since the bRPE cells revealed RPE-marker expression on mRNA and protein level, as well as the ability of bRPE to phagocytose POS, very similar to traditionally generated iPSC-RPE (94) or *in vivo* RPE cells. It could be possible that the bRPE and RO photoreceptors were simply under too much physical stress to properly interact. *In vivo*, the RPE envelop photoreceptor OS through protrusions known as microvilli ((163) reviewed in (164)). It stands to reason that these microvilli are necessary for the physical stabilization of the RPE and photoreceptor contact. *In vitro*, RPE microvilli develop over the course of several weeks (94). It is possible, that a bRPE-RO coculture could produce a stable interaction between the RPE and photoreceptors, if the cocultured cells could be kept physically stable for several weeks. This concept would be extremely difficult to execute in a laboratory setting, since the cultures require at least biweekly medium exchanges. In our hands, even the gentlest medium exchanges sheered the bRPE off the ROs.

It is also possible that the coculture timepoint chosen in our experiments was simply too late, since invagination occurs by embryonic day 32 and the cocultured ROs were at least several months old. The delay was necessary to isolate and cultivate the bRPE, but it may have negatively affected the coculture. Of note, an optimal RO differentiation protocol should replicate the formation of a bilayered optic cup, thereby allowing the simultaneous differentiation of RPE and neural retina. *In vitro* invagination has only repeatedly been shown in mouse stem cells by the group that pioneered RO research, although they reported difficulties when replicating the invagination with human stem cells (33,44,165). In the present study, RO invagination was not actively

pursued. In the past few years, very little work about RO invagination has been published (166). Instead of pursuing *in vitro* RO invagination, we chose to engage in a different course of action by differentiating ROs and bRPE separately and then reuniting the tissues in a coculture system. The coculture experiments shown here, and replicated independently at the institute, failed to achieve the desired results, but they were by no means an exhaustive implementation of all possible coculture techniques. If this avenue should be pursued further, the best technique to try next would probably be to seed juvenile bRPE on a membrane and add the RO. Perhaps the RO could even be sectioned prior to the coculture (167), thereby reducing the likelihood of the coculture failing due to insufficient nutrient supply. Next, the coculture would have to be physically stabilized to allow the bRPE and RO photoreceptors to interact. This could be achieved by adding a second, stabilizing membrane or embedding the bRPE coculture in an ECM-like substance. In our study, Matrigel embedding was tolerated by ROs for 24 - 48 h, but longer embedding such as 7 days or 3 weeks resulted in reduced photoreceptor marker expression, indicating that Matrigel may not be the ideal embedding substance. Many different ECM-like compounds and hydrogels are currently on the market, and it is possible that the ROs could tolerate longer embedding times, if a different compound was used.

Our interest in RO photoreceptor OS arose because RP1 is expressed at the photoreceptor axoneme, and we wanted to leverage ROs as an adRP1 model. In the present study, 4-, 5-month-old, and 1-year-old adRP1 and HD ROs were comparable in terms of RO survival, morphological development, and photoreceptor cellular composition, morphology and histoarchitecture. 1.5-year-old adRP1 and HD RO mRNA expression profiles were not vastly different (there were 769 DEGs in adRP1 #1 vs. HD #1 and 2, compared to 1350 DEGs in HD #1 vs. adRP1 #1 and HD #2), but 7 rod photoreceptor marker genes were downregulated in the patient ROs. This indicates that the adRP1 phenotype may only become apparent in older cultures. This is supported by adRP1 disease progression in humans, as many patients only develop symptoms in adulthood (82,84,85). Still, rod photoreceptor degeneration presumably starts some time before the patient becomes symptomatic. This could explain why we noticed a reduction in rod photoreceptor markers after only 1.5 years, even though patients would probably be asymptomatic at this stage.

Of course, the donor effect on RO mRNA expression may have impacted the adRP1 RO expression profiles in a way which cannot be traced back to the *RP1*

mutation. In contrast to the adRP1 project, the *RP1* knockout project leveraged CRISPR/Cas9 mediated gene editing, in order to produce isogenic iPSC lines. This strategy could have also been applied in the adRP1 project. To this end, CRISPR/Cas9 mediated gene editing could have been used to induce adRP1 mutations in HD iPSC, thereby reducing the likelihood of a donor effect concealing the disease phenotype. A drawback of this approach, however, is that the genetic background of the iPSC would correspond to the HD iPSC line instead of a patient iPSC line, which could also affect the phenotype severity. This in turn could be remedied by correcting the adRP1 mutation in a patient iPSC line using CRISPR/Cas9 mediated homology directed repair (HDR) and a correction template. Unfortunately, the editing efficiency of HDR is very low (168), calling into question whether it would be feasible to repair adRP1 mutations using HDR in iPSC. Regardless of how the mutations are induced or corrected however, ROs would still have to be differentiated and cultured for several months or even years. As we saw in this study, long differentiation times may be necessary to model adult-onset disease in ROs, so it should be considered whether it is possible to increase the rate of RO maturation.

The hallmarks of aging include cellular senescence, telomere attrition, mitochondrial dysfunction, and epigenetic aging (169–171). Epigenetic aging is of particular interest because this is a fairly new field which has been gaining widespread attention as methylation sequencing technology becomes more accessible. A fairly recent study showed that the epigenetic age and chronological age of human fetal retina samples were highly correlated, and this correlation was retained in ROs ((172) reviewed in (169,171)). Still, the oldest ROs investigated in that study were only 90 days old. Here, we examined the methylation signatures of up to 2-year-old ROs. Although these analyses are still underway, preliminary results indicate that the concordance to adult human retinal samples is highest in the 1-year-old ROs. Therefore, increasing the rate of RO epigenetic aging to reflect the methylation status of 1-year-old ROs in chronologically younger cultures could be of interest for future studies.

There are several possible ways in which the rate of epigenetic aging could be increased, including manipulating the expression of enzymatic regulators of epigenetic aging. A previous study has shown that the expression of tet methylcytosine dioxygenase 2 (Tet2), an enzyme involved in DNA demethylation (173), decreased with age in murine hippocampi (174). Loss of Tet2 in the hippocampus of young mice

impaired neurogenesis and cognition, thereby producing an age-related phenotype (174). Downregulation of Tet2, possibly through the use of a short hairpin RNA (175), could therefore potentially accelerate biological aging in ROs. Another approach could be to induce a segmental progeroid syndrome in ROs. Segmental progeroid syndromes are rare genetic disorders that accelerate multiple features of aging, such as alopecia, muscle atrophy, osteoporosis, and atherosclerosis (reviewed in (176)). Epigenetic analysis of tissue samples from segmental progeroid patients (specifically patients with Werner Syndrome and Hutchinson Gilford Syndrome), showed accelerated epigenetic aging (177,178). Furthermore, exposure of iPSC-derived neurons to progerin (the mutant protein expressed in Hutchinson Gilford patients), induced an age-related phenotype resulting in DNA damage and mitochondrial stress (179). The manipulation of epigenetic age via progerin exposure or Tet2 induction, could be fruitful methods with which the biological age of ROs could be increased.

When considering chronological or accelerated RO aging, it is important to note that prior to this study, to the best of our knowledge, ROs had never been examined past ~11 months (330 days; (180)). Through our investigations of up to 2-year-old ROs, we gained valuable insight into RO maturation. For example, although the expression of photoreceptor markers decreased over time, individual photoreceptors with pristine morphological development were observed in 2-year-old ROs. The most likely cause for the observed photoreceptor degeneration, may be due to the fact that RO photoreceptors are cultured in the dark. Photoreceptors are sensory cells which rely on illumination, so it stands to reason that they may degenerate if they are only exposed to light during brief medium exchanges. In contrast, the survival of some photoreceptors suggests that the cells could mature *in vitro*, for example if they were to receive light stimuli. Unfortunately, these conditions are difficult to translate to a laboratory setting, as most if not all RO media contain several light-sensitive components (181). In addition, light exposure may even harm the RO photoreceptors, since they lack supportive RPE, which recycle the photopigments needed for phototransduction (14,15). In contrast to the photoreceptor reduction, Mueller cell marker expression increased over time. Mueller cells are the main glial cell in the retina, and are important for maintaining neural integrity and processing visual information (reviewed in (182,183)). Many retinal diseases evoke Mueller cell gliosis (reviewed in (184)), so it is plausible that photoreceptor degeneration in the older ROs caused the observed upregulation of Mueller cell markers.

Another surprising insight gained into RO maturation, was that ganglion cells persist for at least up to 2 years *in vitro*. This finding was unexpected as previous investigations have indicated that RO ganglion cells degenerate over time, especially after 6 months (47,61). In our study, we saw putative ganglion cells that were PROX1-negative / SNCG-positive, or TFAP2A-negative / SNCG-positive, located towards the RO core. Furthermore, the GCL and INL were also thought to disorganize after 6 months (47), but we saw well-preserved histoarchitecture at every timepoint. Taken together, the photoreceptor downregulation, Mueller cell upregulation, preservation of ganglion cell expression and maintenance of histoarchitecture indicate ROs can survive multiple years of culture, although they are likely stressed especially at later time points. Still, it is possible that the stress response in older ROs could help amplify disease phenotypes that may not be pronounced in younger, less stressed cultures. For example, we saw rod photoreceptor degeneration was more pronounced in 1.5-year-old than in 1-year-old adRP1 ROs.

In summary, this work highlights the advantages and shortcomings of ROs as a human-derived retinal model system. Within this study, we were able to illuminate or even resolve several challenges of RO culture and evaluate their applicability as a patient-derived adRP1 model *in vitro*. We also investigated for the first time, up to 2-year-old ROs which provided valuable insight into *in vitro* RO maturation. Currently, we are examining RO methylation signatures, and the cellular composition and photoreceptor integrity of *RP1* knockout ROs. Future research should focus on the optimization of RO reproducibility, potentially using a M1-3 hybrid differentiation protocol, and accelerating the rate of RO maturation, perhaps by manipulating age-mediating expression such as Tet2 or progerin expression, as discussed in this work.

8. Appendix

8.1. Supplementary Figures
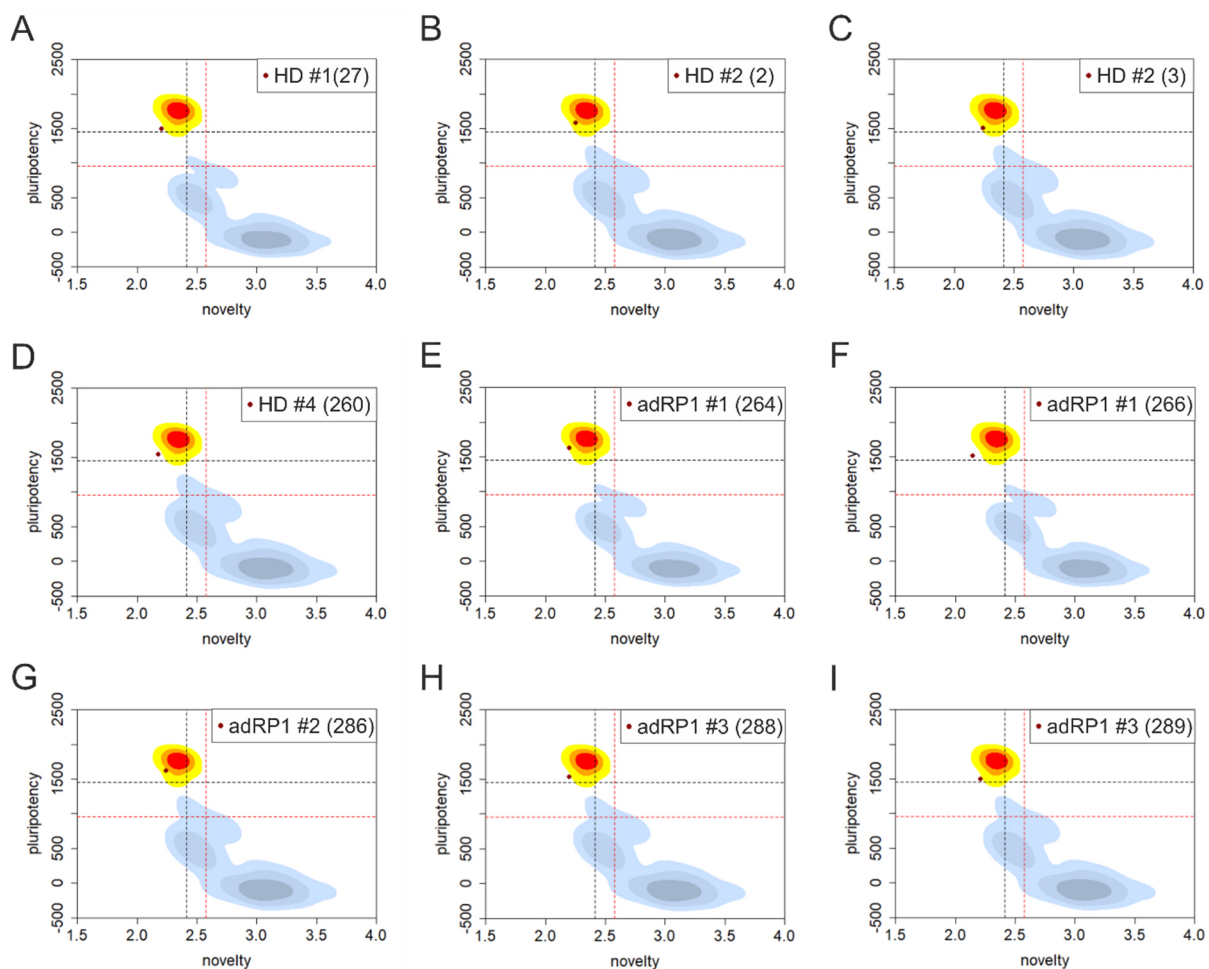
Supplementary Figure 1[8]: PluriTest results from 10 iPSC lines. Scatterplots showing the PluriTest results from the following iPSC lines are shown: (**A**) HD #1 clone 27, (**B**) HD #2 clone 2, (**C**) HD #2 clone 3, (**D**) HD #4 clone 260, (**E**) adRP1 #1 clone 264, (**F**) adRP1 #1 clone 266, (**G**) adRP1 #2 clone 286, (**H**) adRP1 #3 clone 288, (**I**) adRP1 #3 clone 289. The iPSC lines are shown as dark red points. All iPSC lines shown here met the strict empirical thresholds (shown as black dotted lines). Kernel density estimations for embryonic stem cells and nuclear transfer iPSCs (yellow to red) and somatic/differentiated cells (light blue to dark grey) are shown.

---

[8]The PluriTest was executed by Dr. Tanja Rothhammer-Hampl (Department of Neuropathology, Regensburg University Hospital; described in section 5.1.4.)
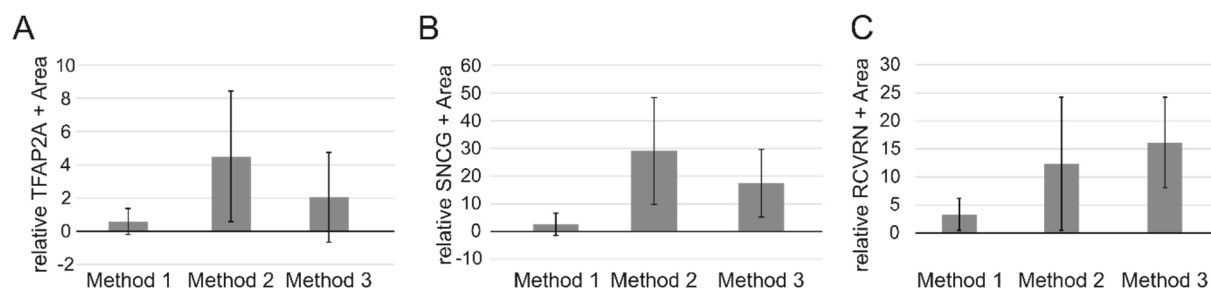
Supplementary Figure 2[9]: Amacrine, ganglion, and marker expression in ROs. The relative area of (**A**) TFAP2A, (**B**) SNCG and (**C**) RCVRN expression were not significantly altered in ROs from either of the three differentiation methods.
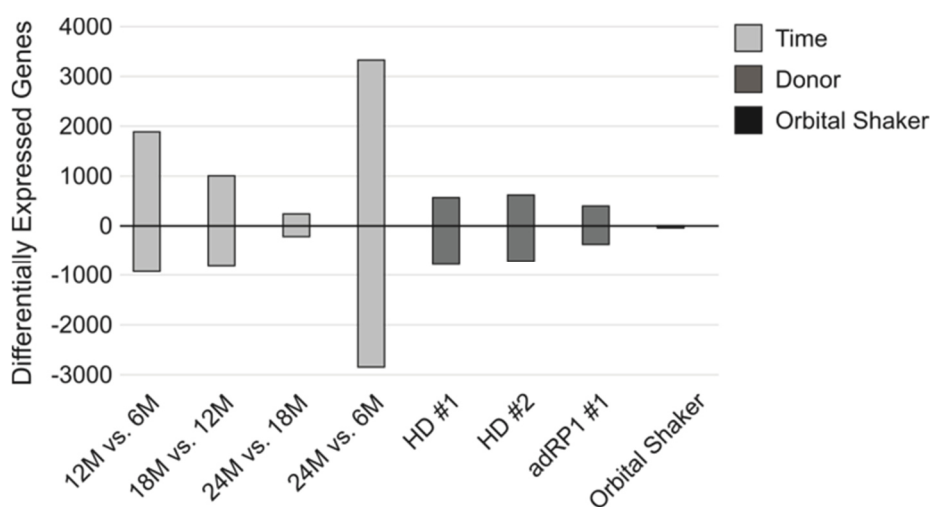
Supplementary Figure 3: DEGs in ROs. The number of up and down-regulated differentially expressed genes are shown for several comparisons. Four comparisons were performed with ROs of different ages: 12 months vs. 6 months, 18 months vs. 12 months, 24 months vs. 18 months, and 12 months vs. 6 months. To characterize the donor effect three comparisons were performed: HD #1 (vs. HD #2 and adRP1 #1), HD #2 (vs. HD #1 and adRP1 #1), and adRP1 #1 (vs. HD #1 and 2). Finally, ROs cultured on an orbital shaker were compared to stationary ROs. Overall, the culture duration had the strongest effect on the mRNA expression, followed by the donor effect. Culture on an orbital shaker did not have a strong influence on the mRNA expression profiles.

---

[9] This figure was modified after Berber et al. (161).
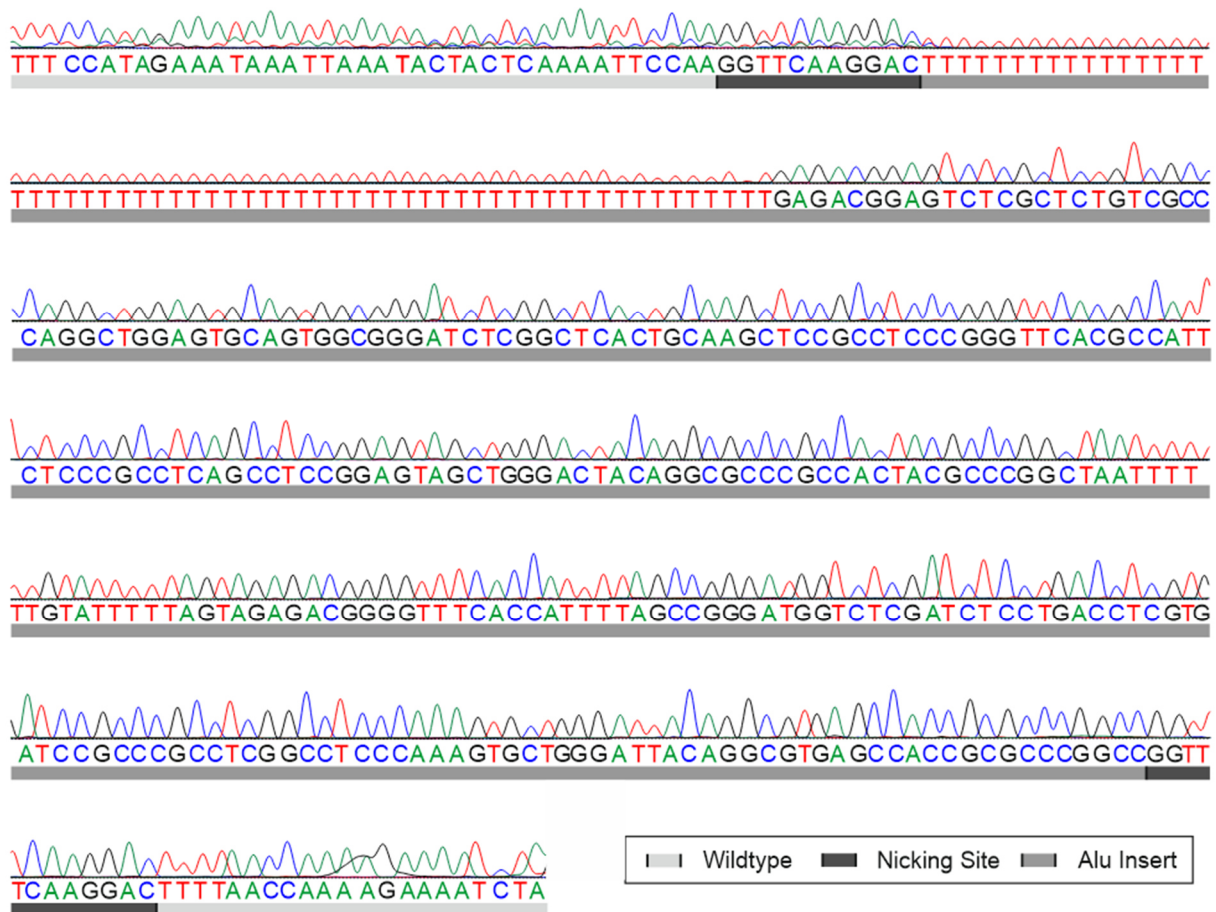
Supplementary Figure 4: adRP1 #2 disease-causing mutation. Sanger sequencing of the mutant allele of cell line adRP1 #2, showing the location of the disease-causing retrotransposon insert (c.2321_2322insAluYa5; medium grey), the duplicated nicking site (dark grey), and the flanking wildtype regions (light grey) are shown. Sequencing was performed with a reverse primer and inverted to show the 5' to 3' sequence.

8.2. Supplementary Methods

The evaluation of raw RNASeq reads was performed based on a pipeline including several programs in a Linux environment. During all steps of the analysis *FastQC* (version 0.11.5) (185) and *MultiQC* (version 1.7.dev0) (186) were used to ensure the correctness of the conducted data processing steps. First, raw reads were trimmed for adapter sequences and low quality (SLIDING WINDOW 4:5; LEADING 5; TRAILING 5; MINLEN 25) using *Trimmomatic* (version 0.39) with the supplied Illumina TruSeq3 sequences (187). Thereafter, the star aligner (version 2.7.1a) (188) was employed with ENCODE standard options to align the trimmed reads to an Ensembl version 97 (GRCh38.p13, including GENCODE version 31) (189) based on the reference genome. The *RSEM* toolbox (version 1.3.1) (190) calculated the estimated gene expression counts, using the standard options paired with two additional

parameters about the fragment length distribution as the data were based on single-end reads (fragment-length-mean 155.9 and fragment-length-sd 56.2). These additional values were obtained by calculating the mean fragment length distribution of 30 samples taken randomly from a dataset about paired-end RNA-seq in retinal tissue as described in (191).

Further quality control and DEG analysis were performed in R (version 4.1.1) (192) using the DESeq2 package (version 1.32.0) (193) based on the estimated counts from RSEM. Only genes that showed at least 10 counts in ten % of the samples were analyzed. The gene count table was further normalized using a variance-stabilizing transformation (VST). A PCA was performed with the help of the *prcomp* function in R to identify and to remove potential outliers. Thereafter, the DESeq2 functions *DESeqDataSetFromMatrix*, *DESeq*, and *results* were applied to identify DEGs in various scenarios. Depending on the research question, the analysis was adjusted for the following covariates: library preparation batch, mobile culture, donor, and RO age. Adjusted p values below a threshold of 0.001 were considered significant. Heatmaps were generated using the function *pheatmap* (version 1.0.12) (194) on the VST normalized data. If necessary, the VST normalized data were scaled beforehand with the help of the *scale* function in the R basic distribution.

8.3. Permission to use Images

Two images shown in this dissertation were modified from images taken by third parties. The permission to use the images was granted by the original authors and/or creators of the images. The images in question are identified in the figure legends, and written permission was granted as follows:

Regensburg, March 9th 2022

I hereby grant Patricia Berber the right to use my image of the Regensburg Cathedral in her dissertation.

_____

Prof Dr. Klaus Stark

UKR
Universitätsklinikum
Regensburg

Regensburg, March 8th 2022

I hereby grant **Patricia Berber** the right to use my brightfield image of induced pluripotent stem cells in her dissertation. The original image is shown in "In-Depth Characterisation of Retinal Pigment Epithelium (RPE) Cells Derived from Human Induced Pluripotent Stem Cells (hiPSC)" Brandl et al. Neuromol Med (2014) DOI 10.1007/s12017-014-8308-8 Figure 1B.

PD Dr. Caroline Brandl

8.4. Original Images

Regensburg, April 29th, 2022

Several original images are shown in this thesis. These images are my work. They were created by myself, during the completion of my doctorate.

Patricia Berber

9.   References

1.   Darwin C. On the Origin of Species by Means of Natural Selection. In: Darwiniana. 1859. p. 7–50.

2.   Flaxman SR, Bourne RRA, Resnikoff S, Ackland P, Braithwaite T, Cicinelli M V., et al. Global causes of blindness and distance vision impairment 1990–2020: a systematic review and meta-analysis. Lancet Glob Heal [Internet]. 2017;5(12):e1221–34. Available from: https://www.sciencedirect.com/science/article/pii/S2214109X17303935?via%3Dihub

3.   Pascolini D, Mariotti SP. Global estimates of visual impairment: 2010. Br J Ophthalmol [Internet]. 2012;96:614–8. Available from: http://bjo.bmj.com/content/early/2011/11/30/bjophthalmol-2011-300539.full.pdf

4.   Ames A, Li Y, Heher E, Kimble C. Energy metabolism of rabbit retina as related to function: high cost of Na+ transport. J Neurosci [Internet]. 1992 Mar 1;12(3):840–53. Available from: https://www.jneurosci.org/lookup/doi/10.1523/JNEUROSCI.12-03-00840.1992

5.   Kühne WF. Zur Photochemie der Netzhaut. Heidelberg: Carl Winter's Universitatsbuchhandlung; 1877.

6.   Gamgee A. Kühne's Researches on Photo-Chemical Processes in the Retina. Nature [Internet]. 1877 Feb;15(379):296–296. Available from: https://www.nature.com/articles/015296a0

7.   Nathans J, Thomas D, Hogness DS. Molecular Genetics of Human Color Vision: The Genes Encoding Blue, Green, and Red Pigments. Science (80-) [Internet]. 1986 Apr 11;232(4747):193–202. Available from: https://www.science.org/doi/10.1126/science.2937147

8.   Dartnall HJA. The interpretation of spectral sensitivity curves. Br Med Bull [Internet]. 1953;9(1):24–30. Available from: https://academic.oup.com/bmb/article-lookup/doi/10.1093/oxfordjournals.bmb.a074302

9.   Deeb SS, Motulsky AG. Molecular genetics of human color vision. Behav Genet [Internet]. 1996 May;26(3):195–207. Available from: http://www.ncbi.nlm.nih.gov/pubmed/8754247

10.   Provencio I, Rodriguez IR, Jiang G, Hayes WP, Moreira EF, Rollag MD. A Novel Human Opsin in the Inner Retina. J Neurosci [Internet]. 2000 Jan 15;20(2):600–5. Available from: https://www.jneurosci.org/lookup/doi/10.1523/JNEUROSCI.20-02-00600.2000

11.   Sernagor E. Retinal Development: Second Sight Comes First. Curr Biol [Internet]. 2005 Jul;15(14):R556–9. Available from: https://linkinghub.elsevier.com/retrieve/pii/S0960982205007165

12.   Berson D. Strange vision: ganglion cells as circadian photoreceptors. Trends Neurosci [Internet]. 2003 Jun;26(6):314–20. Available from: https://linkinghub.elsevier.com/retrieve/pii/S0166223603001309

13.   Strauss O. The Retinal Pigment Epithelium in Visual Function. Physiol Rev

[Internet]. 2005 Jul;85(3):845–81. Available from: http://www.ncbi.nlm.nih.gov/pubmed/15987797

14. WALD G. The Molecular Basis of Visual Excitation. Nature [Internet]. 1968 Aug 24;219(5156):800–7. Available from: https://www.nature.com/articles/219800a0

15. Fulton BS, Rando RR. Biosynthesis of 11-cis-retinoids and retinyl esters by bovine pigment epithelium membranes. Biochemistry [Internet]. 1987 Dec 1;26(24):7938–45. Available from: http://www.ncbi.nlm.nih.gov/pubmed/3427115

16. Quinn PMJ, Wijnholds J. Retinogenesis of the Human Fetal Retina: An Apical Polarity Perspective. Genes (Basel) [Internet]. 2019 Nov 29;10(12):987. Available from: https://www.mdpi.com/2073-4425/10/12/987

17. Wagstaff PE, Heredero Berzal A, Boon CJF, Quinn PMJ, ten Asbroek ALMA, Bergen AA. The Role of Small Molecules and Their Effect on the Molecular Mechanisms of Early Retinal Organoid Development. Int J Mol Sci [Internet]. 2021 Jun 30 [cited 2021 Aug 3];22(13):7081. Available from: https://doi.org/10.3390/ijms22137081

18. Saha M. Spemann Seen through a Lens. In: Gilbert SF, editor. A Conceptual History of Modern Embryology [Internet]. Boston, MA: Springer US; 1991. p. 91–108. Available from: https://doi.org/10.1007/978-1-4615-6823-0_5

19. Ali RR, Sowden JC. DIY eye. Nature [Internet]. 2011 Apr 6;472(7341):42–3. Available from: http://www.nature.com/articles/472042a

20. Spemann H. Uber Korrelationen in die Entwickelung des Auges. Verh Anat Ges [Internet]. 1901 [cited 2022 Mar 3];15:61–79. Available from: http://ci.nii.ac.jp/naid/10012969250/en/

21. NobelPrize.org. The Nobel Prize in Physiology or Medicine 1935 [Internet]. Nobel Prize Outreach AB 2022. 2022. Available from: https://www.nobelprize.org/prizes/medicine/1935/summary/

22. Huang J, Liu Y, Oltean A, Beebe DC. Bmp4 from the optic vesicle specifies murine retina formation. Dev Biol [Internet]. 2015 Jun;402(1):119–26. Available from: http://dx.doi.org/10.1016/j.ydbio.2015.03.006

23. Winnier G, Blessing M, Labosky PA, Hogan BLM. Bone morphogenetic protein-4 is required for mesoderm formation and patterning in the mouse. Genes Dev [Internet]. 1995 Sep 1;9(17):2105–16. Available from: http://genesdev.cshlp.org/lookup/doi/10.1101/gad.9.17.2105

24. Torczynski E. Normal development of the eye and orbit before birth: Development of the eye. Eye Infancy [Internet]. 1989 [cited 2022 Mar 3];9–30. Available from: http://ci.nii.ac.jp/naid/10009735103/en/

25. Berson DM, Dunn FA, Takao M. Phototransduction by Retinal Ganglion Cells That Set the Circadian Clock. Science (80-) [Internet]. 2002 Feb 8;295(5557):1070–3. Available from: https://www.science.org/doi/10.1126/science.1067262

26. Tarttelin EE, Bellingham J, Bibb LC, Foster RG, Hankins MW, Gregory-Evans K, et al. Expression of opsin genes early in ocular development of humans and mice. Exp Eye Res [Internet]. 2003 Mar;76(3):393–6. Available from:

http://www.ncbi.nlm.nih.gov/pubmed/12573668

27. Sekaran S, Lupi D, Jones SL, Sheely CJ, Hattar S, Yau K-W, et al. Melanopsin-Dependent Photoreception Provides Earliest Light Detection in the Mammalian Retina. Curr Biol [Internet]. 2005 Jun;15(12):1099–107. Available from: https://linkinghub.elsevier.com/retrieve/pii/S0960982205005683

28. Dacey DM, Liao H-W, Peterson BB, Robinson FR, Smith VC, Pokorny J, et al. Melanopsin-expressing ganglion cells in primate retina signal colour and irradiance and project to the LGN. Nature [Internet]. 2005 Feb 26;433(7027):749–54. Available from: http://www.nature.com/articles/nature03344

29. Young RW. Cell death during differentiation of the retina in the mouse. J Comp Neurol [Internet]. 1984 Nov 1;229(3):362–73. Available from: https://onlinelibrary.wiley.com/doi/10.1002/cne.902290307

30. Volland S, Esteve-Rudd J, Hoo J, Yee C, Williams DS. A Comparison of Some Organizational Characteristics of the Mouse Central Retina and the Human Macula. Li T, editor. PLoS One [Internet]. 2015 Apr 29;10(4):e0125631. Available from: https://dx.plos.org/10.1371/journal.pone.0125631

31. Murali A, Ramlogan-Steel CA, Andrzejewski S, Steel JC, Layton CJ. Retinal explant culture: A platform to investigate human neuro-retina. Clin Experiment Ophthalmol [Internet]. 2019 Mar 10;47(2):274–85. Available from: https://onlinelibrary.wiley.com/doi/10.1111/ceo.13434

32. Lancaster MA, Knoblich JA. Organogenesis in a dish: Modeling development and disease using organoid technologies. Science (80-) [Internet]. 2014 Jul 18;345(6194). Available from: https://www.science.org/doi/10.1126/science.1247125

33. Eiraku M, Watanabe K, Matsuo-Takasaki M, Kawada M, Yonemura S, Matsumura M, et al. Self-Organized Formation of Polarized Cortical Tissues from ESCs and Its Active Manipulation by Extrinsic Signals. Cell Stem Cell [Internet]. 2008;3(5):519–32. Available from: http://dx.doi.org/10.1016/j.stem.2008.09.002

34. Lancaster MA, Corsini NS, Wolfinger S, Gustafson EH, Phillips AW, Burkard TR, et al. Guided self-organization and cortical plate formation in human brain organoids. Nat Biotechnol. 2017;35(7):659–66.

35. Lancaster MA, Renner M, Martin CA, Wenzel D, Bicknell LS, Hurles ME, et al. Cerebral organoids model human brain development and microcephaly. Nature [Internet]. 2013;501(7467):373–9. Available from: http://dx.doi.org/10.1038/nature12517

36. Velasco S, Kedaigle AJ, Simmons SK, Nash A, Rocha M, Quadrato G, et al. Individual brain organoids reproducibly form cell diversity of the human cerebral cortex. Nature [Internet]. 2019 Jun 5;570(7762):523–7. Available from: http://www.nature.com/articles/s41586-019-1289-x

37. Schwank G, Koo BK, Sasselli V, Dekkers JF, Heo I, Demircan T, et al. Functional repair of CFTR by CRISPR/Cas9 in intestinal stem cell organoids of cystic fibrosis patients. Cell Stem Cell [Internet]. 2013;13(6):653–8. Available from: http://dx.doi.org/10.1016/j.stem.2013.11.002

38. Dekkers JF, Wiegerinck CL, de Jonge HR, Bronsveld I, Janssens HM, de Winter-de Groot KM, et al. A functional CFTR assay using primary cystic fibrosis intestinal organoids. Nat Med [Internet]. 2013 Jul 2;19(7):939–45. Available from: http://www.nature.com/articles/nm.3201

39. Longmire TA, Ikonomou L, Hawkins F, Christodoulou C, Cao Y, Jean JC, et al. Efficient Derivation of Purified Lung and Thyroid Progenitors from Embryonic Stem Cells. Cell Stem Cell [Internet]. 2012 Apr;10(4):398–411. Available from: https://linkinghub.elsevier.com/retrieve/pii/S1934590912000574

40. Wong AP, Bear CE, Chin S, Pasceri P, Thompson TO, Huan L-J, et al. Directed differentiation of human pluripotent stem cells into mature airway epithelia expressing functional CFTR protein. Nat Biotechnol [Internet]. 2012 Sep 26;30(9):876–82. Available from: http://www.nature.com/articles/nbt.2328

41. Low JH, Li P, Chew EGY, Zhou B, Suzuki K, Zhang T, et al. Generation of Human PSC-Derived Kidney Organoids with Patterned Nephron Segments and a De Novo Vascular Network. Cell Stem Cell [Internet]. 2019;25(3):373-387.e9. Available from: https://doi.org/10.1016/j.stem.2019.06.009

42. Watanabe K, Kamiya D, Nishiyama A, Katayama T, Nozaki S, Kawasaki H, et al. Directed differentiation of telencephalic precursors from embryonic stem cells. Nat Neurosci [Internet]. 2005 Mar 6;8(3):288–96. Available from: http://www.nature.com/articles/nn1402

43. Okuda S, Takata N, Hasegawa Y, Kawada M, Inoue Y, Adachi T, et al. Strain-triggered mechanical feedback in self-organizing optic-cup morphogenesis. Sci Adv [Internet]. 2018;1–13. Available from: http://advances.sciencemag.org/cgi/content/short/4/11/eaau1354

44. Eiraku M, Takata N, Ishibashi H, Kawada M, Sakakura E, Okuda S, et al. Self-organizing optic-cup morphogenesis in three-dimensional culture. Nature [Internet]. 2011 Apr 7;472(7341):51–6. Available from: http://www.nature.com/articles/nature09941

45. Wahlin KJ, Maruotti JA, Sripathi SR, Ball J, Angueyra JM, Kim C, et al. Photoreceptor Outer Segment-like Structures in Long-Term 3D Retinas from Human Pluripotent Stem Cells. Sci Rep [Internet]. 2017 Dec 10;7(1):766. Available from: http://www.nature.com/articles/s41598-017-00774-9

46. Li G, Xie B, He L, Zhou T, Gao G, Liu S, et al. Generation of Retinal Organoids with Mature Rods and Cones from Urine-Derived Human Induced Pluripotent Stem Cells. Stem Cells Int [Internet]. 2018 Jun 13;2018:1–12. Available from: https://www.hindawi.com/journals/sci/2018/4968658/

47. Capowski EE, Samimi K, Mayerl SJ, Phillips MJ, Pinilla I, Howden SE, et al. Reproducibility and staging of 3D human retinal organoids across multiple pluripotent stem cell lines. Development [Internet]. 2018 Jan 1;146(1). Available from: http://www.ncbi.nlm.nih.gov/pubmed/30567931

48. Kuwahara A, Ozone C, Nakano T, Saito K, Eiraku M, Sasai Y. Generation of a ciliary margin-like stem cell niche from self-organizing human retinal tissue. Nat Commun [Internet]. 2015 May 19;6(1):6286. Available from: http://dx.doi.org/10.1038/ncomms7286

49. Takahashi K, Yamanaka S. Induction of Pluripotent Stem Cells from Mouse

Embryonic and Adult Fibroblast Cultures by Defined Factors. Cell [Internet]. 2006 Aug;126(4):663–76. Available from: https://linkinghub.elsevier.com/retrieve/pii/S0092867406009767

50. NobelPrize.org. The Nobel Prize in Physiology or Medicine 2012 [Internet]. Nobel Prize Outreach AB 2022. 2022. Available from: https://www.nobelprize.org/prizes/medicine/1935/summary/

51. Gurdon JB. The Developmental Capacity of Nuclei taken from Intestinal Epithelium Cells of Feeding Tadpoles. Development [Internet]. 1962 Dec 1;10(4):622–40. Available from: https://journals.biologists.com/dev/article/10/4/622/35650/The-Developmental-Capacity-of-Nuclei-taken-from

52. Kruczek K, Swaroop A. Pluripotent stem cell-derived retinal organoids for disease modeling and development of therapies. Stem Cells [Internet]. 2020 Oct 1;38(10):1206–15. Available from: https://academic.oup.com/stmcls/article/38/10/1206/6409281

53. Watanabe K, Ueno M, Kamiya D, Nishiyama A, Matsumura M, Wataya T, et al. A ROCK inhibitor permits survival of dissociated human embryonic stem cells. Nat Biotechnol [Internet]. 2007 Jun 27;25(6):681–6. Available from: http://www.nature.com/articles/nbt1310

54. Meyer JS, Shearer RL, Capowski EE, Wright LS, Wallace KA, McMillan EL, et al. Modeling early retinal development with human embryonic and induced pluripotent stem cells. Proc Natl Acad Sci [Internet]. 2009 Sep 29;106(39):16698–703. Available from: https://pnas.org/doi/full/10.1073/pnas.0905245106

55. Kohwi M, Doe CQ. Temporal fate specification and neural progenitor competence during development. Nat Rev Neurosci [Internet]. 2013;14(12):823–38. Available from: https://doi.org/10.1038/nrn3618

56. Hendrickson A, Drucker D. The development of parafoveal and mid-peripheral human retina. Behav Brain Res [Internet]. 1992 Jul 31;49(1):21–31. Available from: http://www.ncbi.nlm.nih.gov/pubmed/1388798

57. Narayanan K, Wadhwa S. Photoreceptor morphogenesis in the human retina: a scanning electron microscopic study. Anat Rec [Internet]. 1998;252(1):133–9. Available from: http://www.ncbi.nlm.nih.gov/pubmed/9737749

58. Edward DP, Kaufman LM. Anatomy, development, and physiology of the visual system. Pediatr Clin North Am [Internet]. 2003 Feb;50(1):1–23. Available from: https://linkinghub.elsevier.com/retrieve/pii/S0031395502001323

59. Zhong X, Gutierrez C, Xue T, Hampton C, Vergara MN, Cao L-H, et al. Generation of three-dimensional retinal tissue with functional photoreceptors from human iPSCs. Nat Commun [Internet]. 2014 Jun 10;5:4047. Available from: http://www.ncbi.nlm.nih.gov/pubmed/24915161

60. O'Hara-Wright M, Gonzalez-Cordero A. Retinal organoids: a window into human retinal development. Development [Internet]. 2020 Dec 24;147(24). Available from: https://journals.biologists.com/dev/article/147/24/dev189746/226019/Retinal-organoids-a-window-into-human-retinal

61. Sridhar A, Hoshino A, Finkbeiner CR, Chitsazan A, Dai L, Haugan AK, et al. Single-Cell Transcriptomic Comparison of Human Fetal Retina, hPSC-Derived Retinal Organoids, and Long-Term Retinal Cultures. Cell Rep [Internet]. 2020 Feb;30(5):1644-1659.e4. Available from: https://doi.org/10.1016/j.celrep.2020.01.007

62. Cowan CS, Renner M, De Gennaro M, Gross-Scherf B, Goldblum D, Hou Y, et al. Cell Types of the Human Retina and Its Organoids at Single-Cell Resolution. Cell [Internet]. 2020 Sep;182(6):1623-1640.e34. Available from: https://linkinghub.elsevier.com/retrieve/pii/S0092867420310047

63. Boughman JA, Conneally PM, Nance WE. Population genetic studies of retinitis pigmentosa. Am J Hum Genet [Internet]. 1980 Mar;32(2):223–35. Available from: http://www.ncbi.nlm.nih.gov/pubmed/7386458

64. Galan A, Chizzolini M, Milan E, Sebastiani A, Costagliola C, Parmeggiani F. Good Epidemiologic Practice in Retinitis Pigmentosa: From Phenotyping to Biobanking. Curr Genomics [Internet]. 2011 Jun 1;12(4):260–6. Available from: http://www.eurekaselect.com/openurl/content.php?genre=article&issn=1389-2029&volume=12&issue=4&spage=260

65. Tsang SH, Sharma T. Atlas of Inherited Retinal Diseases [Internet]. Tsang SH, Sharma T, editors. Advances in Experimental Medicine and Biology. Cham: Springer International Publishing; 2018. 49–55 p. (Advances in Experimental Medicine and Biology; vol. 1085). Available from: http://link.springer.com/10.1007/978-3-319-95046-4

66. Fahim A. Retinitis pigmentosa: recent advances and future directions in diagnosis and management. Curr Opin Pediatr [Internet]. 2018 Dec;30(6):725–33. Available from: http://journals.lww.com/00008480-201812000-00006

67. Ran X, Cai W-J, Huang X-F, Liu Q, Lu F, Qu J, et al. "RetinoGenetics": a comprehensive mutation database for genes related to inherited retinal degeneration. Database [Internet]. 2014 Jun 17;2014:bau047–bau047. Available from: https://academic.oup.com/database/article-lookup/doi/10.1093/database/bau047

68. Huang X-F, Huang F, Wu K-C, Wu J, Chen J, Pang C-P, et al. Genotype–phenotype correlation and mutation spectrum in a large cohort of patients with inherited retinal dystrophy revealed by next-generation sequencing. Genet Med [Internet]. 2015 Apr;17(4):271–8. Available from: https://linkinghub.elsevier.com/retrieve/pii/S1098360021031889

69. Fahim AT, Daiger SP WR. Nonsyndromic Retinitis Pigmentosa Overview [Internet]. GeneReviews®. 2000. Available from: https://www.ncbi.nlm.nih.gov/books/NBK1417/

70. Hamel C. Retinitis pigmentosa. Orphanet J Rare Dis [Internet]. 2006 Dec 11;1(1):40. Available from: https://ojrd.biomedcentral.com/articles/10.1186/1750-1172-1-40

71. Hartong DT, Berson EL, Dryja TP. Retinitis pigmentosa. Lancet [Internet]. 2006 Nov;368(9549):1795–809. Available from: https://linkinghub.elsevier.com/retrieve/pii/S0140673606697407

72. Mansergh FC, Millington-Ward S, Kennan A, Kiang AS, Humphries M, Farrar

GJ, et al. Retinitis pigmentosa and progressive sensorineural hearing loss caused by a C12258A mutation in the mitochondrial MTTS2 gene. Am J Hum Genet [Internet]. 1999 Apr;64(4):971–85. Available from: http://www.ncbi.nlm.nih.gov/pubmed/10090882

73. Jauregui R, Takahashi VKL, Park KS, Cui X, Takiuti JT, Lima de Carvalho JR, et al. Multimodal structural disease progression of retinitis pigmentosa according to mode of inheritance. Sci Rep [Internet]. 2019;9(1):10712. Available from: http://www.nature.com/articles/s41598-019-47251-z

74. Deng W-L, Gao M-L, Lei X-L, Lv J-N, Zhao H, He K-W, et al. Gene Correction Reverses Ciliopathy and Photoreceptor Loss in iPSC-Derived Retinal Organoids from Retinitis Pigmentosa Patients. Stem Cell Reports [Internet]. 2018 Apr;10(4):1267–81. Available from: https://doi.org/10.1016/j.stemcr.2018.02.003

75. Kruczek K, Qu Z, Gentry J, Fadl BR, Gieser L, Hiriyanna S, et al. Gene Therapy of Dominant CRX-Leber Congenital Amaurosis using Patient Stem Cell-Derived Retinal Organoids. Stem Cell Reports [Internet]. 2021 Feb;16(2):252–63. Available from: http://dx.doi.org/10.1016/j.stemcr.2020.12.018

76. Lukovic D, Artero Castro A, Kaya KD, Munezero D, Gieser L, Davó-Martínez C, et al. Retinal Organoids derived from hiPSCs of an AIPL1-LCA Patient Maintain Cytoarchitecture despite Reduced levels of Mutant AIPL1. Sci Rep [Internet]. 2020 Dec 25;10(1):5426. Available from: http://www.nature.com/articles/s41598-020-62047-2

77. Jin Z-B, Okamoto S, Osakada F, Homma K, Assawachananont J, Hirami Y, et al. Modeling Retinal Degeneration Using Patient-Specific Induced Pluripotent Stem Cells. Mattson M, editor. PLoS One [Internet]. 2011 Feb 10;6(2):e17084. Available from: https://dx.plos.org/10.1371/journal.pone.0017084

78. Martin-Merida I, Aguilera-Garcia D, Jose PF-S, Blanco-Kelly F, Zurita O, Almoguera B, et al. Toward the Mutational Landscape of Autosomal Dominant Retinitis Pigmentosa: A Comprehensive Analysis of 258 Spanish Families. Investig Opthalmology Vis Sci [Internet]. 2018 May 7;59(6):2345. Available from: http://iovs.arvojournals.org/article.aspx?doi=10.1167/iovs.18-23854

79. Van Cauwenbergh C, Coppieters F, Roels D, De Jaegere S, Flipts H, De Zaeytijd J, et al. Mutations in Splicing Factor Genes Are a Major Cause of Autosomal Dominant Retinitis Pigmentosa in Belgian Families. Lewin AS, editor. PLoS One [Internet]. 2017 Jan 11;12(1):e0170038. Available from: https://dx.plos.org/10.1371/journal.pone.0170038

80. Payne A, Vithana E, Khaliq S, Hameed A, Deller J, Abu-Safieh L, et al. RP1 protein truncating mutations predominate at the RP1 adRP locus. Invest Ophthalmol Vis Sci [Internet]. 2000 Dec;41(13):4069–73. Available from: http://www.ncbi.nlm.nih.gov/pubmed/11095597

81. Pierce EA, Quinn T, Meehan T, McGee TL, Berson EL, Dryja TP. Mutations in a gene encoding a new oxygen-regulated photoreceptor protein cause dominant retinitis pigmentosa. Nat Genet [Internet]. 1999 Jul;22(3):248–54. Available from: https://www.nature.com/articles/ng0799_248

82. Siemiatkowska AM, Astuti GDN, Arimadyo K, den Hollander AI, Faradz SMH,

Cremers FPM, et al. Identification of a novel nonsense mutation in RP1 that causes autosomal recessive retinitis pigmentosa in an Indonesian family. Mol Vis [Internet]. 2012;18(October):2411–9. Available from: http://www.ncbi.nlm.nih.gov/pubmed/23077400

83. Zhang J, Sun X, Qian Y, LaDuca JP, Maquat LE. At least one intron is required for the nonsense-mediated decay of triosephosphate isomerase mRNA: a possible link between nuclear splicing and cytoplasmic translation. Mol Cell Biol [Internet]. 1998 Sep;18(9):5272–83. Available from: https://journals.asm.org/doi/10.1128/MCB.18.9.5272

84. Verbakel SK, van Huet RAC, den Hollander AI, Geerlings MJ, Kersten E, Klevering BJ, et al. Macular Dystrophy and Cone-Rod Dystrophy Caused by Mutations in the RP1 Gene: Extending the RP1 Disease Spectrum. Invest Ophthalmol Vis Sci [Internet]. 2019 Mar 1;60(4):1192–203. Available from: http://iovs.arvojournals.org/article.aspx?doi=10.1167/iovs.18-26084

85. Chassine T, Bocquet B, Daien V, Avila-Fernandez A, Ayuso C, Collin RWJ, et al. Autosomal recessive retinitis pigmentosa with RP1 mutations is associated with myopia. Br J Ophthalmol [Internet]. 2015 Oct;99(10):1360–5. Available from: https://bjo.bmj.com/lookup/doi/10.1136/bjophthalmol-2014-306224

86. Liu Q, Zhou J, Daiger SP, Farber DB, Heckenlively JR, Smith JE, et al. Identification and subcellular localization of the RP1 protein in human and mouse photoreceptors. Invest Ophthalmol Vis Sci [Internet]. 2002 Jan;43(1):22–32. Available from: http://www.ncbi.nlm.nih.gov/pubmed/11773008

87. Liu Q, Zuo J, Pierce EA. The retinitis pigmentosa 1 protein is a photoreceptor microtubule-associated protein. J Neurosci [Internet]. 2004 Jul 21;24(29):6427–36. Available from: http://www.ncbi.nlm.nih.gov/pubmed/15269252

88. Liu Q, Lyubarsky A, Skalet JH, Pugh EN, Pierce EA. RP1 is required for the correct stacking of outer segment discs. Investig Ophthalmol Vis Sci [Internet]. 2003 Oct 1;44(10):4171–83. Available from: http://iovs.arvojournals.org/article.aspx?doi=10.1167/iovs.03-0410

89. Gao J, Cheon K, Nusinowitz S, Liu Q, Bei D, Atkins K, et al. Progressive photoreceptor degeneration, outer segment dysplasia, and rhodopsin mislocalization in mice with targeted disruption of the retinitis pigmentosa-1 (Rp1) gene. Proc Natl Acad Sci [Internet]. 2002;99(8):5698–703. Available from: http://www.pnas.org/cgi/doi/10.1073/pnas.042122399

90. Liu Q, Collin RWJ, Cremers FPM, den Hollander AI, van den Born LI, Pierce EA. Expression of Wild-Type Rp1 Protein in Rp1 Knock-in Mice Rescues the Retinal Degeneration Phenotype. Janecke AR, editor. PLoS One [Internet]. 2012 Aug 21;7(8):e43251. Available from: https://dx.plos.org/10.1371/journal.pone.0043251

91. Ovando-Roche P, West EL, Branch MJ, Sampson RD, Fernando M, Munro P, et al. Use of bioreactors for culturing human retinal organoids improves photoreceptor yields. Stem Cell Res Ther [Internet]. 2018 Dec 13;9(1):156. Available from: https://stemcellres.biomedcentral.com/articles/10.1186/s13287-018-0907-0

92. DiStefano T, Chen HY, Panebianco C, Kaya KD, Brooks MJ, Gieser L, et al.

Accelerated and Improved Differentiation of Retinal Organoids from Pluripotent Stem Cells in Rotating-Wall Vessel Bioreactors. Stem Cell Reports [Internet]. 2018 Jan;10(1):300–13. Available from: https://doi.org/10.1016/j.stemcr.2017.11.001

93. Biasella F, Plössl K, Karl C, Weber BHF, Friedrich U. Altered Protein Function Caused by AMD-associated Variant rs704 Links Vitronectin to Disease Pathology. Investig Opthalmology Vis Sci [Internet]. 2020 Dec 1;61(14):2. Available from: https://iovs.arvojournals.org/article.aspx?articleid=2772015

94. Brandl C, Zimmermann SJ, Milenkovic VM, Rosendahl SMG, Grassmann F, Milenkovic A, et al. In-Depth Characterisation of Retinal Pigment Epithelium (RPE) Cells Derived from Human Induced Pluripotent Stem Cells (hiPSC). NeuroMolecular Med [Internet]. 2014;16(3):551–64. Available from: http://link.springer.com/10.1007/s12017-014-8308-8

95. Nachtigal A-L, Milenkovic A, Brandl C, Schulz HL, Duerr LMJ, Lang GE, et al. Mutation-Dependent Pathomechanisms Determine the Phenotype in the Bestrophinopathies. Int J Mol Sci [Internet]. 2020 Feb 26;21(5):1597. Available from: https://www.mdpi.com/1422-0067/21/5/1597

96. Okita K, Yamakawa T, Matsumura Y, Sato Y, Amano N, Watanabe A, et al. An Efficient Nonviral Method to Generate Integration-Free Human-Induced Pluripotent Stem Cells from Cord Blood and Peripheral Blood Cells. Stem Cells [Internet]. 2013 Mar 1;31(3):458–66. Available from: http://www.ncbi.nlm.nih.gov/pubmed/23193063

97. Müller F-J, Schuldt BM, Williams R, Mason D, Altun G, Papapetrou EP, et al. A bioinformatic assay for pluripotency in human cells. Nat Methods [Internet]. 2011 Apr 6;8(4):315–7. Available from: http://www.nature.com/articles/nmeth.1580

98. Schulze M, Hoja S, Winner B, Winkler J, Edenhofer F, Riemenschneider MJ. Model Testing of PluriTest with Next-Generation Sequencing Data. Stem Cells Dev [Internet]. 2016 Apr 1;25(7):569–71. Available from: https://www.liebertpub.com/doi/10.1089/scd.2015.0266

99. Hallam D, Hilgen G, Dorgau B, Zhu L, Yu M, Bojic S, et al. Human-Induced Pluripotent Stem Cells Generate Light Responsive Retinal Organoids with Variable and Nutrient-Dependent Efficiency. Stem Cells [Internet]. 2018 Oct 1;36(10):1535–51. Available from: https://academic.oup.com/stmcls/article/36/10/1535/6423915

100. Huang L-K, Wang M-JJ. Image thresholding by minimizing the measures of fuzziness. Pattern Recognit [Internet]. 1995 Jan;28(1):41–51. Available from: https://doi.org/10.1016/0031-3203(94)E0043-K

101. Schindelin J, Arganda-Carreras I, Frise E, Kaynig V, Longair M, Pietzsch T, et al. Fiji: an open-source platform for biological-image analysis. Nat Methods [Internet]. 2012;9(7):676–82. Available from: https://doi.org/10.1038/nmeth.2019

102. Massey FJ. The Kolmogorov-Smirnov Test for Goodness of Fit. J Am Stat Assoc [Internet]. 1951 Mar 1;46(253):68–78. Available from: https://www.tandfonline.com/doi/abs/10.1080/01621459.1951.10500769

103. Fisher RA. Statistical Methods for Research Workers. In: Kotz S, Johnson NL, editors. New York, NY: Springer New York; 1992. p. 66–70. Available from:

https://doi.org/10.1007/978-1-4612-4380-9_6

104. Bonferroni C. Teoria statistica delle classi e calcolo delle probabilita. Pubbl del R Ist Super di Sci Econ e Commericiali di Firenze. 1936;8:3–62.

105. Livak KJ, Schmittgen TD. Analysis of Relative Gene Expression Data Using Real-Time Quantitative PCR and the 2−ΔΔCT Method. Methods [Internet]. 2001 Dec;25(4):402–8. Available from: https://linkinghub.elsevier.com/retrieve/pii/S1046202301912629

106. Raudvere U, Kolberg L, Kuzmin I, Arak T, Adler P, Peterson H, et al. g:Profiler: a web server for functional enrichment analysis and conversions of gene lists (2019 update). Nucleic Acids Res [Internet]. 2019 Jul 2;47(W1):W191–8. Available from: https://academic.oup.com/nar/article/47/W1/W191/5486750

107. Hoshino A, Ratnapriya R, Brooks MJ, Chaitankar V, Wilken MS, Zhang C, et al. Molecular Anatomy of the Developing Human Retina. Dev Cell [Internet]. 2017 Dec;43(6):763-779.e4. Available from: https://linkinghub.elsevier.com/retrieve/pii/S1534580717308730

108. Collin J, Queen R, Zerti D, Dorgau B, Hussain R, Coxhead J, et al. Deconstructing Retinal Organoids: Single Cell RNA-Seq Reveals the Cellular Components of Human Pluripotent Stem Cell-Derived Retina. Stem Cells [Internet]. 2019 May 1;37(5):593–8. Available from: https://stemcellsjournals.onlinelibrary.wiley.com/doi/abs/10.1002/stem.2963?af=R

109. Knut and Alice Walberg Foundation. proteinatlas.org [Internet]. 2019. Available from: proteinatlas.org

110. Uhlén M, Fagerberg L, Hallström BM, Lindskog C, Oksvold P, Mardinoglu A, et al. Tissue-based map of the human proteome. Science (80-) [Internet]. 2015 Jan 23;347(6220). Available from: https://www.science.org/doi/10.1126/science.1260419

111. Thul PJ, Åkesson L, Wiking M, Mahdessian D, Geladaki A, Ait Blal H, et al. A subcellular map of the human proteome. Science (80-) [Internet]. 2017 May 26;356(6340). Available from: https://www.science.org/doi/10.1126/science.aal3321

112. Achberger K, Probst C, Haderspeck J, Bolz S, Rogal J, Chuchuy J, et al. Merging organoid and organ-on-a-chip technology to generate complex multi-layer tissue models in a human Retina-on-a-Chip platform. Elife [Internet]. 2019;8. Available from: https://elifesciences.org/articles/46188

113. Yanai A, Laver CRJ, Gregory-Evans CY, Liu RR, Gregory-Evans K. Enhanced Functional Integration of Human Photoreceptor Precursors into Human and Rodent Retina in an Ex Vivo Retinal Explant Model System. Tissue Eng Part A [Internet]. 2015 Jun;21(11–12):1763–71. Available from: https://www.liebertpub.com/doi/10.1089/ten.tea.2014.0669

114. Bagley JA, Reumann D, Bian S, Lévi-Strauss J, Knoblich JA. Fused cerebral organoids model interactions between brain regions. Nat Methods [Internet]. 2017 Jul 1;14(7):743–51. Available from: http://www.nature.com/articles/nmeth.4304

115. www.benchling.com/ [Internet]. 2019. Available from: www.benchling.com/

116. Mashiko D, Fujihara Y, Satouh Y, Miyata H, Isotani A, Ikawa M. Generation of mutant mice by pronuclear injection of circular plasmid expressing Cas9 and single guided RNA. Sci Rep [Internet]. 2013 Dec 27;3(1):3355. Available from: http://www.nature.com/articles/srep03355

117. Lukowski SW, Lo CY, Sharov AA, Nguyen Q, Fang L, Hung SS, et al. A single-cell transcriptome atlas of the adult human retina. EMBO J [Internet]. 2019;1–15. Available from: https://onlinelibrary.wiley.com/doi/abs/10.15252/embj.2018100811

118. Soto I, Oglesby E, Buckingham BP, Son JL, Roberson EDO, Steele MR, et al. Retinal Ganglion Cells Downregulate Gene Expression and Lose Their Axons within the Optic Nerve Head in a Mouse Glaucoma Model. J Neurosci [Internet]. 2008 Jan 9;28(2):548–61. Available from: https://www.jneurosci.org/lookup/doi/10.1523/JNEUROSCI.3714-07.2008

119. Yan X-X, Wiechmann AF. Early expression of recoverin in a unique population of neurons in the human retina. Anat Embryol (Berl) [Internet]. 1996 Dec 16;195(1):51–63. Available from: http://link.springer.com/10.1007/s004290050024

120. Chen S, Wang Q-L, Nie Z, Sun H, Lennon G, Copeland NG, et al. Crx, a Novel Otx-like Paired-Homeodomain Protein, Binds to and Transactivates Photoreceptor Cell-Specific Genes. Neuron [Internet]. 1997 Nov 1 [cited 2021 May 19];19(5):1017–30. Available from: https://linkinghub.elsevier.com/retrieve/pii/S0896627300803943

121. Furukawa T, Morrow EM, Cepko CL. Crx, a Novel otx-like Homeobox Gene, Shows Photoreceptor-Specific Expression and Regulates Photoreceptor Differentiation. Cell [Internet]. 1997 Nov 14 [cited 2021 May 19];91(4):531–41. Available from: https://linkinghub.elsevier.com/retrieve/pii/S0092867400804390

122. Gonzalez-Cordero A, Kruczek K, Naeem A, Fernando M, Kloc M, Ribeiro J, et al. Recapitulation of Human Retinal Development from Human Pluripotent Stem Cells Generates Transplantable Populations of Cone Photoreceptors. Stem Cell Reports [Internet]. 2017;9(3):820–37. Available from: http://dx.doi.org/10.1016/j.stemcr.2017.07.022

123. Muranishi Y, Sato S, Inoue T, Ueno S, Koyasu T, Kondo M, et al. Gene expression analysis of embryonic photoreceptor precursor cells using BAC-Crx-EGFP transgenic mouse. Biochem Biophys Res Commun [Internet]. 2010 Feb 12 [cited 2021 May 12];392(3):317–22. Available from: https://linkinghub.elsevier.com/retrieve/pii/S0006291X1000029X

124. Xiang M, Zhou L, Macke J, Yoshioka T, Hendry S, Eddy R, et al. The Brn-3 family of POU-domain factors: primary structure, binding specificity, and expression in subsets of retinal ganglion cells and somatosensory neurons. J Neurosci [Internet]. 1995 Jul 1;15(7):4762–85. Available from: https://www.jneurosci.org/lookup/doi/10.1523/JNEUROSCI.15-07-04762.1995

125. Sajgo S, Ghinia MG, Brooks M, Kretschmer F, Chuang K, Hiriyanna S, et al. Molecular codes for cell type specification in Brn3 retinal ganglion cells. Proc Natl Acad Sci [Internet]. 2017 May 16;114(20):E3974–83. Available from:

https://pnas.org/doi/full/10.1073/pnas.1618551114

126. Luo Z, Xu C, Li K, Xian B, Liu Y, Li K, et al. Islet1 and Brn3 Expression Pattern Study in Human Retina and hiPSC-Derived Retinal Organoid. Stem Cells Int [Internet]. 2019 Dec 10;2019:1–14. Available from: https://www.hindawi.com/journals/sci/2019/8786396/

127. Marmorstein AD, Marmorstein LY, Rayborn M, Wang X, Hollyfield JG, Petrukhin K. Bestrophin, the product of the Best vitelliform macular dystrophy gene (VMD2), localizes to the basolateral plasma membrane of the retinal pigment epithelium. Proc Natl Acad Sci [Internet]. 2000 Nov 7;97(23):12758–63. Available from: https://pnas.org/doi/full/10.1073/pnas.220402097

128. Stevenson BR, Siliciano JD, Mooseker MS, Goodenough DA. Identification of ZO-1: a high molecular weight polypeptide associated with the tight junction (zonula occludens) in a variety of epithelia. J Cell Biol [Internet]. 1986 Sep 1;103(3):755–66. Available from: https://rupress.org/jcb/article/103/3/755/13454/Identification-of-ZO1-a-high-molecular-weight

129. Georgiadis A, Tschernutter M, Bainbridge JWB, Balaggan KS, Mowat F, West EL, et al. The Tight Junction Associated Signalling Proteins ZO-1 and ZONAB Regulate Retinal Pigment Epithelium Homeostasis in Mice. Klymkowsky M, editor. PLoS One [Internet]. 2010 Dec 30;5(12):e15730. Available from: https://dx.plos.org/10.1371/journal.pone.0015730

130. Gordon A, Yoon S-J, Tran SS, Makinson CD, Park JY, Andersen J, et al. Long-term maturation of human cortical organoids matches key early postnatal transitions. Nat Neurosci [Internet]. 2021 Mar 22;24(3):331–42. Available from: http://dx.doi.org/10.1038/s41593-021-00802-y

131. Berson EL, Grimsby JL, Adams SM, McGee TL, Sweklo E, Pierce EA, et al. Clinical features and mutations in patients with dominant retinitis pigmentosa-1 (RP1). Invest Ophthalmol Vis Sci [Internet]. 2001 Sep;42(10):2217–24. Available from: http://www.ncbi.nlm.nih.gov/pubmed/11527933

132. Qian X, Nguyen HN, Song MM, Hadiono C, Ogden SC, Hammack C, et al. Brain-Region-Specific Organoids Using Mini-bioreactors for Modeling ZIKV Exposure. Cell [Internet]. 2016 May;165(5):1238–54. Available from: https://linkinghub.elsevier.com/retrieve/pii/S0092867416304676

133. Tanaka Y, Cakir B, Xiang Y, Sullivan GJ, Park I-H. Synthetic Analyses of Single-Cell Transcriptomes from Multiple Brain Organoids and Fetal Brain. Cell Rep [Internet]. 2020 Feb;30(6):1682-1689.e3. Available from: https://linkinghub.elsevier.com/retrieve/pii/S221112472030053X

134. Ormel PR, Vieira de Sá R, van Bodegraven EJ, Karst H, Harschnitz O, Sneeboer MAM, et al. Microglia innately develop within cerebral organoids. Nat Commun [Internet]. 2018 Dec 9;9(1):4167. Available from: http://dx.doi.org/10.1038/s41467-018-06684-2

135. Clarke DD SL. Circulation and Energy Metabolism of the Brain. In: Basic Neurochemistry: Molecular, Cellular and Medical Aspects [Internet]. 6th ed. 1999. Available from: https://www.ncbi.nlm.nih.gov/books/NBK20413/

136. Wong-Riley M. Energy metabolism of the visual system. Eye Brain [Internet].

2010 Jul;99. Available from: http://www.dovepress.com/energy-metabolism-of-the-visual-system-peer-reviewed-article-EB

137. Raichle ME, Gusnard DA. Appraising the brain's energy budget. Proc Natl Acad Sci U S A [Internet]. 2002 Aug 6;99(16):10237–9. Available from: https://pnas.org/doi/full/10.1073/pnas.172399499

138. Eremeev A V., Volovikov EA, Shuvalova LD, Davidenko A V., Khomyakova EA, Bogomiakova ME, et al. "Necessity Is the Mother of Invention" or Inexpensive, Reliable, and Reproducible Protocol for Generating Organoids. Biochem [Internet]. 2019 Mar 27;84(3):321–8. Available from: http://link.springer.com/10.1134/S0006297919030143

139. Chichagova V, Hilgen G, Ghareeb A, Georgiou M, Carter M, Sernagor E, et al. Human iPSC differentiation to retinal organoids in response to IGF1 and BMP4 activation is line- and method-dependent. Stem Cells [Internet]. 2020 Feb 1;38(2):195–201. Available from: https://academic.oup.com/stmcls/article/38/2/195/6409346

140. Mellough CB, Collin J, Queen R, Hilgen G, Dorgau B, Zerti D, et al. Systematic Comparison of Retinal Organoid Differentiation from Human Pluripotent Stem Cells Reveals Stage Specific, Cell Line, and Methodological Differences. Stem Cells Transl Med [Internet]. 2019 Jul 1;8(7):694–706. Available from: https://academic.oup.com/stcltm/article/8/7/694/6403767

141. Lane A, Jovanovic K, Shortall C, Ottaviani D, Panes AB, Schwarz N, et al. Modeling and Rescue of RP2 Retinitis Pigmentosa Using iPSC-Derived Retinal Organoids. Stem Cell Reports [Internet]. 2020 Jul 14;15(1):67–79. Available from: https://doi.org/10.1016/j.stemcr.2020.05.007

142. Gao M-L, Lei X-L, Han F, He K-W, Jin S-Q, Zhang Y-Y, et al. Patient-Specific Retinal Organoids Recapitulate Disease Features of Late-Onset Retinitis Pigmentosa. Front Cell Dev Biol [Internet]. 2020 Mar 6;8(March):1–14. Available from: https://www.frontiersin.org/article/10.3389/fcell.2020.00128/full

143. Quinn PM, Buck TM, Mulder AA, Ohonin C, Alves CH, Vos RM, et al. Human iPSC-Derived Retinas Recapitulate the Fetal CRB1 CRB2 Complex Formation and Demonstrate that Photoreceptors and Müller Glia Are Targets of AAV5. Stem Cell Reports [Internet]. 2019 May;12(5):906–19. Available from: https://linkinghub.elsevier.com/retrieve/pii/S2213671119300876

144. Jerber J, Seaton DD, Cuomo ASE, Kumasaka N, Haldane J, Steer J, et al. Population-scale single-cell RNA-seq profiling across dopaminergic neuron differentiation. Nat Genet [Internet]. 2021 Mar 4;53(3):304–12. Available from: https://doi.org/10.1038/s41588-021-00801-6

145. Ovando-Roche P, Georgiadis A, Smith AJ, Pearson RA, Ali RR. Harnessing the Potential of Human Pluripotent Stem Cells and Gene Editing for the Treatment of Retinal Degeneration. Curr Stem Cell Reports [Internet]. 2017 Jun 18;3(2):112–23. Available from: http://link.springer.com/10.1007/s40778-017-0078-4

146. Gaspard N, Bouschet T, Hourez R, Dimidschstein J, Naeije G, van den Ameele J, et al. An intrinsic mechanism of corticogenesis from embryonic stem cells. Nature [Internet]. 2008 Sep 17;455(7211):351–7. Available from:

http://www.nature.com/articles/nature07287

147. Au E, Fishell G. Cortex Shatters the Glass Ceiling. Cell Stem Cell [Internet]. 2008 Nov;3(5):472–4. Available from: http://dx.doi.org/10.1016/j.stem.2008.10.013

148. Camp JG, Badsha F, Florio M, Kanton S, Gerber T, Wilsch-Bräuninger M, et al. Human cerebral organoids recapitulate gene expression programs of fetal neocortex development. Proc Natl Acad Sci [Internet]. 2015 Dec 22;112(51):15672–7. Available from: https://pnas.org/doi/full/10.1073/pnas.1520760112

149. Quadrato G, Nguyen T, Macosko EZ, Sherwood JL, Min Yang S, Berger DR, et al. Cell diversity and network dynamics in photosensitive human brain organoids. Nature [Internet]. 2017 May 4;545(7652):48–53. Available from: http://www.nature.com/articles/nature22047

150. Yoon S-J, Elahi LS, Paşca AM, Marton RM, Gordon A, Revah O, et al. Reliability of human cortical organoid generation. Nat Methods [Internet]. 2019 Jan 20;16(1):75–8. Available from: http://dx.doi.org/10.1038/s41592-018-0255-0

151. Quadrato G, Brown J, Arlotta P. The promises and challenges of human brain organoids as models of neuropsychiatric disease. Nat Med [Internet]. 2016 Nov 26;22(11):1220–8. Available from: http://www.nature.com/articles/nm.4214

152. Christova P, Joseph J, Georgopoulos AP. Human Connectome Project: heritability of brain volumes in young healthy adults. Exp Brain Res [Internet]. 2021 Apr 21;239(4):1273–86. Available from: https://link.springer.com/10.1007/s00221-021-06057-0

153. Bartley A. Genetic variability of human brain size and cortical gyral patterns. Brain [Internet]. 1997 Feb 1;120(2):257–69. Available from: https://academic.oup.com/brain/article-lookup/doi/10.1093/brain/120.2.257

154. Bekerman I, Gottlieb P, Vaiman M. Variations in eyeball diameters of the healthy adults. J Ophthalmol [Internet]. 2014;2014:503645. Available from: http://www.ncbi.nlm.nih.gov/pubmed/25431659

155. Klein AP. Heritability Analysis of Spherical Equivalent, Axial Length, Corneal Curvature, and Anterior Chamber Depth in the Beaver Dam Eye Study. Arch Ophthalmol [Internet]. 2009 May 11;127(5):649. Available from: http://archopht.jamanetwork.com/article.aspx?doi=10.1001/archophthalmol.2009.61

156. Ding X, Wang D, Huang Q, Zhang J, Chang J, He M. Distribution and Heritability of Peripheral Eye Length in Chinese Children and Adolescents: The Guangzhou Twin Eye Study. Investig Opthalmology Vis Sci [Internet]. 2013 Feb 5;54(2):1048. Available from: http://iovs.arvojournals.org/article.aspx?doi=10.1167/iovs.12-10066

157. Pierce GB, Verney EL. An in vitro and in vivo study of differentiation in teratocarcinomas. Cancer [Internet]. 1961 Sep;14(5):1017–29. Available from: http://www.ncbi.nlm.nih.gov/pubmed/13735537

158. Bernard AB, Lin CC, Anseth KS. A Microwell cell culture platform for the aggregation of pancreatic β-cells. Tissue Eng - Part C Methods [Internet]. 2012 Aug;18(8):583–92. Available from:

https://www.liebertpub.com/doi/10.1089/ten.tec.2011.0504

159. Decembrini S, Hoehnel S, Brandenberg N, Arsenijevic Y, Lutolf MP. Hydrogel-based milliwell arrays for standardized and scalable retinal organoid cultures. Sci Rep [Internet]. 2020 Dec 24;10(1):10275. Available from: http://dx.doi.org/10.1038/s41598-020-67012-7

160. Artero Castro A, Rodríguez Jimenez FJ, Jendelova P, Erceg S. Deciphering Retinal Diseases through the Generation of Three Dimensional Stem Cell-derived Organoids. Stem Cells [Internet]. 2019; Available from: http://www.ncbi.nlm.nih.gov/pubmed/31617949

161. Berber P, Milenkovic A, Michaelis L, Weber BHF. Retinal organoid differentiation methods determine organoid cellular composition. J Transl Genet Genomics [Internet]. 2021;292–303. Available from: https://jtggjournal.com/article/view/4287

162. Akhtar T, Xie H, Khan MI, Zhao H, Bao J, Zhang M, et al. Accelerated photoreceptor differentiation of hiPSC-derived retinal organoids by contact co-culture with retinal pigment epithelium. Stem Cell Res [Internet]. 2019 Aug;39(June):101491. Available from: https://linkinghub.elsevier.com/retrieve/pii/S1873506119301217

163. Burnside B, Laties AM. Actin filaments in apical projections of the primate pigmented epithelial cell. Invest Ophthalmol [Internet]. 1976 Jul;15(7):570–5. Available from: http://www.ncbi.nlm.nih.gov/pubmed/819393

164. Steinberg RH. Interactions between the retinal pigment epithelium and the neural retina. Doc Ophthalmol [Internet]. 1985 Oct 15;60(4):327–46. Available from: http://www.ncbi.nlm.nih.gov/pubmed/3905312

165. Nakano T, Ando S, Takata N, Kawada M, Muguruma K, Sekiguchi K, et al. Self-formation of optic cups and storable stratified neural retina from human ESCs. Cell Stem Cell [Internet]. 2012;10(6):771–85. Available from: http://dx.doi.org/10.1016/j.stem.2012.05.009

166. Lowe A, Harris R, Bhansali P, Cvekl A, Liu W. Intercellular Adhesion-Dependent Cell Survival and ROCK-Regulated Actomyosin-Driven Forces Mediate Self-Formation of a Retinal Organoid. Stem Cell Reports [Internet]. 2016 May;6(5):743–56. Available from: http://dx.doi.org/10.1016/j.stemcr.2016.03.011

167. Völkner M, Zschätzsch M, Rostovskaya M, Overall RW, Busskamp V, Anastassiadis K, et al. Retinal Organoids from Pluripotent Stem Cells Efficiently Recapitulate Retinogenesis. Stem Cell Reports [Internet]. 2016 Apr;6(4):525–38. Available from: https://linkinghub.elsevier.com/retrieve/pii/S2213671116000825

168. Mao Z, Bozzella M, Seluanov A, Gorbunova V. Comparison of nonhomologous end joining and homologous recombination in human cells. DNA Repair (Amst) [Internet]. 2008 Oct 1;7(10):1765–71. Available from: https://linkinghub.elsevier.com/retrieve/pii/S1568786408002474

169. Matsuyama M, Søraas A, Yu S, Kim K, Stavrou EX, Caimi PF, et al. Analysis of epigenetic aging in vivo and in vitro : Factors controlling the speed and direction. Exp Biol Med [Internet]. 2020 Nov 6;245(17):1543–51. Available from:

http://journals.sagepub.com/doi/10.1177/1535370220947015

170. Mkrtchyan G V., Abdelmohsen K, Andreux P, Bagdonaite I, Barzilai N, Brunak S, et al. ARDD 2020: from aging mechanisms to interventions. Aging (Albany NY) [Internet]. 2020 Dec 31;12(24):24484–503. Available from: https://www.aging-us.com/lookup/doi/10.18632/aging.202454

171. Raj K, Horvath S. Current perspectives on the cellular and molecular features of epigenetic ageing. Exp Biol Med [Internet]. 2020 Nov 10;245(17):1532–42. Available from: http://journals.sagepub.com/doi/10.1177/1535370220918329

172. Hoshino A, Horvath S, Sridhar A, Chitsazan A, Reh TA. Synchrony and asynchrony between an epigenetic clock and developmental timing. Sci Rep [Internet]. 2019 Dec 6;9(1):3770. Available from: http://www.nature.com/articles/s41598-019-39919-3

173. Burgess DJ. Somatic mutations linked to future disease risk. Nat Rev Genet [Internet]. 2015 Feb 23;16(2):69–69. Available from: http://www.nature.com/articles/nrg3889

174. Gontier G, Iyer M, Shea JM, Bieri G, Wheatley EG, Ramalho-Santos M, et al. Tet2 Rescues Age-Related Regenerative Decline and Enhances Cognitive Function in the Adult Mouse Brain. Cell Rep [Internet]. 2018;22(8):1974–81. Available from: https://doi.org/10.1016/j.celrep.2018.02.001

175. Lu Y, Brommer B, Tian X, Krishnan A, Meer M, Wang C, et al. Reprogramming to recover youthful epigenetic information and restore vision. Nature [Internet]. 2020 Dec 3;588(7836):124–9. Available from: http://dx.doi.org/10.1038/s41586-020-2975-4

176. Hisama FM, Oshima J, Martin GM. How Research on Human Progeroid and Antigeroid Syndromes Can Contribute to the Longevity Dividend Initiative. Cold Spring Harb Perspect Med [Internet]. 2016 Apr 1;6(4):a025882. Available from: http://www.ncbi.nlm.nih.gov/pubmed/26931459

177. Horvath S, Oshima J, Martin GM, Lu AT, Quach A, Cohen H, et al. Epigenetic clock for skin and blood cells applied to Hutchinson Gilford Progeria Syndrome and ex vivo studies. Aging (Albany NY) [Internet]. 2018 Jul 26;10(7):1758–75. Available from: https://www.aging-us.com/lookup/doi/10.18632/aging.101508

178. Maierhofer A, Flunkert J, Oshima J, Martin GM, Haaf T, Horvath S. Accelerated epigenetic aging in Werner syndrome. Aging (Albany NY) [Internet]. 2017 Apr 4;9(4):1143–52. Available from: https://www.aging-us.com/lookup/doi/10.18632/aging.101217

179. Miller JD, Ganat YM, Kishinevsky S, Bowman RL, Liu B, Tu EY, et al. Human iPSC-Based Modeling of Late-Onset Disease via Progerin-Induced Aging. Cell Stem Cell [Internet]. 2013 Dec;13(6):691–705. Available from: https://linkinghub.elsevier.com/retrieve/pii/S1934590913004979

180. Eldred KC, Hadyniak SE, Hussey KA, Brenerman B, Zhang P-W, Chamling X, et al. Thyroid hormone signaling specifies cone subtypes in human retinal organoids. Science (80-) [Internet]. 2018 Oct 12;362(6411). Available from: https://www.science.org/doi/10.1126/science.aau6348

181. Wang RJ. Lethal effect of "daylight" fluorescent light on human cells in tissue-

culture medium. Photochem Photobiol [Internet]. 1975 May;21(5):373–5. Available from: https://onlinelibrary.wiley.com/doi/10.1111/j.1751-1097.1975.tb06688.x

182. Newman E, Reichenbach A. The Müller cell: a functional element of the retina. Trends Neurosci [Internet]. 1996 Aug;19(8):307–12. Available from: https://linkinghub.elsevier.com/retrieve/pii/0166223696100400

183. Reichenbach A, Bringmann A. New functions of Müller cells. Glia [Internet]. 2013 May;61(5):651–78. Available from: https://onlinelibrary.wiley.com/doi/10.1002/glia.22477

184. Bringmann A, Pannicke T, Grosche J, Francke M, Wiedemann P, Skatchkov SN, et al. Müller cells in the healthy and diseased retina. Prog Retin Eye Res [Internet]. 2006 Jul;25(4):397–424. Available from: https://linkinghub.elsevier.com/retrieve/pii/S1350946206000164

185. Babraham Bioinformatics - FastQC A Quality Control tool for High Throughput Sequence Data [Internet]. [cited 2019 Nov 11]. Available from: https://www.bioinformatics.babraham.ac.uk/projects/fastqc/

186. Ewels P, Magnusson M, Lundin S, Käller M. MultiQC: summarize analysis results for multiple tools and samples in a single report. Bioinformatics [Internet]. 2016 Oct 1;32(19):3047–8. Available from: https://academic.oup.com/bioinformatics/article-lookup/doi/10.1093/bioinformatics/btw354

187. Bolger AM, Lohse M, Usadel B. Trimmomatic: a flexible trimmer for Illumina sequence data. Bioinformatics [Internet]. 2014 Aug 1;30(15):2114–20. Available from: https://academic.oup.com/bioinformatics/article-lookup/doi/10.1093/bioinformatics/btu170

188. Dobin A, Davis CA, Schlesinger F, Drenkow J, Zaleski C, Jha S, et al. STAR: ultrafast universal RNA-seq aligner. Bioinformatics [Internet]. 2013 Jan;29(1):15–21. Available from: https://academic.oup.com/bioinformatics/article-lookup/doi/10.1093/bioinformatics/bts635

189. Ensembl version 97 homo sapiens [Internet]. [cited 2019 Nov 11]. Available from: ftp://ftp.ensembl.org/pub/release-97/fasta/homo_sapiens/dna/

190. Li B, Dewey CN. RSEM: accurate transcript quantification from RNA-Seq data with or without a reference genome. BMC Bioinformatics [Internet]. 2011 Dec 4;12(1):323. Available from: https://bmcbioinformatics.biomedcentral.com/articles/10.1186/1471-2105-12-323

191. Strunz T, Kiel C, Grassmann F, Ratnapriya R, Kwicklis M, Karlstetter M, et al. A mega-analysis of expression quantitative trait loci in retinal tissue. Liu Y, editor. PLoS Genet [Internet]. 2020 Sep 1;16(9):e1008934. Available from: https://dx.plos.org/10.1371/journal.pgen.1008934

192. R Team Core. A language and environment for statistical computing. R Foundation for Statistical Computing, Vienna, Austria. Vienna: R Foundation for Statistical Computing; 2017. p. 2017.

193. Love MI, Huber W, Anders S. Moderated estimation of fold change and dispersion for RNA-seq data with DESeq2. Genome Biol [Internet]. 2014 Dec 5;15(12):550. Available from: http://genomebiology.biomedcentral.com/articles/10.1186/s13059-014-0550-8

194. Kolde R. CRAN - Package pheatmap. Https://Cran.R-Project.Org/Web/Packages/Pheatmap/. 2019.

10. List of Abbreviations

Abbreviation	Meaning
adRP1	autosomal dominant RP1
AP	advanced placement
arRP1	autosomal recessive RP1
ATP1A3	ATPase Na+/K+ transporting subunit alpha 3
ATRA	all-trans retinoic acid
BEST1	bestrophin 1
BMP4	bone morphogenic protein 4
bp	base pair
BRN3A	POU class 4 homeobox 1
bRPE	byproduct RPE
BSA	bovine serum albumin
C	cystein
CALB1	calbindin 1
Cas9	CRISPR associated protein 9
cDNA	complementary DNA
CRISPR	clustered regularly interspaced short palindromic repeats
CRX	cone-rod homeobox
Dapi	4',6-Diamidin-2-phenylindol
DAPT	{N-[N-(3,5-difluorophenacetyl-L-alanyl)]-S-phenylglycine t-butyl ester
DEG	differentially expressed genes
dest.	destilled
DMEM	dulbecco's modified eagle medium
DMSO	dimethylsulfoxide
DNA	deoxyribonucleicacid
dNTP	deoxynucleotidetriphosphate
ECM	extracellular matrix
E.coli	Escherichia coli
e.g.	exempli gratia (for example)
EDTA	ethylendiamintetraacetate
et al.	et alia (and others)
FBS/RCS	fetal bovine/calf serum
FIJI	Fiji is just ImageJ
g	gram
GCL	ganglion cell layer
gDNA	genomic DNA
GFR	growth factor reduced
GO:BP	gene ontology biological process
gRNA	guide RNA
HD	healthy donor
HI-FBS	heat inactivated fetal bovine serum
HPRT1	hypoxanthine phosphoribosyltransferase 1
indel	insertion or deltion

INL	inner nuclear layer
ipGC	intrinsically photosensitive retinal ganglion cell
iPSC	induced pluripotent stem cell
IS	inner segment
IWR-1e	inhibitor of Wnt response compound-1-endo
KCNB1	potassium voltage-gated channel subfamily B member 1
kDA	kilodalton
KI67	marker of proliferation Ki-67
KO	knockout
LCA	Leber congental amarousis
LLC	limited liability company
Ltd	limited
m	milli
M	molar
M1	RO differentiation method 1
M2	RO differentiation method 2
M3	RO differentiation method 3
mAB	monoclonal antibody
MITF	melanocyte inducing transcription factor
mRNA	messenger RNA
mTeSR_G	mTeSR^{TM} plus medium with 25 µg/ml gentamycin
n	nano
NGS	next generation sequencing
nM	nanomolar
ON	overnight
ONL	outer nuclear layer
OPN1M/LW	opsin 1, medium/long wave sensitive
OPN1SW	opsin 1, short wave sensitive
orbRO	orbital shaker RO
OS	outer segment
pAB	polyclonal antibody
PBMC	peripheral blood mononuclear cell
PBS	phosphate buffered saline
PCR	polymerase chain reaction
Pen/Strep	penicillin/streptomycin
PFA	paraformaldeyd
PMEL	premelanosome protein
PRKCα	protein kinase C alpha
PROX1	prospero homeobox 1
PRPH2	peripherin 2
P.S.	postscriptum (written after)
rcf	relative centrifugal force
RCVRN	recoverin
RHO1D4	rhodopsin 1D4
RLBP1	retinaldehyde binding protein 1
RNA	ribonucleicacid

RNA-seq	RNA sequencing
RO	retinal organoid
ROM1	retinal outer segment membrane protein 1
RP	retinitis pigmentosa
RP1	retinitis pigmentosa 1 axonemal microtubule associated
RPE	retinal pigment epithelium
RPE65	retinoid isomerohydrolase RPE65
RS1	retinoschisin 1
RT	room temperature
SAG	smoothened agonist
sgRNA	single guide RNA
SNCG	synuclein gamma
SpCas9	Streptococcus pyogenes Cas9
statRO	stationary RO
Tet2	ten eleven translocation methylcytosine dioxygenase 2
TFAP2A	transcription factor AP-2 alpha
vs.	versus
VSX2	visual system homeobox 2
wt/WT	wildype
ZO-1	tight junction protein 1
µ	micro
µl	microliter
µM	micromolar

11. List of Figures

in 6-month-old ROs. (**B**) ROs from four timepoints (6 months, 12 months, 18 months, and 24 months) show the preservation of the Mueller cell marker RLBP1 expression over time. Images are counterstained with Dapi. Scale bar: 50 µm.......................... 68

Figure 28: Top ten enriched pathways of DEGs downregulated over time. The top ten enriched GO:BP pathways for four comparisons is shown: (**A**) DEGs downregulated at 12 months (in comparison to 6 months), (**B**) DEGs downregulated at 18 months (in comparison to 12 months), (**C**) DEGs downregulated at 24 months (in comparison to 18 months), and (**D**) DEGs downregulated at 24 months (in comparison to 6 months). Several important pathways are written in bold. Green bars indicate -log10(p) and the threshold for significance (p = 0.05) is shown as a dashed line..... 69

Figure 29: Photoreceptor marker expression decreases over time. Heatmaps of (**A**) photoreceptor markers (these markers are not subtype specific for rod or cones) and (**B**) cone photoreceptor markers are shown. The expression of all 15 markers decreased over time and was significantly lower in 24-month-old ROs than in 6-month-old ROs. The black, grey, white, and striped bar directly above the heatmap denotes the origin of the samples. (**C**) In general, few photoreceptors showed RS1 or ATP1A3 expression. (**D**) Individual photoreceptors showed pristine RS1 and ATP1A3 expression correctly localized at the membrane of photoreceptor IS. The best RS1 and ATP1A3 expression pattern was seen in a 24-month-old RO. The position of the magnified images shown in (D) are denoted as white boxes in (C). (**E**) In general, few photoreceptors showed KCNB1 expression, although individual photoreceptors showed KCNB1 expression correctly localized at the membrane of photoreceptor IS (arrowheads). (**F**) The normalized expression levels of the markers stained in (C-E) is shown. ATP1A3 and KCNB1 were significantly downregulated over time, whereas the reduction in RS1 expression was not significant. Scale bars: 10 µm. *** p < 0.001.. 70

Figure 30: Long-term ROs retain low expression of ganglion cell markers. (**A**) The normalized expression of four ganglion cell markers (BRN3A, POU4F2, ATOH7 and ISL1) is shown. All four markers were expressed in ROs at all timepoints. (**B**) 6-, 12-, 18-, and 24-month-old ROs contain SNCG-positive (white) and PROX1-positive (green) cells. The SNCG-positive plexiform layers demarcate the ONL and INL. Magnified images show the presence of SNCG-positive / PROX1-positive horizontal cells (blue arrows) and SNCG-positive / PROX1-negative putative ganglion cells (yellow arrows). The location of the magnified images is denoted with a yellow square. (**C**) 6-, 12-, 18-, and 24-month-old ROs contain SNCG-positive (white) and TFAP2A-

12. List of Tables

13. Selbständigkeitserklärung

Ich, Berber, Patricia geboren am 29.03.1992 in Herrenberg, erkläre hiermit, dass ich die vorliegende Arbeit ohne unzulässige Hilfe Dritter und ohne Benutzung anderer als der angegebenen Hilfsmittel angefertigt habe.

Die aus anderen Quellen direkt oder indirekt übernommenen Daten und Konzepte sind unter Angabe der Quelle gekennzeichnet. Insbesondere habe ich nicht die entgeltliche Hilfe von Vermittlungs- bzw. Beratungsdiensten (Promotionsberater oder andere Personen) in Anspruch genommen.

Die Arbeit wurde bisher weder im In- noch im Ausland in gleicher oder ähnlicher Form einer anderen Prüfungsbehörde vorgelegt.

Regensburg, 31.10.2022

Ort, Datum

eigenhändige Unterschrift

des Promovenden

14. Acknowledgements